The Shallow Water Test Cases for a Global Model with Documentation of the Results

K. Cassirer, R. Hess, C. Jablonowski and W. Joppich

Institute for Algorithms and Scientific Computing (SCAI)
GMD – German National Research Center for Information Technology
53754 Sankt Augustin

May 3, 1996

Abstract

In this documentation the results are described which were obtained by using a grid point oriented approach to solve the shallow water equations on the globe. Several test cases of the shallow water test set have been evaluated.

This work was carried out on behalf of the Deutscher Wetterdienst (DWD).

Contents

List of Figures

List of Tables

1 Introduction

The program *BARGLO* [4] of the German Weather Service (Deutscher Wetterdienst, DWD) solves the shallow water equations on the globe. The space discretization uses an almost uniform triangular mesh, whose generation starts from a regular icosahedron, which is embedded into the two-sphere [1]. The further refinement finally leads to a triangulation (see Section 3), which is almost regular and which provides a data structure having nice properties with respect to a later parallelization (see Section 5). Having an approximately equally spaced grid, there is no need for a special procedure close to the poles as in many other approaches.

Today, spectral methods are the most widely accepted and applied algorithms both for numerical weather prediction and for the atmospheric part of global climate models. The idea of using massively parallel computer architectures (perhaps for higher resolutions) has raised the question again, whether grid point models or spectral methods are more promising. Of course, the advantages and the disadvantages of the two methods are known, but never compared in a fair and systematic way. Therefore, applying the grid point oriented approach of the DWD to the standard test suite will not only contribute to such a fair comparison but also deliver the material which is necessary for strategic decisions within the DWD's new global model. As already mentioned, there is no clear answer to the question whether the spectral technique [3] or a grid point method is preferable. Both approaches have advantages (especially the grid point approach offers the principal possibility to use optimal order methods) but the use of parallel architectures again poses the above question because of the more local features of grid point based models. Therefore, it is both of theoretical and practical interest to investigate the given model. For spectral methods there exists a widely accepted sequence of test cases (see [2, 6]), which will detect the numerical properties of solving procedures. In this documentation we describe the results which we obtained running the grid point program BARGLO in its original version and with some optimizations on all but one the test cases. The optimization of the code, which essentially results in a modified time stepping, is described later.

The numerical experiments are performed on several resolutions having an average distance between mesh points of 542 km for the coarsest grid and of 125 km for the finest one. The corresponding spectral truncation numbers are approximately T21/T42 and T106, respectively, if the grid spacing is considered at the equator.

2 The Continuous Problem

In Cartesian coordinates the shallow water equations are given by the advective form of the momentum equations and by the continuity equation:

$$\frac{\partial u}{\partial t} + u\frac{\partial u}{\partial x} + v\frac{\partial u}{\partial y} - fv + g\frac{\partial(h + h_s)}{\partial x} = 0$$

$$\frac{\partial v}{\partial t} + u\frac{\partial v}{\partial x} + v\frac{\partial v}{\partial y} + fu + g\frac{\partial(h + h_s)}{\partial y} = 0 \qquad (2.1)$$

$$\frac{\partial h}{\partial t} + u\frac{\partial h}{\partial x} + v\frac{\partial h}{\partial y} + h\left(\frac{\partial u}{\partial x} + \frac{\partial v}{\partial y}\right) = 0$$

u and v are the horizontal wind components. h represents the depth of the fluid, h_s the height of the underlying mountain. The Coriolis term is $f = 2\Omega \sin\varphi$ with the latitude $\varphi \in [-\frac{1}{2}\pi, \frac{1}{2}\pi]$ varying from the north pole ($\varphi = \frac{1}{2}\pi$) to the south pole ($\varphi = -\frac{1}{2}\pi$). $\Omega = 2\pi/T$ with T being the length of a siderian day, is the angular velocity of the earth. The longitude λ varies in $[0, 2\pi]$.

In vector representation using Cartesian coordinates with the origin in the center of the earth the above system (2.1) reads like

$$\frac{\partial \mathbf{V}}{\partial t} + \mathbf{V} \cdot \nabla \mathbf{V} + f\mathbf{k} \times \mathbf{V} + g\nabla(h + h_s) = 0$$

$$\frac{\partial h}{\partial t} + \mathbf{V} \cdot \nabla h + h\left(\nabla \cdot \mathbf{V}\right) = 0 \qquad (2.2)$$

Here $\mathbf{V} := (u, v, w)$ is the three dimensional wind vector, ∇ is given by $(\frac{\partial}{\partial x}, \frac{\partial}{\partial y}, \frac{\partial}{\partial z})$ or $(\frac{\partial}{\partial x}\mathbf{i} + \frac{\partial}{\partial y}\mathbf{j} + \frac{\partial}{\partial z}\mathbf{k})$. $\mathbf{i}, \mathbf{j}$ and $\mathbf{k}$ are the unit vectors into the three space directions.

3   The Discretized Problem

3.1   The Triangular Mesh

The discretization of the continuous problem uses a mesh consisting of spherical triangles, having areas and sides of approximately the same size and length, respectively. The first step to create this mesh consists in embedding a regular icosahedron (20 triangles, 30 edges and 12 nodes) into the two-sphere. Because the icosahedron may be placed anywhere in the two-sphere, the poles play no special role. Nevertheless, for better representation two nodes of the icosahedron are placed into the poles. Because each of the initial nodes is surrounded by 5 triangles, the angles within the triangles are $\frac{2\pi}{5}$. The length of each side is given by

$$L = 2\arccos\frac{\cos\frac{\pi}{5}}{\sin\frac{2\pi}{5}} \cdot R_{earth}$$

with $R_{earth} \approx 6371$ km. Therefore $L \approx 7053.6$ km. The height of the triangles is

$$H = \arcsin\left(\sin L \sin\frac{2\pi}{5}\right) \cdot R_{earth}.$$

To compute the coordinates φ and λ of the twelve initial points on the two-sphere of the twenty spherical triangles the figure is subdivided into $5 \cdot 4$ large triangles (see Figure 3.1). Each of the five sub-domains consisting of four triangles is shifted in latitudinal direction (λ-direction), by $\frac{2\pi}{5}$ against the previous one. The sub-domains are equal with respect to φ.

```
              (3,2)  north pole
                /\
               /  \
              /    \
      (2,2) ._____. (3,1)
            / \    /
           /   \  /
          /     \/
   (1,2) ._____. (2,1)
          \     /
           \   /
       j    \ /    i
             \/
          (1,1) south pole
```

Figure 3.1: Principal idea to construct the icosahedral mesh

The final data structure is generated by repeating this initial data part five times (see Figure 3.2). The refinement of this initial structure is done in a standard way: the midpoints of the arcs of the spherical triangles are connected by geodesic arcs, yielding four sub-triangles. This procedure is repeated several times until the desired resolution is reached. For the refinement depth $m \geq 0$ and $n := 2^m$ the total number of nodes is $N = 10n^2 + 2$. The number of triangles is $T = 20n^2$. Table 3.1 collects some interesting details of meshes created by this procedure. A is the average angle of opening and d is the average Euclidean distance between the midpoints of two adjacent triangles. The mesh corresponding to two refinement steps is shown in Figure 3.2.

The discretization which is described later (see Section 3) places all unknowns into the *midpoints* of the triangles. This simplifies the difference operators because only three neighbor points occur in the difference equations and supplies a good locality for the later parallelization. On the other hand, the resulting mesh is not completely regular. The distance between neighboring points varies and may cause problems to achieve the desired order of approximation when discretizing the continuous equations. From this approach the data structure is derived in a natural way. Five times four of the initial triangles are connected, resulting in two rhomboids within each of the five parallelograms. Considering the centers of the triangles which are obtained by the

Figure 3.2: Main structure of the icosahedral approach and a mesh after two refinement steps

refinement, five logically rectangular data partitions are created. The number of nodes per rectangle depends on the number of refinement steps. This number is $je \times ie = (n+1) \times (2n+1)$ (see Table 3.1). Similarly to the connection of the large initial triangles the triangles of finer meshes are considered as the basic elements of rhomboids, composed of a lower and an upper triangle. All the required information concerning the vertices and the midpoints is computed in a preprocessing step and written to a file which is read by the main program. The details which are read from this file are the λ- and φ-values of the midpoints of the triangles, the length of the sides, the distance to neighbor points, the unit vectors standing perpendicular to the triangles, the areas of the triangles and information concerning the Coriolis term.

step		Nodes	Triangles	Length (km)	Angle (grad)	dist. (km)		
m	n	N	T	L	A	d	ie	je
0	1	12	20	7674	69.00		3	2
1	2	42	80	3837	34.50		5	3
2	4	162	320	1919	17.30		9	5
3	8	642	1280	959	8.63	542	17	9
4	16	2562	5120	480	4.31	271	33	17
5	32	10242	20480	240	2.16	136	65	33
6	64	40962	81920	120	1.08	68	129	65

Table 3.1: Characteristic values for the triangular mesh

3.2 Time Discretization

As time discretization an explicit time–split scheme is used. The advective terms can be calculated in large time steps, whereas the gravity and Coriolis terms are treated in smaller steps. In this way, the time step restrictions of the explicit schemes are well adapted to the wave speeds the terms are dealing with.

For the slower advective changes the following equations are solved in every large time step:

$$
\begin{aligned}
\frac{\partial \mathbf{V}_l}{\partial t} + \mathbf{V}_l \cdot \nabla \mathbf{V}_l &= 0 \\
\frac{\partial h_l}{\partial t} + \mathbf{V}_l \cdot \nabla h_l &= 0
\end{aligned}
\tag{3.1}
$$

The subscript l denotes the results of the advective time step. Integration is done with a two–step Lax–Wendroff scheme:

$$
\begin{aligned}
\mathbf{V}_l^{n+\frac{1}{2}} &= \mathbf{V}_l^n - \frac{\Delta t}{2} \mathbf{V}_l^n \cdot \nabla \mathbf{V}_l^n \\
h_l^{n+\frac{1}{2}} &= h_l^n - \frac{\Delta t}{2} \mathbf{V}_l^n \cdot \nabla h_l^n
\end{aligned}
\tag{3.2}
$$

$$
\begin{aligned}
\frac{\mathbf{V}_l^{n+1} - \mathbf{V}_l^n}{\Delta t} &= -\mathbf{V}_l^{n+\frac{1}{2}} \cdot \nabla \mathbf{V}_l^{n+\frac{1}{2}} \\
\frac{h_l^{n+1} - h_l^n}{\Delta t} &= -\mathbf{V}_l^{n+\frac{1}{2}} \cdot \nabla h_l^{n+\frac{1}{2}}
\end{aligned}
\tag{3.3}
$$

The full set of equations including gravity and Coriolis terms are calculated afterwards with smaller time steps using the advection results of the long ones. Discretization is done with a semi–implicit Euler scheme. The Coriolis term is evaluated implicitly to get a more stable discretization. The gravitational term is determined explicitly:

$$
\begin{aligned}
h^{n_{j+1}} &= h^{n_j} + \frac{\Delta t}{k}\left(\frac{h_l^{n+1} - h_l^n}{\Delta t} - h^{n_j}\nabla\cdot\mathbf{V}^{n_j}\right) \\
\mathbf{V}^{n_{j+1}} &= \mathbf{V}^{n_j} + \frac{\Delta t}{k}\left(\frac{\mathbf{V}_l^{n+1} - \mathbf{V}_l^n}{\Delta t} - fe\times\frac{\mathbf{V}^{n_{j+1}} + \mathbf{V}^{n_j}}{2} - g\nabla(h^{n_{j+1}} + h_s)\right)
\end{aligned}
\tag{3.4}
$$

with $j = 1\ldots k$. According to the speed of the advection and the fast gravity waves, respectively, the large time steps are subdivided into $k = 5$ smaller ones.

3.3   Stability Considerations

Unfortunately, the discretization for the advection (3.1) is not stable with a straight forward space discretization, see [8]. A stability analysis for this situation is fairly complicated. However, a simplified study explains this statement:

Consider the nonlinear, one–dimensional convection equation:

$$
\frac{\partial u}{\partial t} + a\frac{\partial u}{\partial x} = 0
\tag{3.5}
$$

Time discretization due to Lax–Wendroff with centered space discretization gives:

$$
\begin{aligned}
u_i^{n+\frac{1}{2}} &= u_i^n - \frac{\Delta t}{2}\,a\,\frac{u_{i+1}^n - u_{i-1}^n}{2\Delta x}\quad\text{and} \\
u_i^{n+1} &= u_i^n - \Delta t\,a\,\frac{u_{i+1}^{n+\frac{1}{2}} - u_{i-1}^{n+\frac{1}{2}}}{2\Delta x}
\end{aligned}
\tag{3.6}
$$

or after inserting the first equation into the second one

$$
u_i^{n+1} = u_i^n - \frac{1}{2}\frac{\Delta t\,a}{\Delta x}(u_{i+1}^n - u_{i-1}^n) + \frac{1}{8}\frac{\Delta t^2 a^2}{\Delta x^2}(u_{i+2}^n - 2u_i^n + u_{i-2}^n);
\tag{3.7}
$$

For the Von Neumann stability analysis (see [7]) the actual calculated solution u is developed into a Fourier series, $u_i^n = E^n e^{Ii\phi}$, $I^2 = 1$:

$$G := \frac{E^{n+1}}{E^n} = 1 - I\sigma\sin\phi - \frac{\sigma^2}{2}\sin^2\phi, \tag{3.8}$$

where $\sigma = \frac{\Delta t\, a}{\Delta x}$ denotes the Courant number. The modulo of the amplification factor G gives the growth of the amplitudes of the solution.

With

$$|G|^2 = 1 + \frac{\sigma^4}{4}\sin^4\phi > 1 \tag{3.9}$$

it is obvious that the discretization is unstable independent from the size of the Courant number σ.

Because of these reasons, which are reflected by the numerical results of the original code, we propose a different procedure which has been used in the framework of BARGLO. The practical improvement is described below (see Section 4) and can be explained theoretically. Applying a discretization which uses a Lax–Friedrich step instead of the Euler step within the first part of the Lax–Wendroff scheme gives:

$$
\begin{aligned}
u_i^{n+\frac{1}{2}} &= \frac{u_{i+1}^n + u_{i-1}^n}{2} - \frac{\Delta t}{2}a\,\frac{u_{i+1}^n - u_{i-1}^n}{2\Delta x} \quad \text{and} \\
u_i^{n+1} &= u_i^n - \Delta t\, a\,\frac{u_{i+1}^{n+\frac{1}{2}} - u_{i-1}^{n+\frac{1}{2}}}{2\Delta x}
\end{aligned}
\tag{3.10}
$$

instead. The Von Neumann stability analysis gives:

$$G = 1 - I\sigma\cos\phi\sin\phi - \frac{\sigma^2}{2}\sin^2\phi \tag{3.11}$$

and

$$|G|^2 = 1 + \sigma^2\sin^4\phi\left(\frac{\sigma^2}{4} - 1\right) < 1 \text{ for } \sigma < 2. \tag{3.12}$$

This scheme is stable for Courant numbers $\sigma < 2$. For multi–dimensional problems the critical Courant number can be smaller. Ideally one should consider the total time splitting scheme with the Lax–Wendroff scheme for the large steps and the Eulerian scheme for the small steps together. Nonlinear stability is achieved with an additional diffusion step, see sec. (3.5).

Further improvement of the stability of the time splitting scheme was gained by performing a Lax–Wendroff time scheme for the small non–advective time steps, too. The

semi–implicit Euler scheme (3.4) was substituted with a semi–implicit Lax–Wendroff scheme as follows:

$$
h^{n_{j+\frac{1}{2}}} \;=\; h^{n_j} + \frac{\Delta t}{2k}\left(\frac{h_l^{n+1} - h_l^n}{\Delta t} - h^{n_j}\nabla\cdot\mathbf{V}^{n_j}\right) \tag{3.13}
$$

$$
\mathbf{V}^{n_{j+\frac{1}{2}}} \;=\; \mathbf{V}^{n_j} + \frac{\Delta t}{2k}\left(\frac{\mathbf{V}_l^{n+1} - \mathbf{V}_l^n}{\Delta t} - f e \times \frac{\mathbf{V}^{n_{j+\frac{1}{2}}} + \mathbf{V}^{n_j}}{2} - g\nabla(h^{n_{j+\frac{1}{2}}} + h_s)\right)
$$

$$
h^{n_j+1} \;=\; h^{n_j} + \frac{\Delta t}{k}\left(\frac{h_l^{n+1} - h_l^n}{\Delta t} - h^{n_{j+\frac{1}{2}}}\nabla\cdot\mathbf{V}^{n_{j+\frac{1}{2}}}\right) \tag{3.14}
$$

$$
\mathbf{V}^{n_j+1} \;=\; \mathbf{V}^{n_j} + \frac{\Delta t}{k}\left(\frac{\mathbf{V}_l^{n+1} - \mathbf{V}_l^n}{\Delta t} - f e \times \frac{\mathbf{V}^{n_j+1} + \mathbf{V}^{n_{j+\frac{1}{2}}}}{2} - g\nabla(h^{n_j+1} + h_s)\right)
$$

With these two slight changes it became possible to increase the size of possible time steps drastically. However, the computational costs for every time step almost double because of the more expensive Lax–Wendroff scheme within the small time steps. But the total increase in efficiency is shown with the results of the test cases, see (4).

3.4   Spatial Discretization

A finite volume method on the triangular mesh is used to discretize the governing equations. The following formula result:

1. $\nabla\psi$, with ψ a scalar quantity:

$$
\nabla\psi = \frac{1}{2F}\sum_{i=1}^{i=3} l_i(\psi_i - \psi_0)\mathbf{e}_{2i}
$$

   The used conventions are: index 0 indicates the reference triangle, the indices $i = 1,\ldots,3$ are used for the surrounding triangles, l_i is the length of the three sides of the triangle, $\mathbf{e}_{2i}$ is the unit vector which stands perpendicular to the vector normal to the triangle and which also stands perpendicular to the side i of the triangle (because these vectors are given in Cartesian coordinates, $\nabla\psi$ is given in these coordinates, too).

2. $\nabla\cdot V$, with $V = (V_1, V_2, V_3) = (u, v, w)$ a vector field:

$$
\nabla\cdot V = \frac{1}{2F}\sum_{i=1}^{i=3} l_i\left(\sum_{k=1}^{k=3}(V_{k0} + V_{ki})\,(\mathbf{e}_{2i})_k\right)
$$

3. $\Delta\psi$, with ψ a scalar quantity:

$$\Delta\psi = \frac{1}{F} \sum_{i=1}^{i=3} \frac{l_i}{\Delta x_i}(\psi_i - \psi_0)$$

Here the new quantity Δx_i is the distance between the midpoint of the reference triangle and the i-th neighboring triangle.

4. Diffusion $\Delta^2\psi$, with ψ a scalar quantity:
Because of $\Delta^2\psi = \Delta w$ with $w = \Delta\psi$ there is

$$\Delta^2\psi = \frac{1}{F} \sum_{i=1}^{i=3} \frac{l_i}{\Delta x_i}(w_i - w_0).$$

The formula for $\Delta\psi$ can be used to complete the representation.

3.5 Diffusion

For the nonlinear instability of the Eulerian advection a fourth order diffusion operator is added to the set of equations (diffusion coefficient K_4). Diffusion has to damp out high frequent error modes. In BARGLO the diffusion step is calculated after every long time step for every prognostic variable:

$$\psi_{smooth} = \psi - \Delta t K_4 \Delta^2 \psi$$

This smoothing has to reduce high frequent error modes by a factor of $\frac{1}{e}$ within a time frame of two or three hours.

For a two dimensional model analysis the space discretization of Δ^2 on an equidistant grid of mesh size Δx starts with the standard second order approximation of the Laplacian, which is described by the well-known five–point stencil. From this we get the second order approximation for $\Delta^2 = \Delta\Delta$ which is given by the 13–point–stencil:

$$\frac{1}{\Delta x^4}\begin{bmatrix} & & 1 & & \\ & 2 & -8 & 2 & \\ 1 & -8 & 20 & -8 & 1 \\ & 2 & -8 & 2 & \\ & & 1 & & \end{bmatrix}$$

This space discretization corresponds to the actual discretization as described in Section 3.

A two dimensional analysis using a frequency of the form $\psi = \Psi e^{Ii\varphi} e^{Ij\theta}$ gives

$$G = \frac{\Psi_{smooth}}{\Psi} = 1 - 16 \frac{\Delta t}{\Delta x^4} K_4 \left(\sin^2 \frac{\varphi}{2} + \sin^2 \frac{\theta}{2} \right)^2 \qquad (3.15)$$

High frequencies correspond to values φ, θ close to π, while low frequencies correspond to ϕ, θ close to 0. The requirement to reduce high frequent error modes by a factor of $\frac{1}{e}$ within the time period $T = k \cdot \Delta t$ leads to:

$$G^k = \left(1 - 64 \frac{\Delta t}{\Delta x^4} K_4 \right)^k = \frac{1}{e}$$

From this we get a condition for the diffusion constant

$$K_4 = \frac{1}{64} \left(1 - e^{-\frac{1}{k}} \right) \frac{\Delta x^4}{\Delta t}$$

This method affects low frequencies in a negligible way. A table of proposed and used diffusion constants is given in Section 4.

4   The Shallow Water Test Set

The development of global weather forecast programs usually starts from the shallow water equations on the sphere. This 2D-problem already exhibits the main difficulties for the numerical solution of the 3D-problem which finally occurs in global weather forecast. To detect numerical properties of new numerical approaches and software developments a standard test set consisting of a series of test cases has been proposed [6]. Any new development should perform well on these test cases. Because the realized test cases are described in more meteorological detail below, here the numerical properties which are checked by the test set are mentioned:

- The advection of a structure having compact support by a specific wind field checks the behavior of the advection scheme.

- The steady state, nonlinear zonal geostrophic flow with given wind fields tests the capability of the scheme to handle the poles and, in addition, nonlinearities come into play.

- Other test cases which are characterized by increasing complexity and realism look for the treatment of more complicated local features of atmospheric flow like isolated mountains and driving a low pressure region around the sphere, respectively.

– Finally test cases providing atmospheric initial conditions of the 500 mb height and wind fields from several atmospheric states check the capability of the scheme under realistic conditions.

Of course, the standard numerical test in meteorology, applying a Rossby-Haurwitz wave is included.

The results of the test cases are evaluated by comparing to analytical solutions and highly resolved reference solutions. The error is measured in different norms. When comparing the results of the described test cases with already published results using implementations of spectral models one should keep in mind the following fact: most of the test situations consider problems with relatively smooth phenomena. They can be represented more or less exactly using frequencies up to a relatively small truncation number. Therefore, the spectral methods provide quasi exact solutions in these situations. This is not the case for grid point oriented approaches because their inherent locality is not able to detect global smoothness.

Because the numerical properties of the program BARGLO have to be compared to those which have been reported for spectral methods [2] it is of interest to collect some characteristic values which have been used there (Table 4.1).

Spectral Truncation M	Grid Points	Distance at the equator	Diffusion Constant K_4	Time Step Δt
42	$64 \cdot 128$	312 km	$0.50 \cdot 10^{16}$	1200 s
63	$96 \cdot 192$	208 km	$1.00 \cdot 10^{15}$	900 s
106	$160 \cdot 320$	125 km	$1.25 \cdot 10^{14}$	600 s
170	$256 \cdot 512$	78 km	$2.00 \cdot 10^{13}$	450 s
213	$320 \cdot 640$	62 km	$8.00 \cdot 10^{12}$	360 s

Table 4.1: Characteristic values for test cases using spectral methods

Some parameters relevant to the earth and all test cases are not used uniquely throughout the literature. Therefore we specify how we have used them:

– radius of the earth: $R_{earth} = 6371$ km instead of 6371.22 km

– angular velocity: $\Omega = \frac{2\pi}{T} s^{-1}$ ($T=$ siderian day $= 86164.1$ s) computed in single precision instead of the fixed value $\Omega = 7.292 \times 10^{-5} s^{-1}$

– gravitation $g = 9.81 \frac{m}{s^2}$ instead of $9.80616 \frac{m}{s^2}$

All of the analytic representations of initial states for the wind or for the geopotential height are given in spherical coordinates. The program BARGLO requires them in Cartesian form. If the surface vector $(U, V)^T$ is extended to the three-dimensional

vector $(U, V, W)^T$ where we assume $W = 0$, the Cartesian formulation of the velocity vector $(u, v, w)^T$ can be calculated by the transformation

$$
\begin{pmatrix} u \\ v \\ w \end{pmatrix} = \begin{pmatrix} -\sin\lambda & -\sin\varphi\cos\lambda & \cos\varphi\cos\lambda \\ \cos\lambda & -\sin\varphi\sin\lambda & \cos\varphi\sin\lambda \\ 0 & \cos\varphi & \sin\varphi \end{pmatrix} \begin{pmatrix} U \\ V \\ W \end{pmatrix}.
$$

As an example consider the test case 1. Here we have

$$
\begin{pmatrix} U \\ V \\ W \end{pmatrix} = \begin{pmatrix} U_0\left(\cos\varphi\cos\alpha + \sin\varphi\cos\lambda\sin\alpha\right) \\ -U_0\sin\lambda\sin\alpha \\ 0 \end{pmatrix}.
$$

Then the Cartesian representation is

$$
\begin{pmatrix} u \\ v \\ w \end{pmatrix} = \begin{pmatrix} -U_0\sin\lambda\cos\varphi\cos\alpha \\ U_0\left(\cos\lambda\cos\varphi\cos\alpha + \sin\varphi\sin\alpha\right) \\ -U_0\cos\varphi\sin\lambda\sin\alpha \end{pmatrix}.
$$

To have all components within the plane of the triangles the tangential components are calculated due to the rules which are specified in [4]. Any vector $\mathbf{V}$ is projected using the formula

$$
\mathbf{V}_{tang} = \mathbf{V} - <\mathbf{V}, \mathbf{n}> \mathbf{n} \tag{4.1}
$$

where $\mathbf{n}$ is the unit normal vector perpendicular to the plane of the triangle.

For all the experiments a standard output is given which describes the relative change of quantities like total energy and total mass with time. For most of the experiments we simulated a ten day period. Only test case 1 needs a twelve days simulation to be back at the initial situation, and the test cases representing real atmospheric states are provided for a five day forecast.

```
h0 =    .29400000E+05  hqu(t=0) =    .23172501E+05


hour    kin.energy  pot.energy tot.energy    tot.mass     var. of geop.


0       .59850E+21   .80633E+21  .14048E+22    .14755E+19  -.24347E-10
1       .99966      1.00031     1.00004      1.0000001     .16976E-10
2       .99939      1.00059     1.00008       .9999998  -.91625E-11
3       .99924      1.00081     1.00014       .9999994    .21802E-10
```

Table 4.2: Part of the standard output of BARGLO

Because the different quantities are defined in a special way, their calculation is given here:

– kinetic energy: $E_{kin} = \dfrac{\overline{h}}{2g} \displaystyle\sum_{triangles} \mathbf{V}_i \cdot \mathbf{V}_i area_i$

– potential energy: $E_{pot} = \dfrac{1}{2g} \displaystyle\sum_{triangles} \left(h_i - \overline{h}\right)^2 area_i$

– mass: $m = \dfrac{\varrho}{g} \displaystyle\sum_{triangles} h_i \, area_i$

Here $\overline{h} = \sum_{triangles} h_i area_i / surface$ is the weighted mean value of the geopotential. $surface$ is the sum of the areas of all planar triangles. Relative errors are given in terms of l_1, l_2 and l_∞-norms. With a true solution to a test case u_T and

$$I(u) := \int_{surface} u\, do \qquad \text{approximated by} \qquad \frac{\sum_{triangles} u_i \, \text{area}_i}{surface}$$

these quantities are defined for a scalar quantity as

$$
\begin{aligned}
l_1 &= \frac{I(|u - u_T|)}{I(|u_T|)} \\
l_2 &= \frac{\sqrt{I(|u - u_T|^2)}}{\sqrt{I(u_T^2)}} \\
l_\infty &= \frac{\max(|u - u_T|)}{\max |u_T|}
\end{aligned}
$$

The modifications for vector quantities are due to [6].

Performance measurements are not evaluated, because the current test is more concerned with numerical questions than efficient programming. The experiments have been done using a IBM RS6000 workstation. The code is not optimized, especially not with respect of cache usage. Such a tuning is of future interest. All data used DOUBLE PRECISION representation.

The sequence of experiments is performed using the diffusion constants as given in Table 4.3. They have been selected from [4]. The influence of the diffusion constant due to Section 3.5 is investigated later. For the mostly used time step sizes we give values of K_4 as proposed by the theoretical analysis of Section 3.5. The Δt which was used to calculate the diffusion coefficient is mentioned in parentheses. Additionally, we give the Δt which were calculated due to the stability condition. A systematic study of possible values for these quantities is postponed.

For all test cases we show results using both the original form of the program and the modified program (modified especially with respect to time stepping and with respect to the handling of the data structure). If nothing is specified, the presented results concern the program in its original form. The results obtained with the modified program are

refinement depth	diffusion constant		Δt
m	K_4 used	K_4 proposed (T=2)	proposed
3	$7.3 \cdot 10^{17}$	$1.5 \cdot 10^{17} (\Delta t = 3600s)$	8727 s
4	$4.5 \cdot 10^{16}$	$1.0 \cdot 10^{16} (\Delta t = 1800s)$	4327 s
5	$3.7 \cdot 10^{15}$	$7.1 \cdot 10^{14} (\Delta t = 900s)$	2164 s

Table 4.3: Diffusion constant depending on refinement depth and time step size

specified explicitly. The direct comparison of the calculations on the triangular mesh and on grids as they are used for spectral transform methods is not so easy because the mesh spacing in the latter case varies from the pole to the equator. The different spectral truncations correspond to approximate distances between neighboring points at the equator as follows: T42 (312 km), T63 (208 km), T106 (125 km), T170 (78 km) and T213 (62 km), respectively. For the triangular mesh the average distance between midpoints of neighboring triangles does not vary as extremely. For the different refinement steps we have average distances of 542 km (m=3), 271 km (m=4), 136 km (m=5) and 68 km (m=6), respectively (see Table 3.1). This has to be kept in mind when comparing time step sizes and diffusion coefficients as they have been used for the different test cases and numerical techniques.

4.1 Advecting Cosine Bell

This test case does not deal with the complete set of the shallow water equations. It concentrates on the advective component of the numerical approach. A cosine bell is placed at predescribed positions and advected over the sphere. It circulates around the equator, over the poles and at slight angles to these extreme values. After a simulation time of twelve days the bell should be back at the initial position. For this test case the predicted wind field is overwritten by an analytically specified wind field every time step. The analytical specification of the wind field and of the cosine pattern is given in [6]. It is necessary to transform the given definitions to the Cartesian coordinate system. Starting from the specifications of u, v and h as given in [6] we have:

$$u = -U_0 \sin \lambda \cos \varphi \cos \alpha \tag{4.2}$$

$$v = U_0 \left(\cos \lambda \cos \varphi \cos \alpha + \sin \varphi \sin \alpha \right) \tag{4.3}$$

$$w = -U_0 \cos \varphi \sin \lambda \sin \alpha \tag{4.4}$$

$$h = \begin{cases} \frac{h_0}{2} \left(1 + \cos \left(\frac{\pi r}{R} \right) \right) g & \text{if } r < R \\ 0 & \text{if } r \geq R \end{cases} \tag{4.5}$$

$h_0 = 1000m$ is prescribed and r is the great circle distance between some arbitrary point on the sphere and the center of the cosine bell [6].

The numerical experiments have been performed using the diffusion constant K_4 as specified in Table 4.3 for the corresponding refinement step. Table 4.4 contains the relation of the initial and final values of energy, mass and geopotential height. Additionally, the time step size is reported. These time step sizes produced stable results. A systematic search for the largest possible time step size can be done later, but always considering the accuracy requirements. Comparing the time step sizes of $\Delta t = 1200s$ and $\Delta t = 600s$ as they are used for the tests using spectral models with resolutions corresponding to T42 and T106, respectively, larger time step sizes are allowed even for the original program.
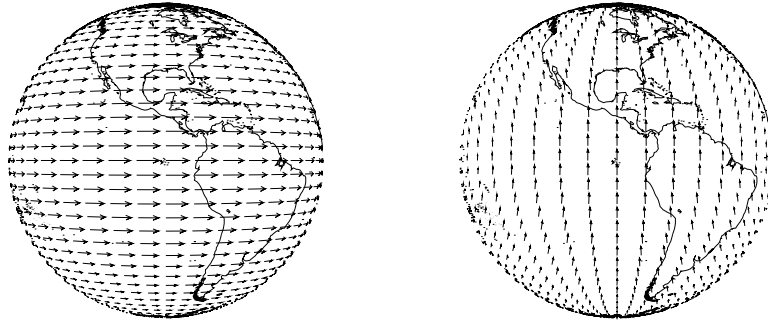

Figure 4.1: Initial state of wind fields with $\alpha = 0$ and $\alpha = \frac{\pi}{2}$

The first picture (Figure 4.1) shows the initial states of the wind field for different directions of α. The maximum velocity v_{max} is $38.609 \ ms^{-1}$.

This version of the program produces results which are not satisfactory for resolutions below refinement depth $m = 5$, as the loss of the total energy shows. The variation of the angle of rotation has no influence on the behavior of the program, as the results for the different resolutions prove. Figure 4.2 shows the initial and the final state of the cosine bell for $\alpha = 0$ using a resolution with $m = 5$ and calculating with $\Delta t = 900$ seconds. The profile of the cosine bell is slightly damaged and a small wave occurs behind the moving profile. According to this phenomenon the contour lines are more dense at the back end of the bell and less dense at the front of the profile. The difference between the initial state and the final state within the critical region is plotted in the upper part of Figure 4.3. The difference varies from -240 m to 210 m, approximately. Varying the direction of the bell's movement ($\alpha = \frac{\pi}{2}$ instead of $\alpha = 0.0$) shows no significant difference. Again, the oscillation is behind the bell. But now, due to the changed direction at another position (see Figure 4.3). In Figure 4.4 the error norms (l_∞, l_1, l_2) of the height errors for all angles using refinement depth $m = 5$ and $\Delta t = 900$ are shown. The relative errors seem to be large. Looking closer at the values, the reason for this is a small shift of the final cosine bell with respect to the reference bell

angle	m	Δt	after 2 days		after 6 days		after 12 days	
			E	M	E	M	E	M
$\alpha = 0$	3	3600	0.659	0.989	0.490	0.968	0.390	0.937
	4	1800	0.936	0.995	0.845	0.984	0.751	0.968
	5	900	0.990	0.997	0.972	0.992	0.946	0.984
$\alpha = \frac{\pi}{2}$	3	3600	0.656	0.989	0.491	0.968	0.393	0.937
	4	1800	0.936	0.995	0.845	0.984	0.752	0.967
	5	900	0.990	0.997	0.972	0.992	0.946	0.984
$\alpha = 0.05$	3	3600	0.659	0.989	0.517	0.973	0.390	0.937
	4	1800	0.936	0.995	0.864	0.986	0.751	0.968
	5	900	0.990	0.997	0.976	0.993	0.945	0.984
$\alpha = \frac{\pi}{2} - 0.05$	3	3600	0.680	0.991	0.518	0.973	0.396	0.938
	4	1800	0.936	0.995	0.865	0.986	0.752	0.967
	5	900	0.990	0.997	0.976	0.993	0.946	0.984
modified program								
$\alpha = 0$	5	1800	0.980	0.995	0.943	0.984	0.896	0.968
	5	900	0.987	0.997	0.965	0.992	0.934	0.984
$\alpha = \frac{\pi}{2}$	5	1800	0.980	0.995	0.944	0.984	0.897	0.968
	5	900	0.987	0.997	0.965	0.992	0.934	0.984
$\alpha = 0.05$	5	1800	0.980	0.995	0.952	0.986	0.895	0.968
	5	900	0.987	0.997	0.965	0.992	0.933	0.984
$\alpha = \frac{\pi}{2} - 0.05$	5	1800	0.980	0.995	0.953	0.986	0.897	0.968
	5	900	0.987	0.997	0.965	0.992	0.935	0.984

Table 4.4: Advection of the cosine bell; relative conservation of energy and mass, original and modified program

(see Figure 4.7). Therefore the centers of the two do not coincide and produce a large error. The maximum value of the final bell, which is for $\alpha = 0.0$ equal to 959.56 m, differs with respect to the maximum of the reference bell, which is for this resolution 989.75 m just by about 30.0 m. This again comes from the fact, that the specified center of the bells in general does not meet a center of a triangle and results in a velocity error. This influences the height of the errors, too. For the modified program using the improved time stepping the variation of the angle has no influence on the quality of the results. This is shown here for refinement step $m = 5$. Even with a time step size twice as large as allowed for the original program the results are of the similar accuracy. A possible time step size can be chosen three times larger than for the corresponding spectral computations. The error norms as shown in Figure 4.8 are larger than those reported for the unchanged algorithm. The reason for this may be the introduced artificial averaging (comparable to some artificial diffusion) during the modified time stepping procedure in combination with the principal facts which were already mentioned above. Comparing the structure of the error as presented both in

Figures 4.3 (above) and in Figure 4.6 with that reported for spectral methods ([2], Figure 1.2 b) shows the similarity.
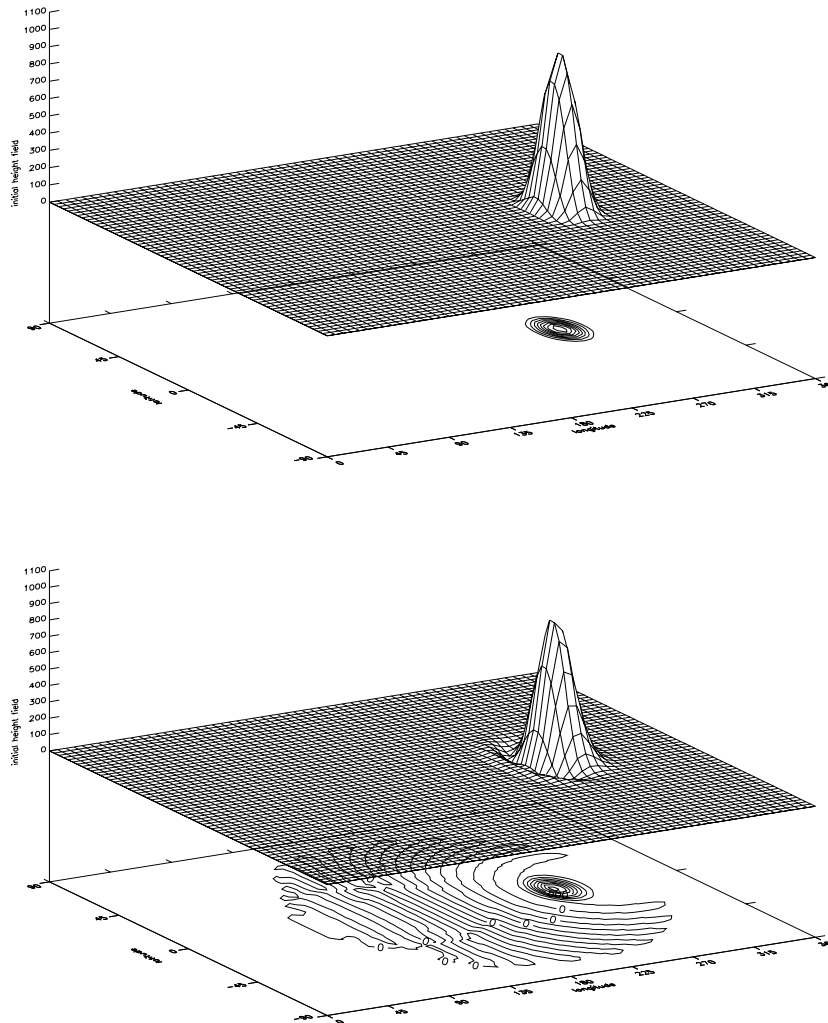

Figure 4.2: Initial state and final state of the advecting cosine bell ($\alpha = 0, m = 5, \Delta t = 900$ s), contour interval 100 m
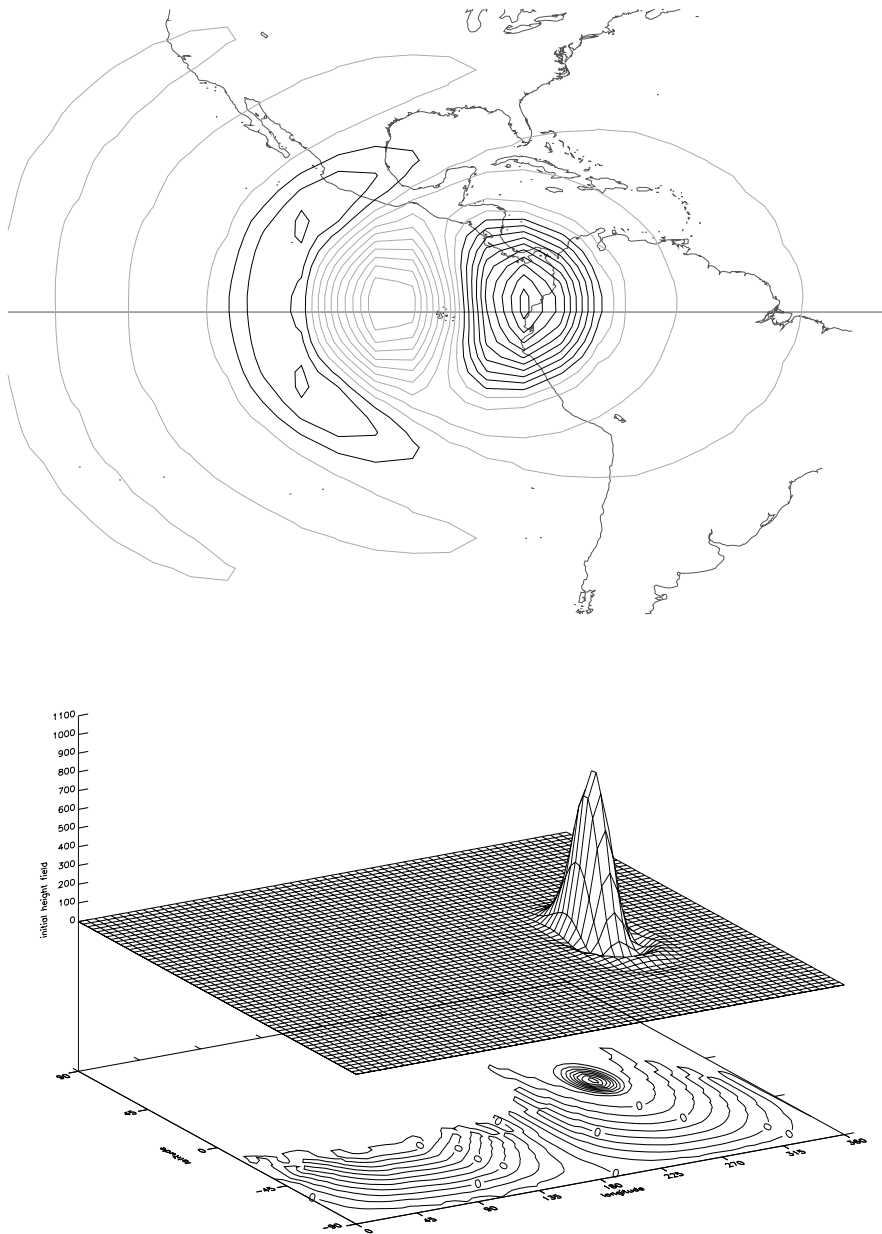
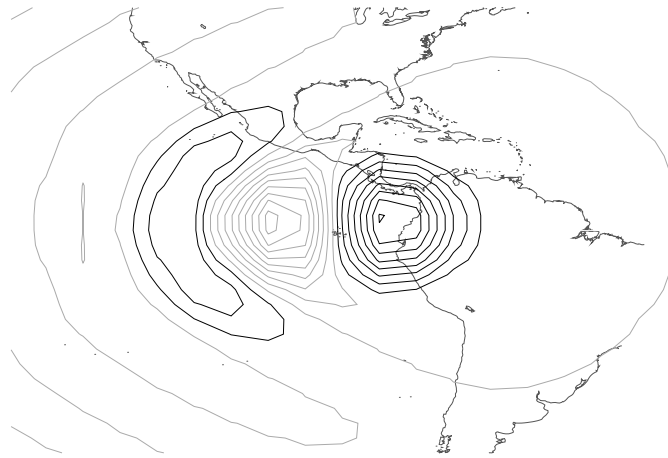Figure 4.3: Above: difference between initial and final state of the cosine bell ($\alpha = 0, m = 5, \Delta t = 900$), contour interval 20 m (solid lines negative, dashed lines positive); below: final state of the cosine bell ($\alpha = \frac{\pi}{2}$, $m = 5$, $\Delta t = 900$ s), contour interval 100 m
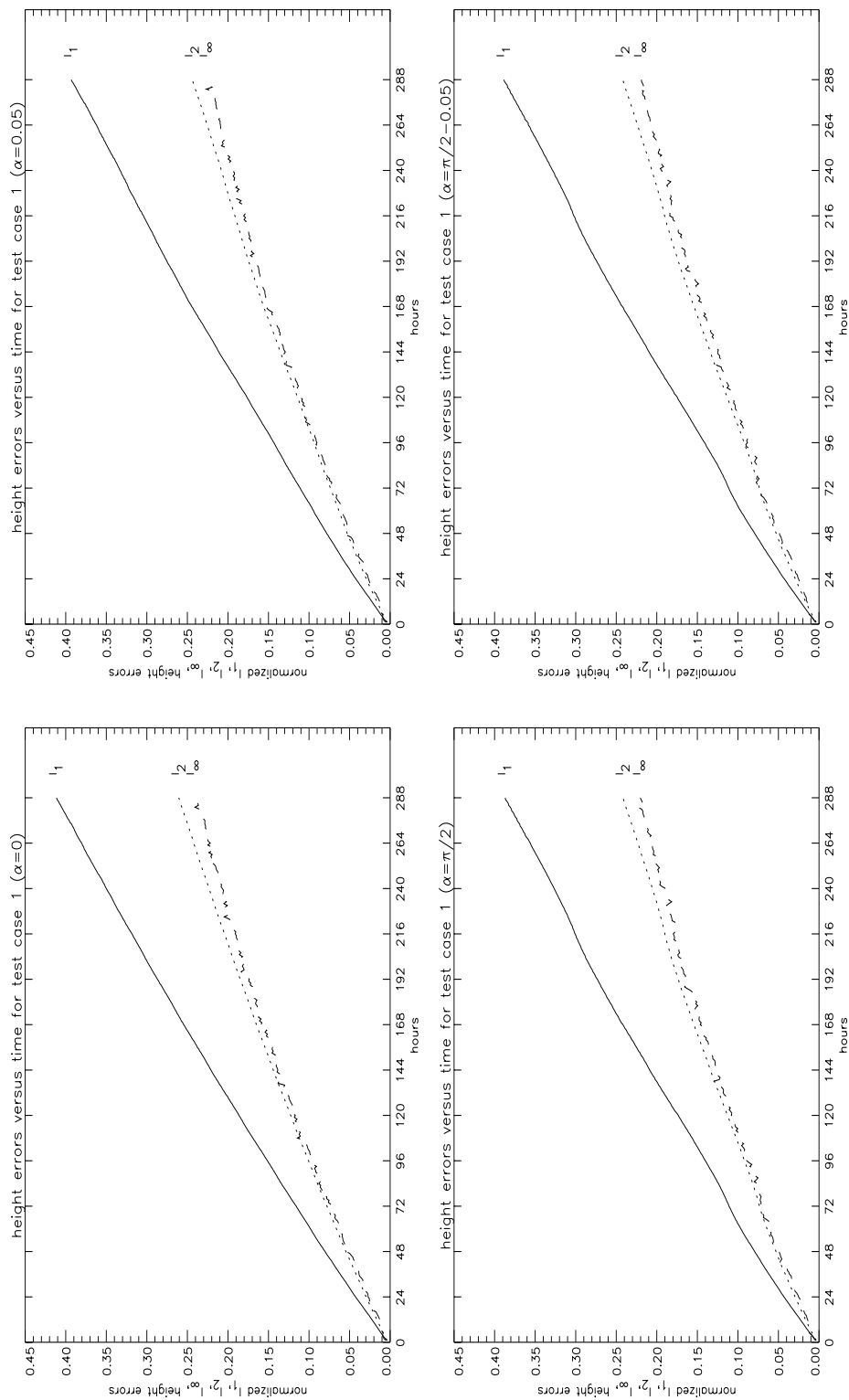
Figure 4.4: Height error norms for the advection of the cosine bell ($m = 5$, $\Delta t = 900$ s)
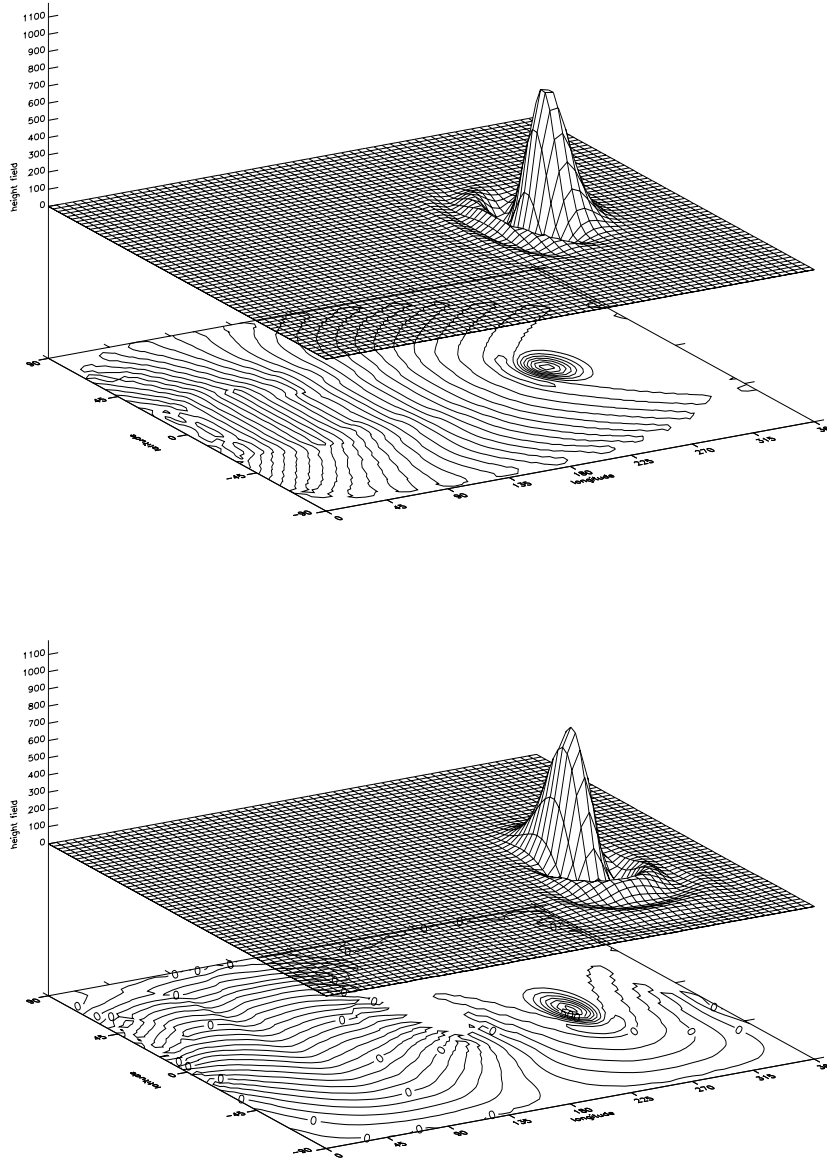
Figure 4.5: Final state of the cosine bell ($m = 5$, $\alpha = 0.0$ and $\alpha = \frac{\pi}{2}$, $\Delta t = 900$), contour interval 100 m, modified program

Figure 4.6: Height difference between initial and final state of the cosine bell ($\alpha = 0, m = 5, \Delta t = 900$), contour interval 50 m (solid lines negative, dashed lines positive), modified program
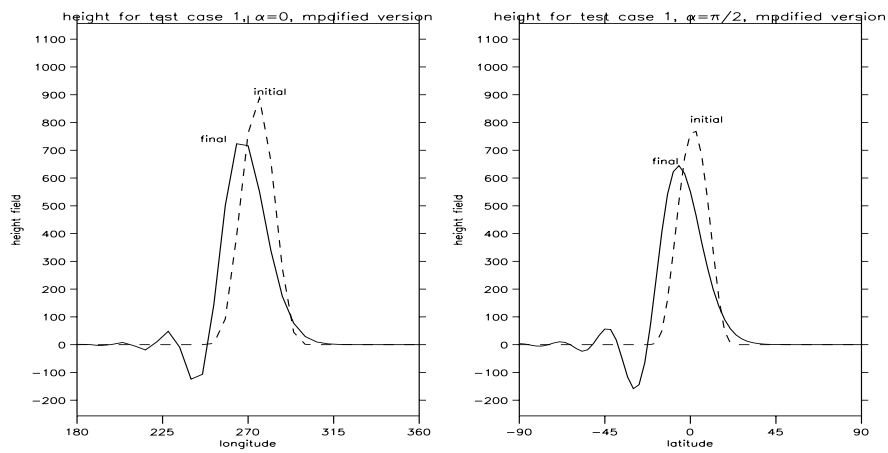
Figure 4.7: Longitudinal and latitudinal cut through the initial and final cosine bells for $\alpha = 0$ and $\alpha = \frac{\pi}{2}$, respectively, modified program
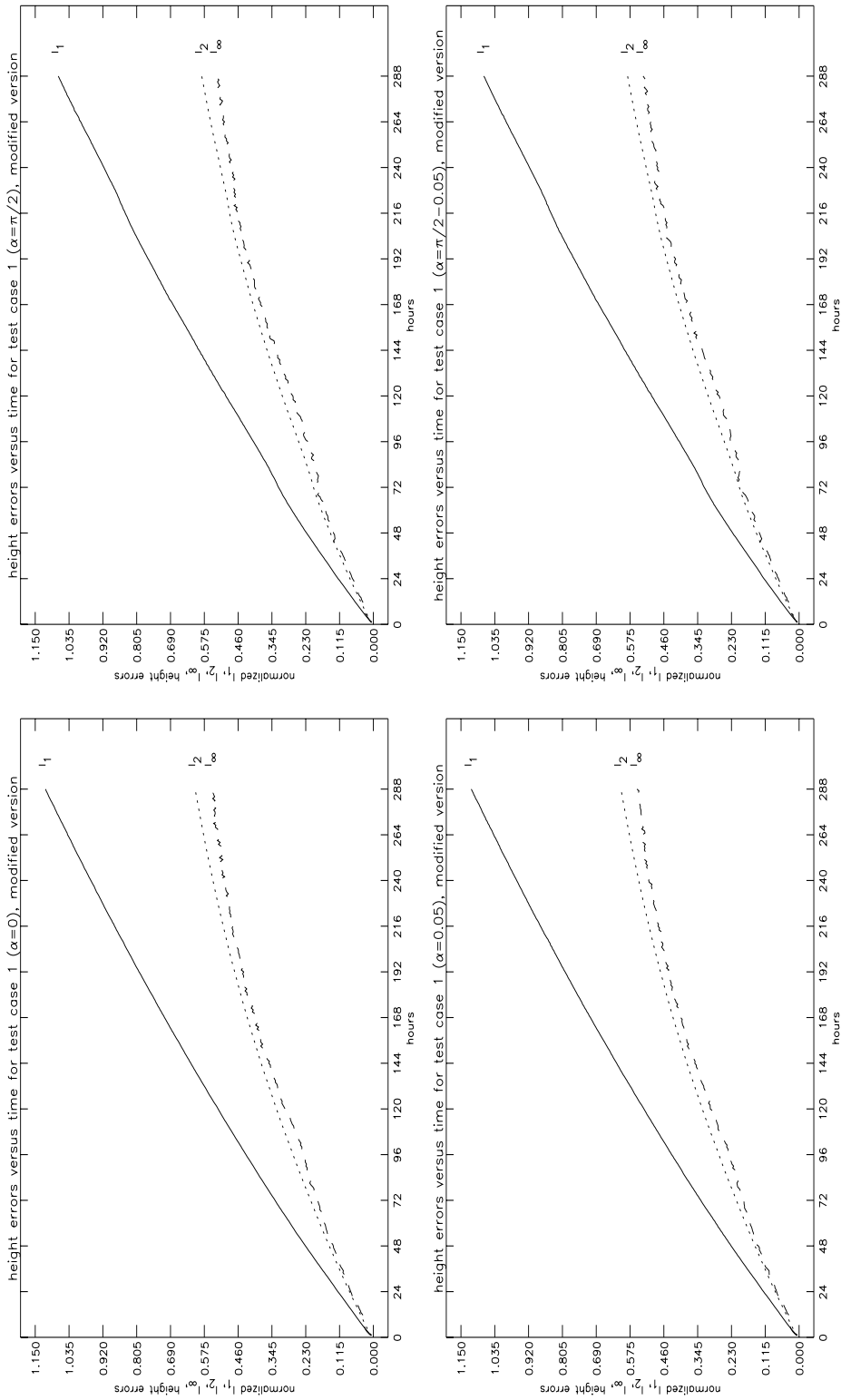
Figure 4.8: Height error norms for the advection of the cosine bell ($m = 5$, $\Delta t = 900$ s), modified program

4.2   Steady State Geostrophic Flow

This test case is a steady state solution to the non-linear shallow water equations. Because of the smoothness of the geopotential height and the wind field this example is a trivial test for spectral methods. Even for low resolutions the solution is approximated well. The test is performed using the standard parameter as specified in [6].

Starting from the specifications of u, v and h as required we have after transformation to Cartesian coordinates the same initialization for u, v and w as in test case 1. The geopotential height is given by

$$h = h_0 - \left(R_{earth} \Omega u_0 + \frac{1}{2} u_0^2 \right) (- \cos \lambda \cos \theta \sin \alpha + \sin \theta \cos \alpha)^2$$

with $h_0 = 2.94 \cdot 10^4 m^2 s^{-2}$, u_0 and α, respectively, as in test case 1.

Table 4.5 shows the results concerning relative mass and energy for the original time stepping. For the coarse resolution $m = 3$ the time step size of 3600 seconds runs into stability problems for any angle α. Table 4.5 gives the time step sizes for which stable results were obtained. The possible time steps are smaller than those used for experiments with spectral methods. The results are independent from the angle used.

For this test case the modified time stepping allows an extremely enlarged time step size. Again, the results are independent from α. Therefore results using coarser resolutions $m = 3$ and $m = 4$ are reported only for $\alpha = 0.0$. Even with a time step size which is more than six times larger for $m = 5$ the final results are stable. The mass is conserved more or less exactly, while the development of the energy shows a nearly linear increase. This gain of energy is reduced when time steps with $\Delta t = 675$ s are used. Compared to the original version the new time stepping enables larger time steps, which now are even larger than the usually used Δt for the spectral methods. Figure 4.9 shows the initial height fields for the test situations using the angles $\alpha = 0.0$ and $\alpha = \frac{\pi}{2}$. The development of the error is reported in Figure 4.10.

The structure of the error reflects to a certain degree also the underlying structure of the grid. Ten of the initial discretization points on the initial icosahedron can be recognized. These are points, where only five neighboring cells exist. Such a symmetry is not only observed for test case 2, but also for test case 3. This phenomenon is presented in Figure 4.18, looking at the north pole. The height- and wind-errors in Figures 4.11 and 4.12, respectively, are small and show a reasonable development. For the modified program the errors are again larger than for the original version. The reported results in Figures 4.14 and 4.15 refer to $m = 5$ with $\Delta t = 675$ s. The enlarged errors are explained by the larger time steps. In Table 4.5 the results for the modified program give the impression of stability for all the time step sizes. But the height and wind errors with $\Delta t = 900$ s show an unstable behavior after approximately 200 hours (Figures 4.14 and 4.15). This time step therefore is too large for this test on refinement depth $m = 5$.

angle	m	Δt	after 2 days		after 5 days		after 10 days	
			E	M	E	M	E	M
$\alpha = 0$	3	3600	0.992	0.998	0.980	0.993	1.617	0.795
	3	1800	0.991	0.999	0.976	0.997	0.952	0.994
	4	450	0.998	1.000	0.994	0.999	0.989	0.998
	5	120	0.999	1.000	0.999	1.000	0.997	1.000
$\alpha = 0.05$	3	3600	0.992	0.997	0.980	0.993	1.612	0.803
	3	1800	0.991	0.999	0.976	0.997	0.952	0.994
	4	450	0.998	1.000	0.994	0.999	0.989	0.998
	5	120	0.999	1.000	0.999	1.000	0.997	1.000
$\alpha = \frac{\pi}{2}$	3	3600	0.992	0.997	0.980	0.992	divergent	
	3	1800	0.990	0.999	0.975	0.997	0.951	0.994
	4	450	0.998	0.999	0.994	0.999	0.988	0.998
	5	120	0.999	0.999	0.999	0.999	0.997	0.999
$\alpha = \frac{\pi}{2} - 0.05$	3	3600	0.992	0.997	0.980	0.993	5.017	0.869
	3	1800	0.990	0.999	0.975	0.997	0.950	0.994
	4	450	0.998	1.000	0.994	0.999	0.988	0.998
	5	120	0.999	1.000	0.999	1.000	0.997	1.000
modified program								
$\alpha = 0.0$	3	3600	1.007	1.000	1.018	1.000	1.037	1.001
	4	1800	1.005	1.000	1.014	1.000	1.028	1.000
	5	900	1.003	1.000	1.008	1.000	1.017	1.000
	5	675	1.002	1.000	1.006	1.000	1.011	1.000
$\alpha = 0.05$	5	900	1.003	1.000	1.008	1.000	1.017	1.000
	5	675	1.002	1.000	1.006	1.000	1.011	1.000
$\alpha = \frac{\pi}{2}$	5	900	1.004	0.999	1.010	0.999	1.020	0.999
	5	675	1.003	1.000	1.007	1.000	1.014	0.999
$\alpha = \frac{\pi}{2} - 0.05$	5	900	1.004	1.000	1.010	0.999	1.020	0.999
	5	675	1.003	1.000	1.007	1.000	1.014	0.999

Table 4.5: Zonal geostrophic flow; relative conservation of energy and mass, original and modified program
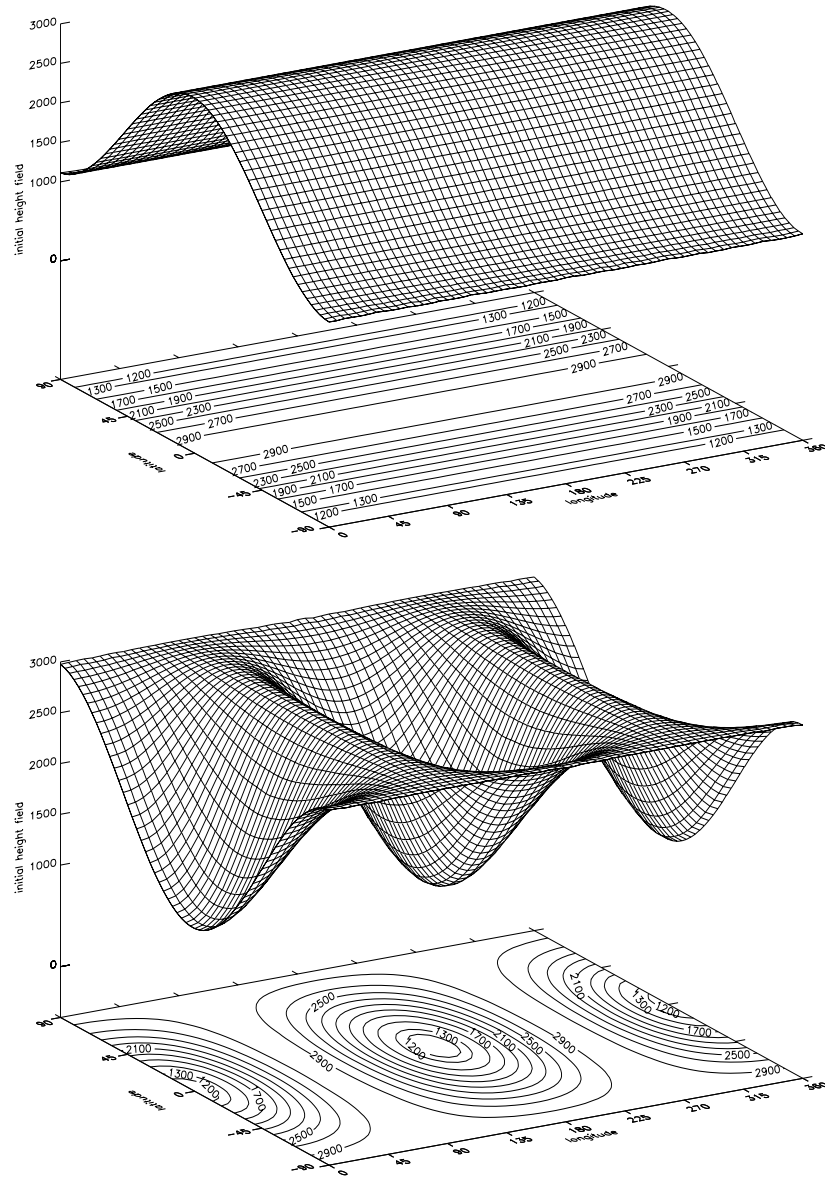
Figure 4.9: Initial state for zonal flow ($\alpha = 0.0$ and $\alpha = \frac{\pi}{2}$)
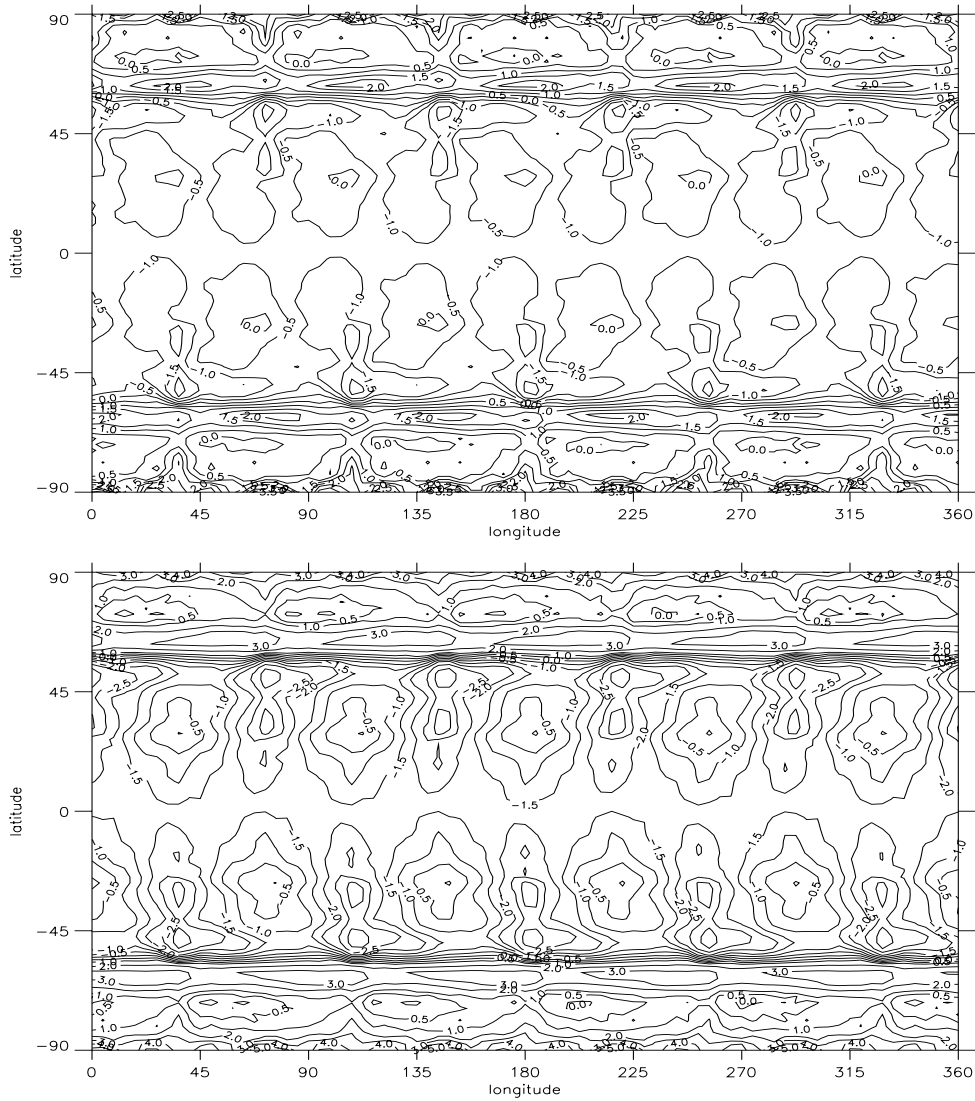
Figure 4.10: Zonal flow, height errors after 120 (top) and 240 hours (below), ($\alpha = 0.0$), $\Delta t = 120$ s
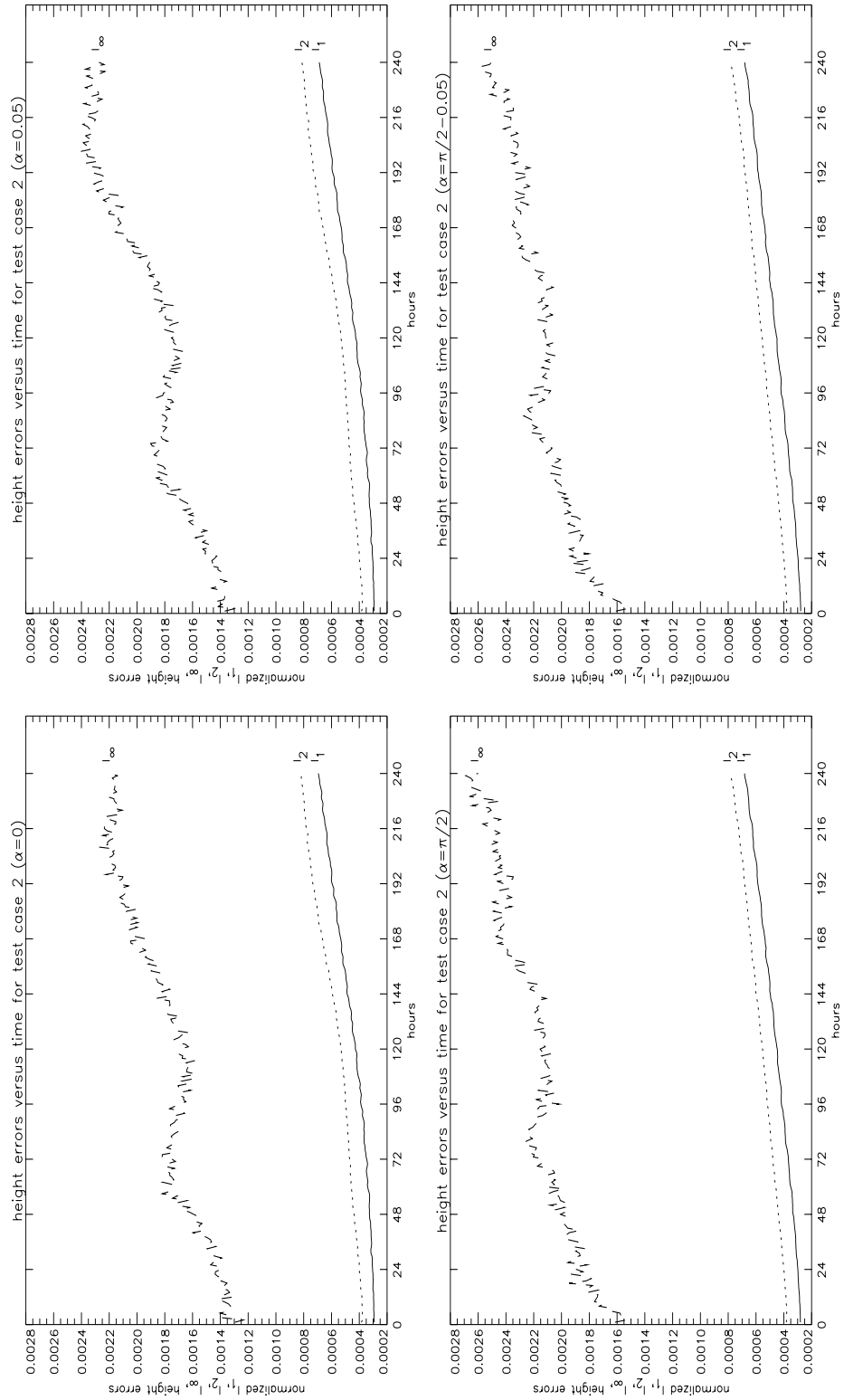
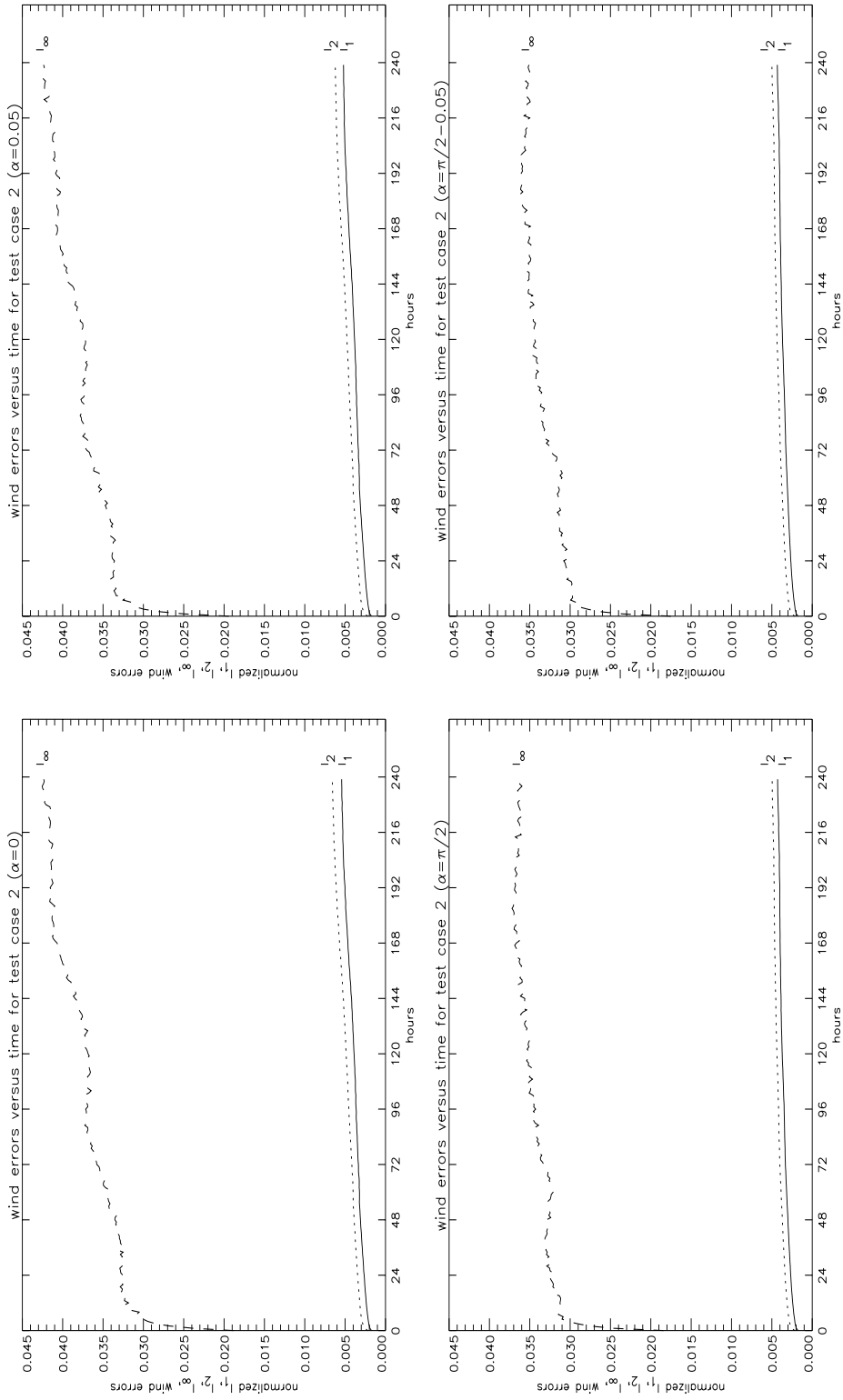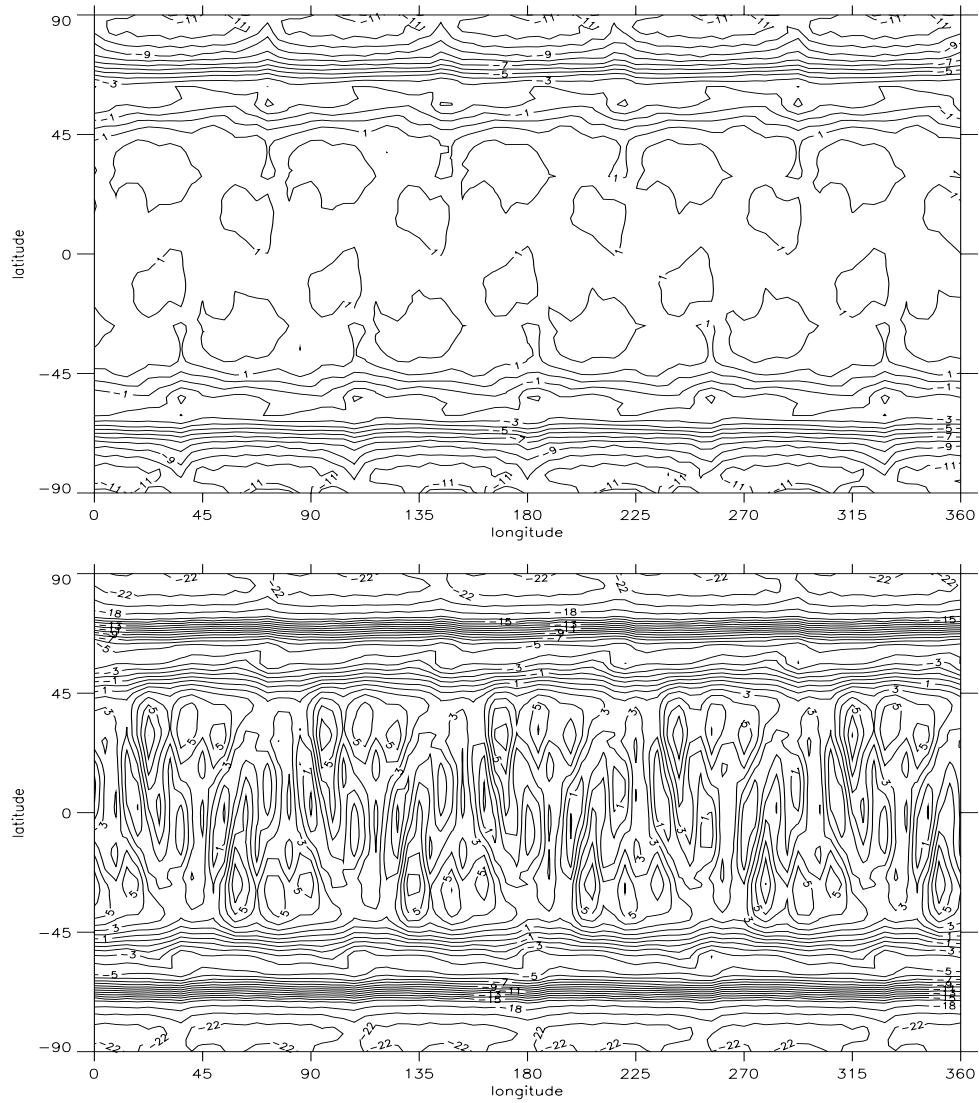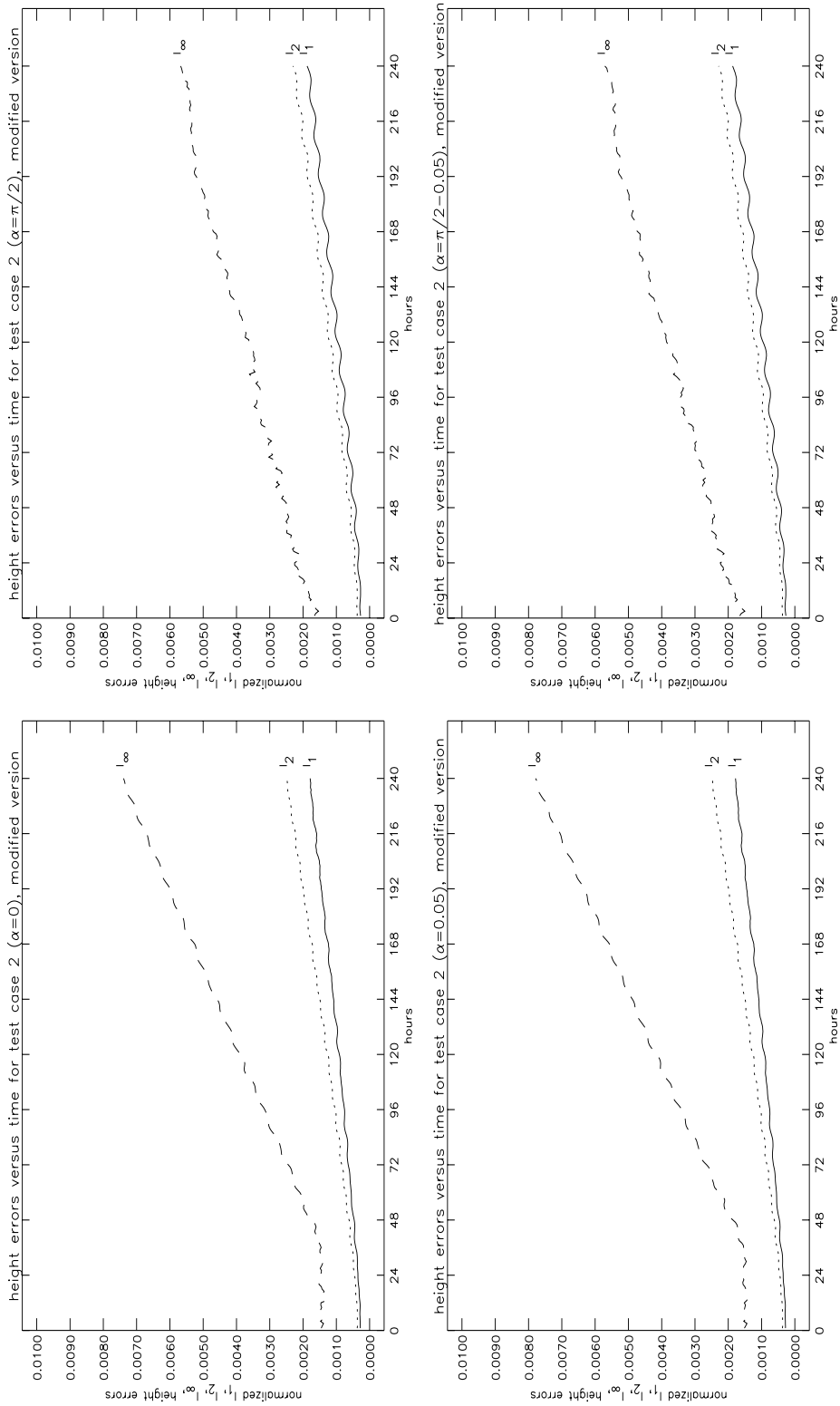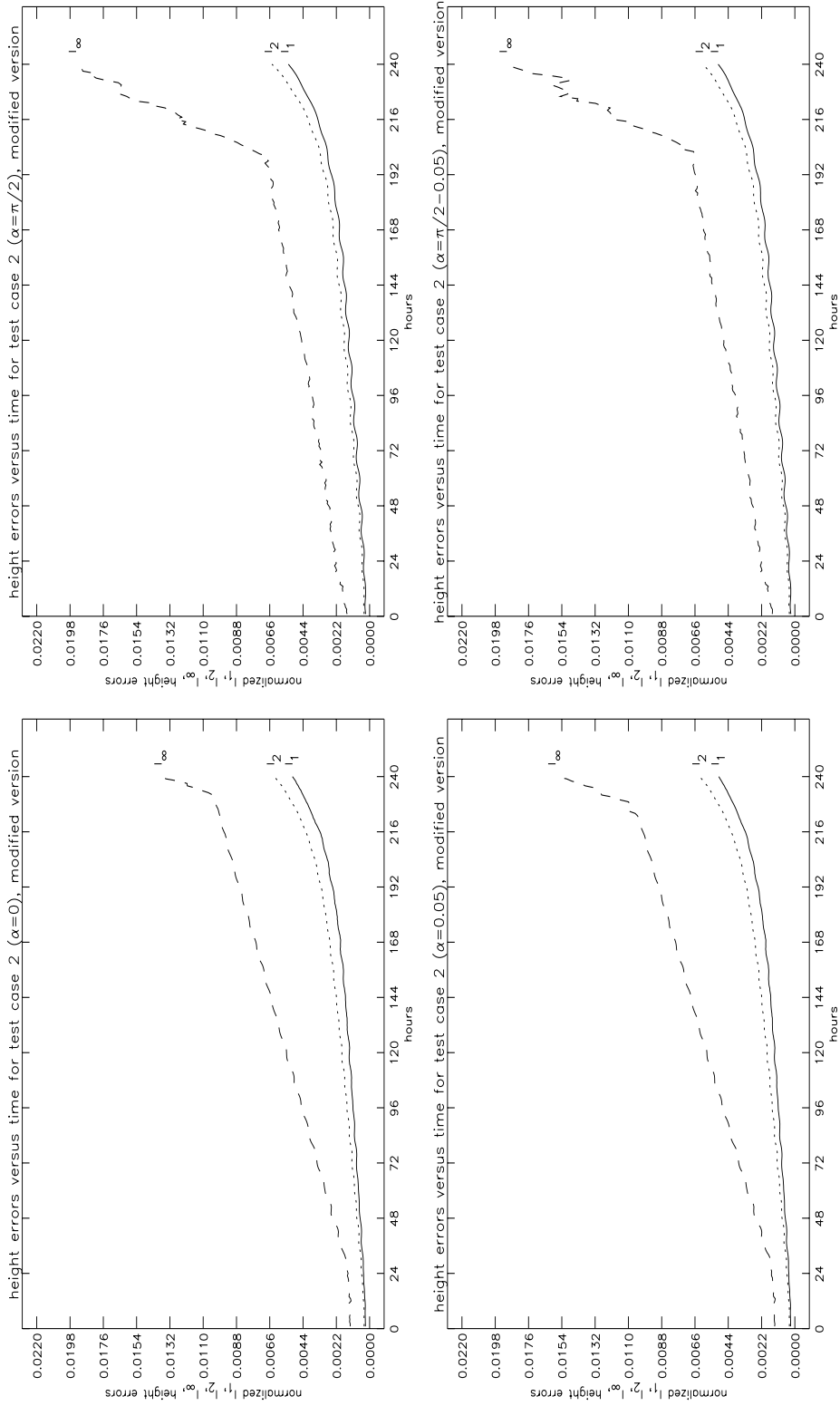Figure 4.11: Zonal flow, height error norms for all α, $\Delta t = 120$ s

Figure 4.12: Zonal flow, wind error norms for all α, $\Delta t = 120$ s

Figure 4.13: Zonal flow, height errors after 120 (top) and 240 hours (below), ($\alpha = 0.0$), $\Delta t = 675$ s, modified program

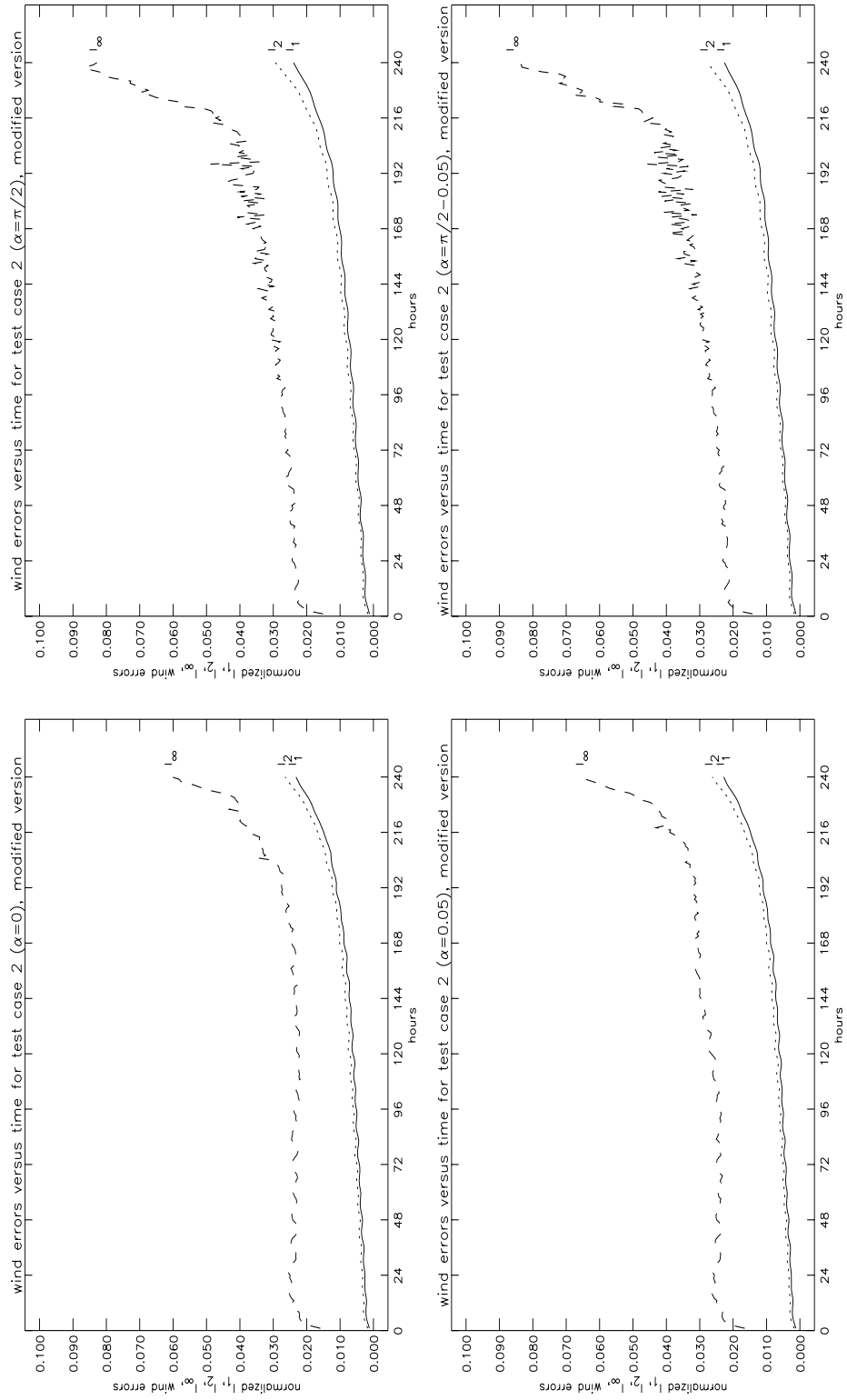Figure 4.14: Zonal flow, height error norms for all α, $\Delta t = 675$ s, modified program
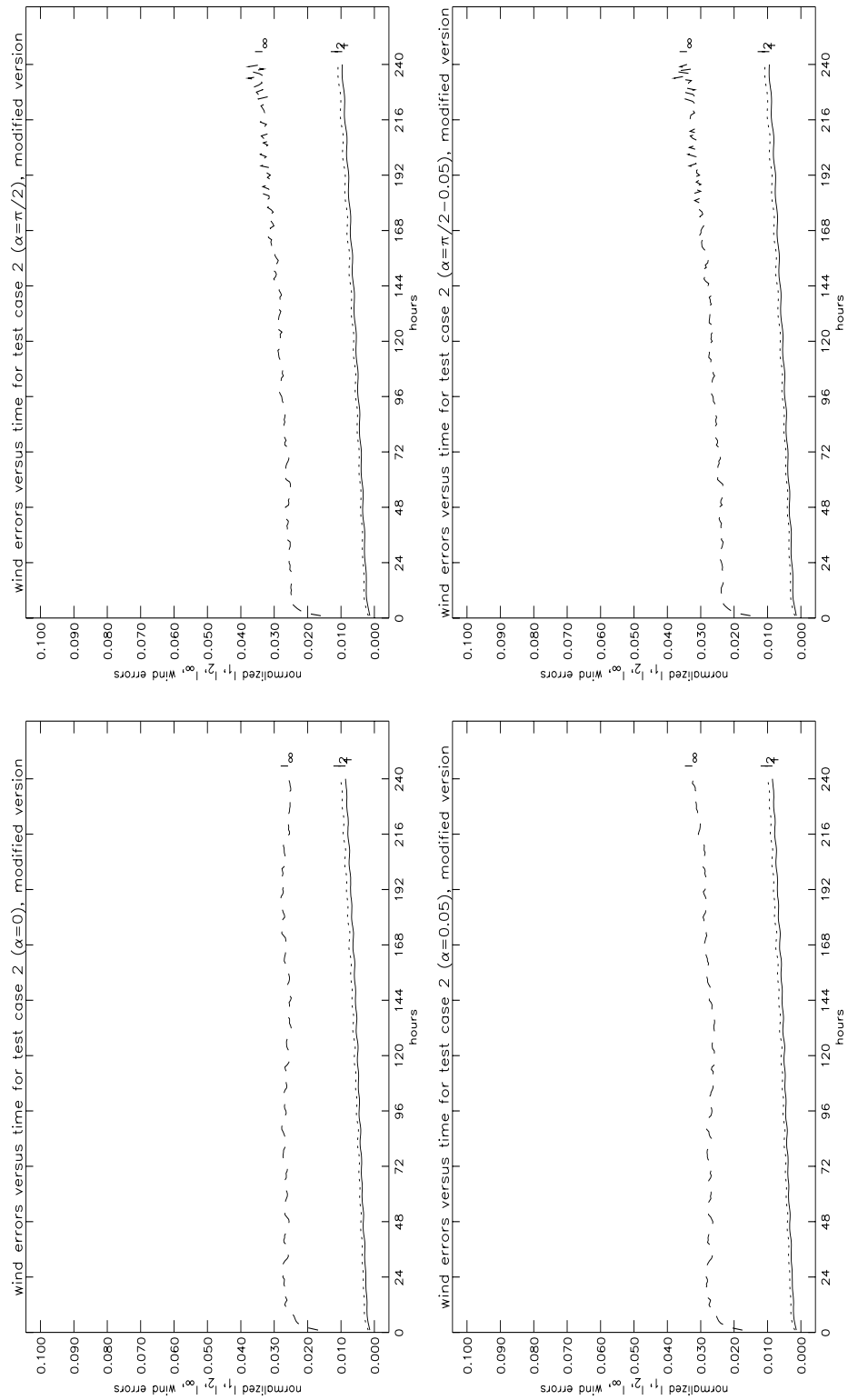
Figure 4.15: Zonal flow, wind error norms for all α, $\Delta t = 675$ s, modified program

Figure 4.16: Zonal flow, height error norms for all α, $\Delta t = 900$ s, modified program

Figure 4.17: Zonal flow, wind error norms for all α, $\Delta t = 900$ s, modified program
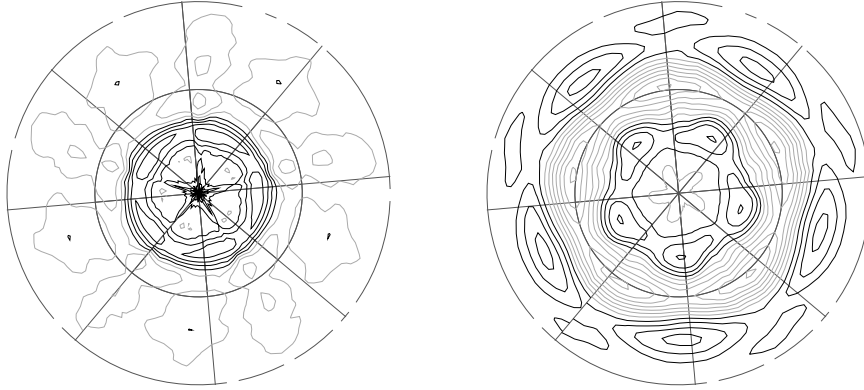
Figure 4.18: Symmetry of the height errors after ten days due to the space discretization, (test case 2 left and test case 3 right)

4.3   Steady State Geostrophic Flow with Compact Support

This case is a steady state solution to the non-linear shallow water equations. Because of the smoothness of the geopotential height and the wind field this example is a trivial test for spectral methods. Similarly to the test case 2, for principal reasons grid point approaches cannot be expected to work as good on this problem as spectral methods do. Even for low resolutions the solution is approximated well. The test is performed using the standard parameter due to [6]. The problem description is as specified in Section 4.2. After transformation of the initial conditions due to [6] the velocities in Cartesian coordinates are:

$$
\begin{aligned}
U &= -\sin\lambda \cdot u \\
V &= \cos\lambda \cdot u \\
W &= 0
\end{aligned}
$$

The height field is used as given in [6].

   To produce stable results with the unchanged algorithm the time step size has to be

angle	m	Δt	after 2 days		after 5 days		after 10 days	
			E	M	E	M	E	M
$\alpha = 0$	3	3600	0.961	0.999	0.922	0.999	0.875	0.998
	4	1800	0.993	1.000	0.986	0.999	4.642	0.981
	4	900	0.992	1.000	0.981	1.000	0.965	0.999
	5	225	0.993	1.000	0.996	1.000	0.992	1.000
modified program								
$\alpha = 0$	3	3600	0.975	1.000	0.956	1.000	0.940	1.000
	4	3600	1.012	1.000	1.031	1.000	1.065	0.999
	5	1800	1.007	1.000	1.019	1.000	1.038	1.000

Table 4.6: Zonal geostrophic flow with compact support; relative conservation of energy and mass, original and modified program

considerably smaller than expected, as in the previous case. The improved version of the program is able to use time steps which are three times larger than for the reported spectral methods. For this case the time step sizes can be increased by a factor of about 4 for $m = 4$ and even more for $m = 5$.

Figure 4.19 shows the initial wind and height fields, while Figure 4.20 reports the development of the height error. Looking to the wind and height errors again, we have acceptable small errors, which are again larger for the modified program. But one should keep in mind the considerably larger time steps.
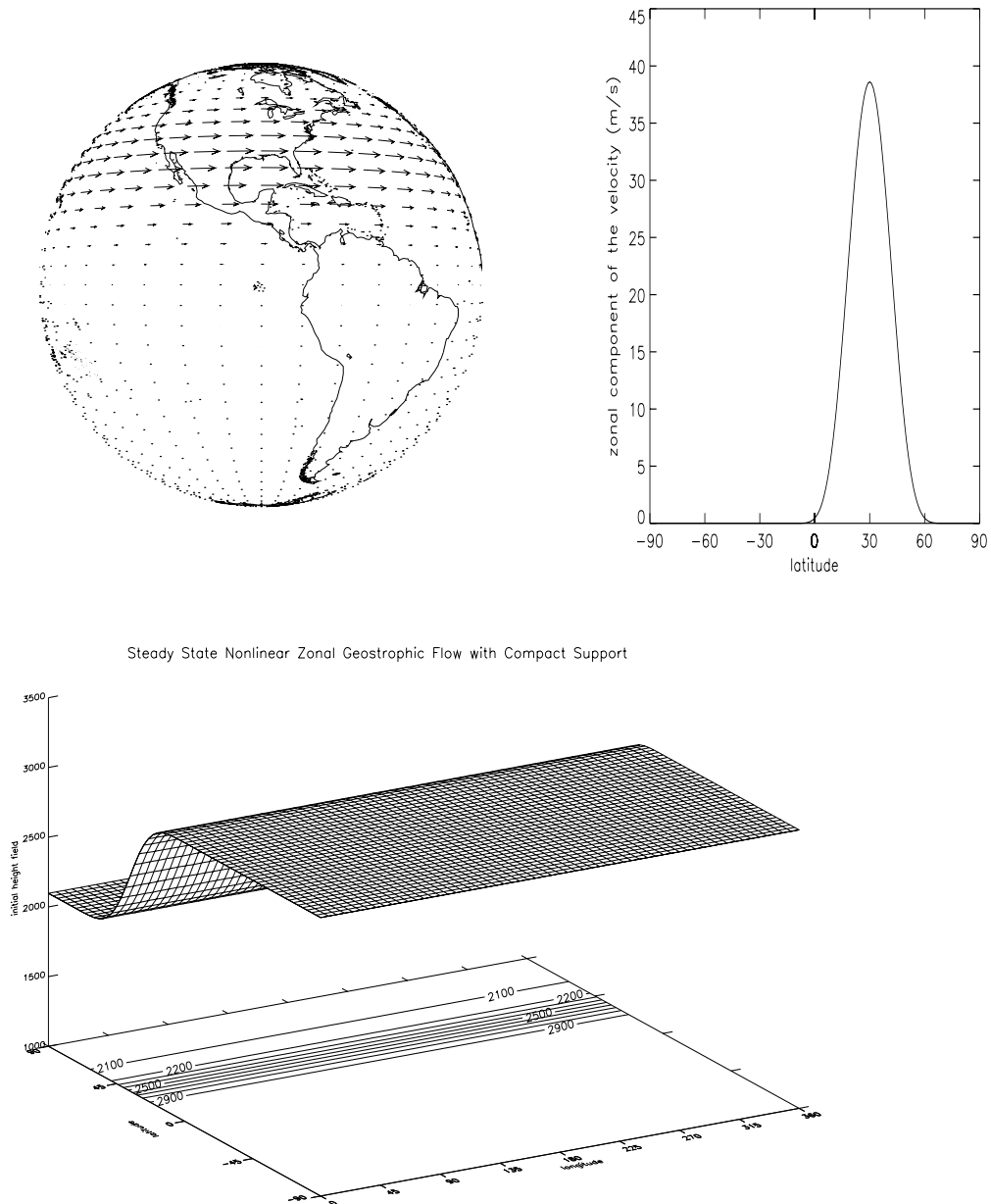
Figure 4.19: Zonal flow with compact support, initial wind (above) and height field (below) , $\Delta t = 225$ s, contour interval 100 m
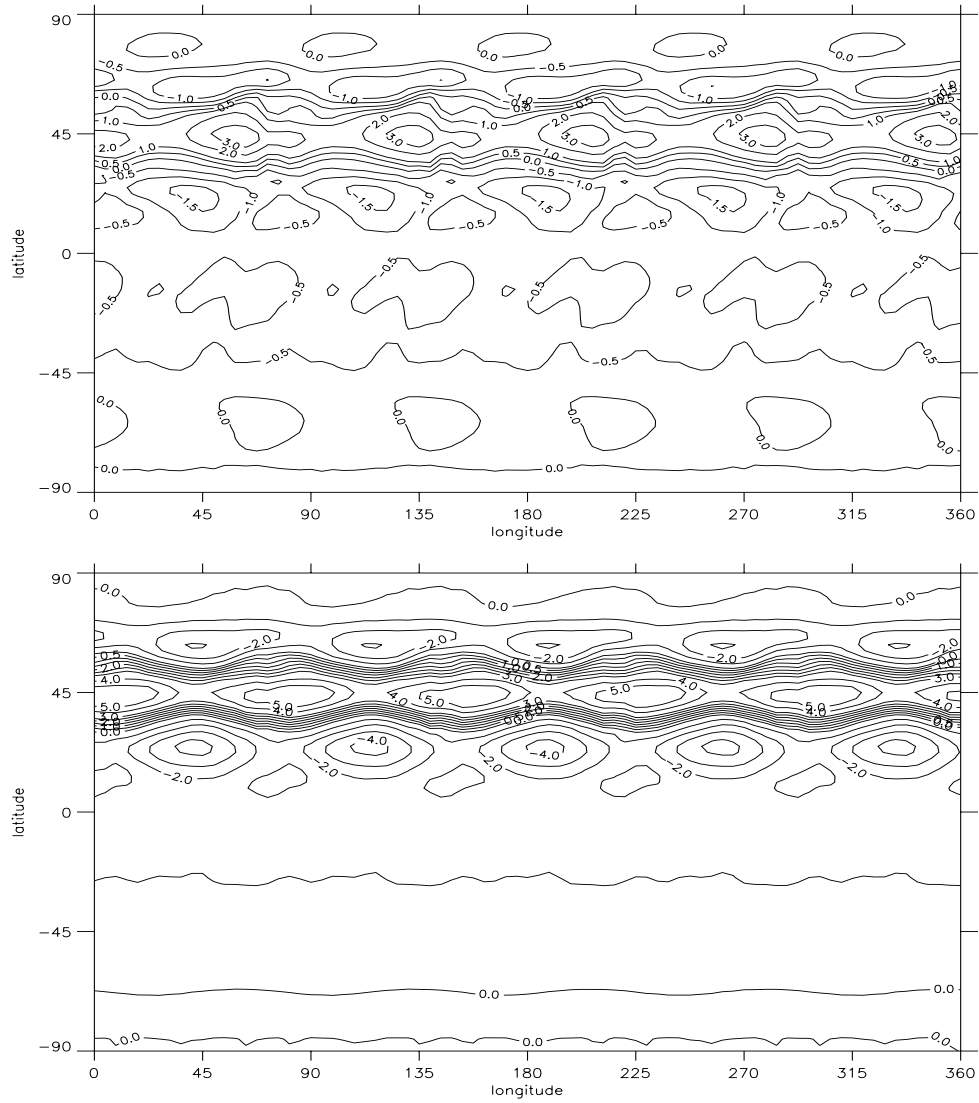
Figure 4.20: Zonal flow with compact support, height errors after 120 (top) and 240 hours (below), $\Delta t = 225$ s
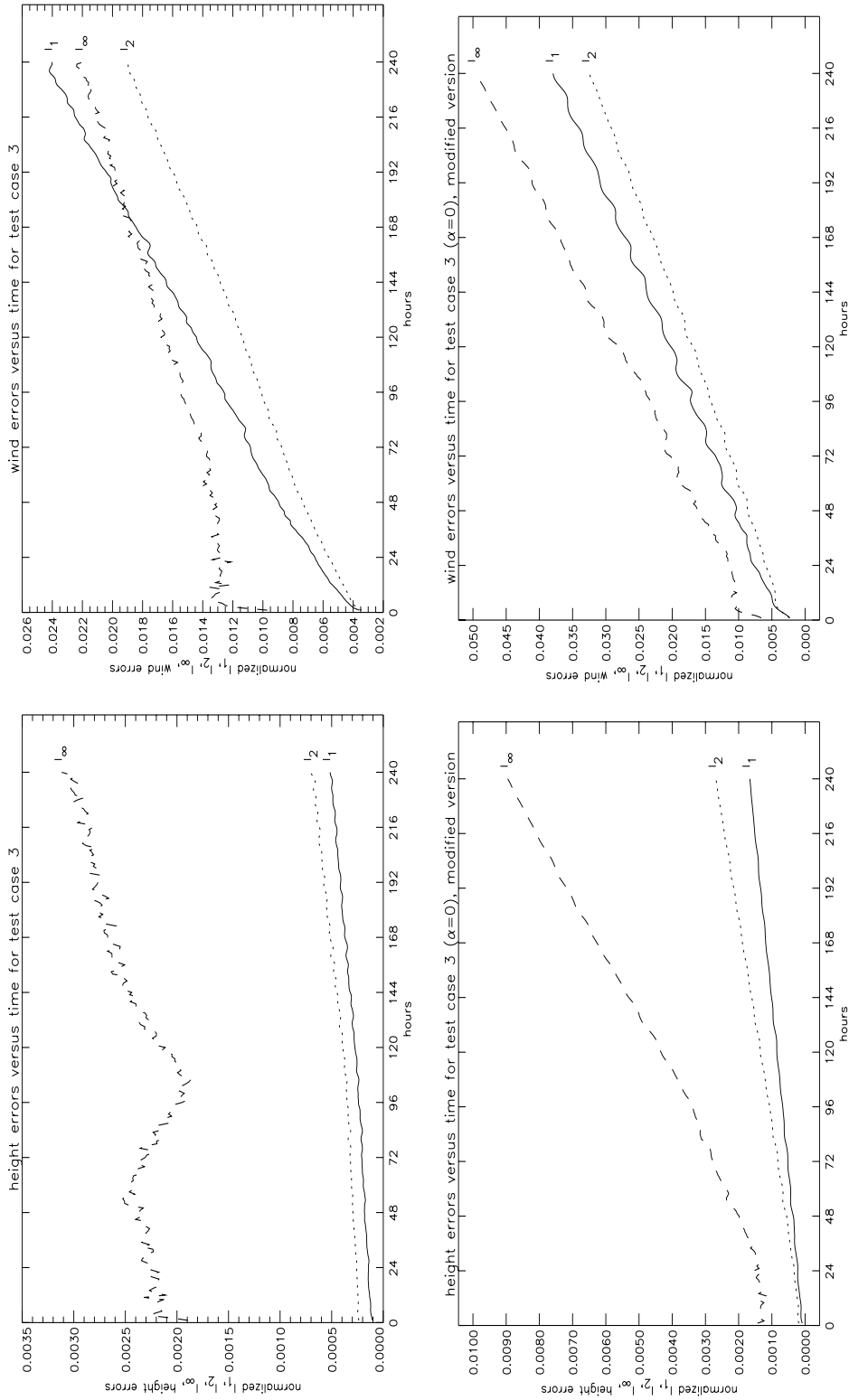
Figure 4.21: Zonal flow with compact support; height and wind error norms $\Delta t = 225$ s (original) and $\Delta t = 1800$ s (modified)
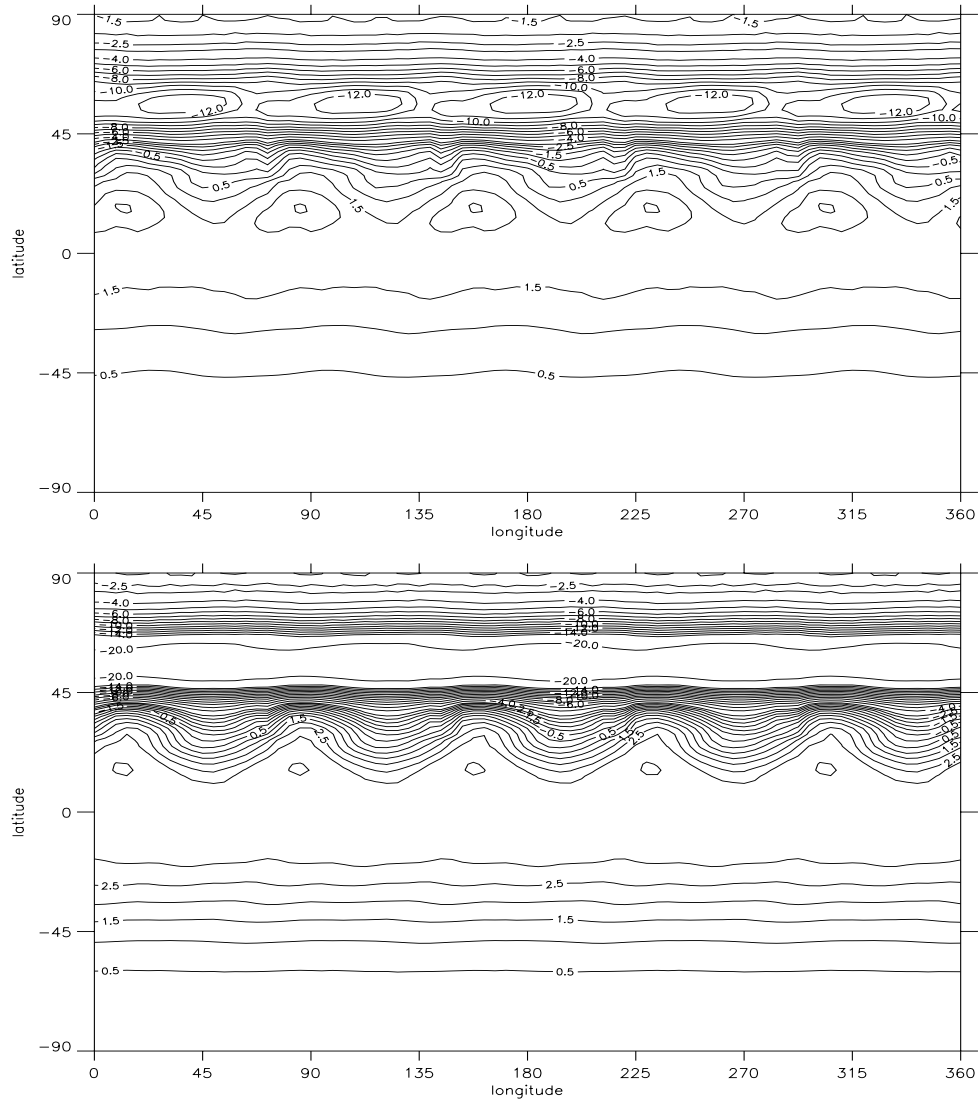
Figure 4.22: Zonal flow with compact support, height errors after 120 (top) and 240 hours (below), $\Delta t = 1800$ s, modified program

4.4   Zonal Flow over an Isolated Mountain

A first approximation to realism is the usage of some artificial topography. The center of an artificial mountain is placed at the position $\lambda = \frac{3}{2}\pi$ and $\varphi = \frac{\pi}{6}$. The maximal height is 2000 m.
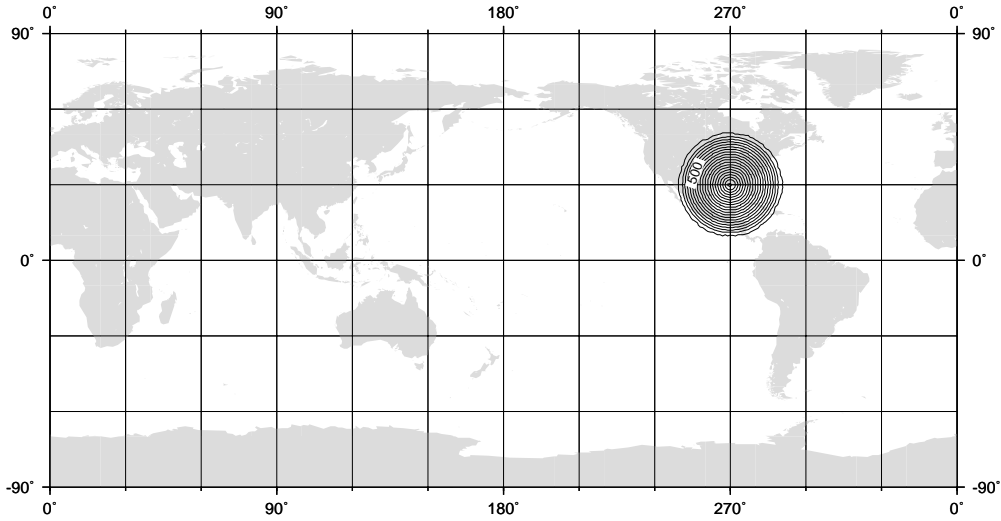

Figure 4.23: Zonal flow over an isolated mountain; topography (contour interval 100 m)

After transformation to Cartesian coordinates the initial wind field is given by

$$
\begin{aligned}
U &= -u_0 \cos\varphi \sin\lambda \\
V &= u_0 \cos\varphi \cos\lambda \\
W &= 0
\end{aligned}
$$

A similar wind field has also been used in test cases 1 and 2 for $\alpha = 0$. Here we use the same definitions with $u_0 = 20.0 ms^{-1}$. The height field is used as given in [6].

This test case has no analytical solution. Therefore, an error estimation requires a reference solution which has to be computed by some other solving method using a fine resolution. The reference solutions used in this and the following two test cases are taken from the spectral transform shallow water model described in [2]. They are provided for each day and therefore the error norms are calculated in intervals of 24 hours. The forecast for this test case is computed for ten days.

Table 4.7 contains the relative conservation of the initial values of energy and mass. With the original program, stable results can be produced with the specified Δt . To produce stable results with the modified version, the time step size can be chosen up to

m	Δt	after 2 days		after 5 days		after 10 days	
		E	M	E	M	E	M
3	1800	0.988	1.000	0.951	1.000	0.869	1.000
4	900	1.000	1.000	0.985	1.000	0.956	1.000
5	225	1.002	1.000	0.998	1.000	0.997	1.000
modified program							
3	3600	1.027	1.000	1.053	1.001	1.083	1.001
4	3600	1.033	1.000	1.079	1.000	1.168	1.001
4	1800	1.016	1.000	1.030	1.000	1.047	1.000
5	1800	1.018	1.000	1.039	1.000	1.080	1.000
5	900	1.010	1.000	1.018	1.000	1.036	1.000

Table 4.7: Zonal flow over an isolated mountain; relative conservation of energy and mass, original and modified program

$\Delta t = 1800$ s, which is eight times higher than for the original program. This is much larger than the time stepping in the referenced spectral model ($\Delta t = 600$ s). Comparing the results (see table 4.7) in case of $\Delta t = 1800$ s and $\Delta t = 900$ s there is a small increase of the energy. Furthermore the error norms are up to two times higher for $\Delta t = 1800$ s. Therefore we decided to present only the graphs for $\Delta t = 900$ s in case of the modified program. Here the time step size is still four times larger than that of the original program and 1.5 times larger than for the spectral model. Nevertheless the error norms of the spectral model and BARGLO have the same order.
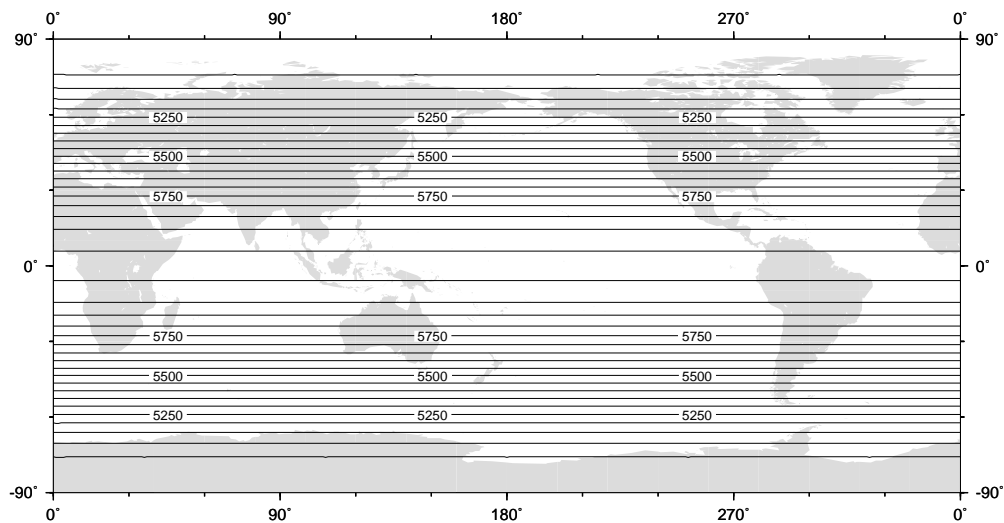

Figure 4.24: Zonal flow over an isolated mountain; initial height field with incorporated topography $(h + h_s)$, contour interval 50 m

The initialization of the height field and the reference solutions for day five and day ten are presented in Figures 4.24 and 4.25. The development of the height field as computed by the original program using $\Delta t = 225$ s and the deviations to the reference solutions at day five and ten are shown in Figures 4.26 and 4.27. The corresponding results for the modified program using $\Delta t = 900$ s are shown in Figures 4.29 and 4.30. The graphs of the error norms are provided in Figure 4.28. Although the increased time stepping used in the modified version leads to larger error norms, the errors still have a reasonable size. Further investigation for a better choice of the diffusion constant may improve the results, especially in this and the next two test cases.
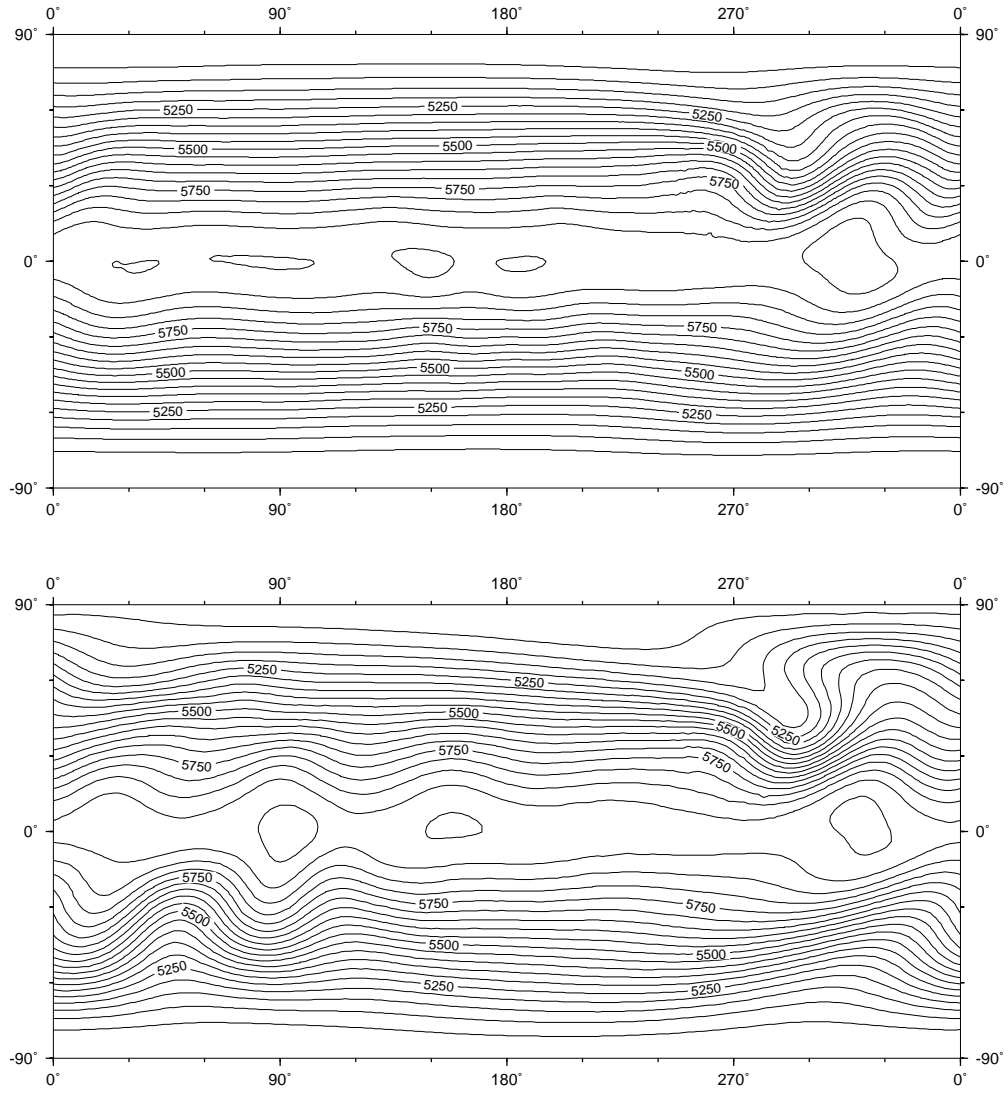
Figure 4.25: Zonal flow over an isolated mountain; reference height field $(h + h_s)$ after 120 (top) and 240 hours (below), contour interval 50 m
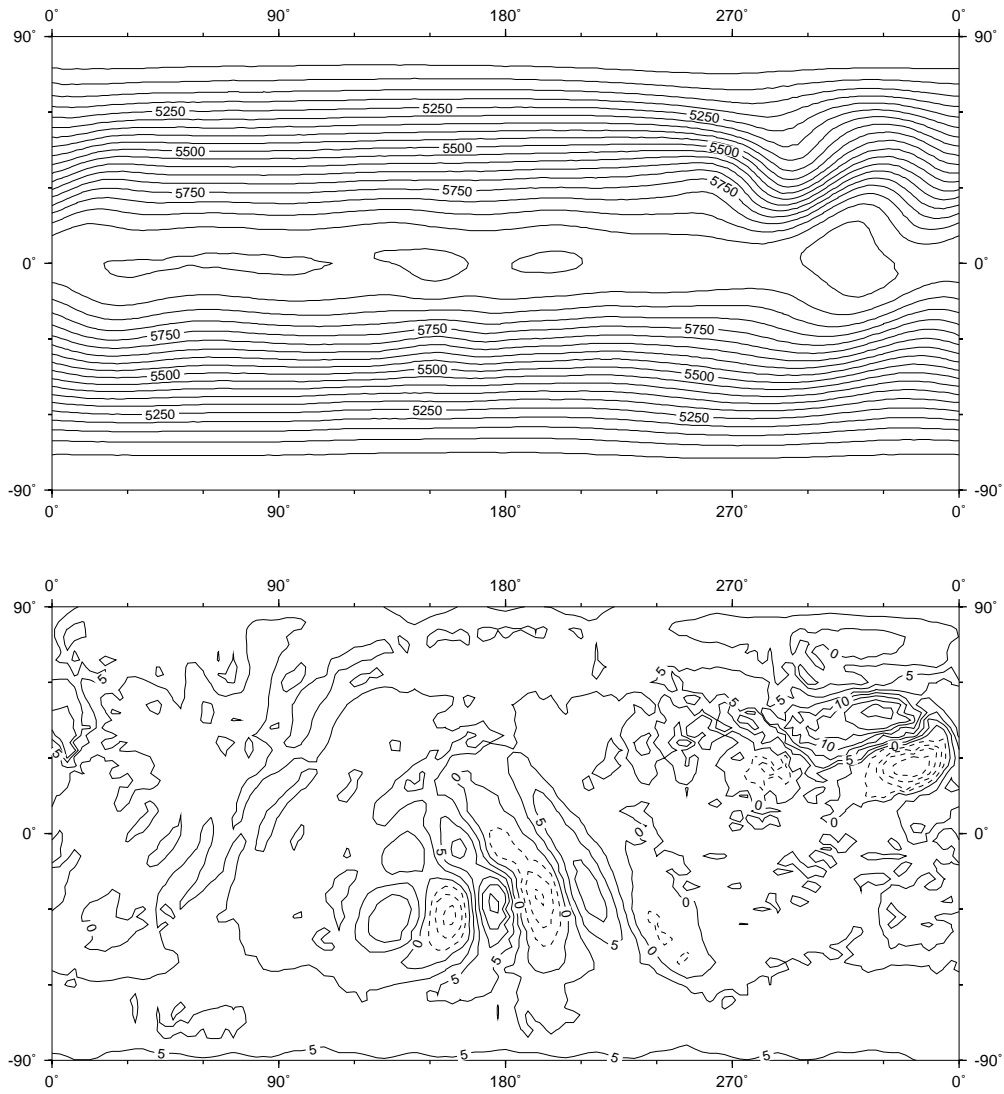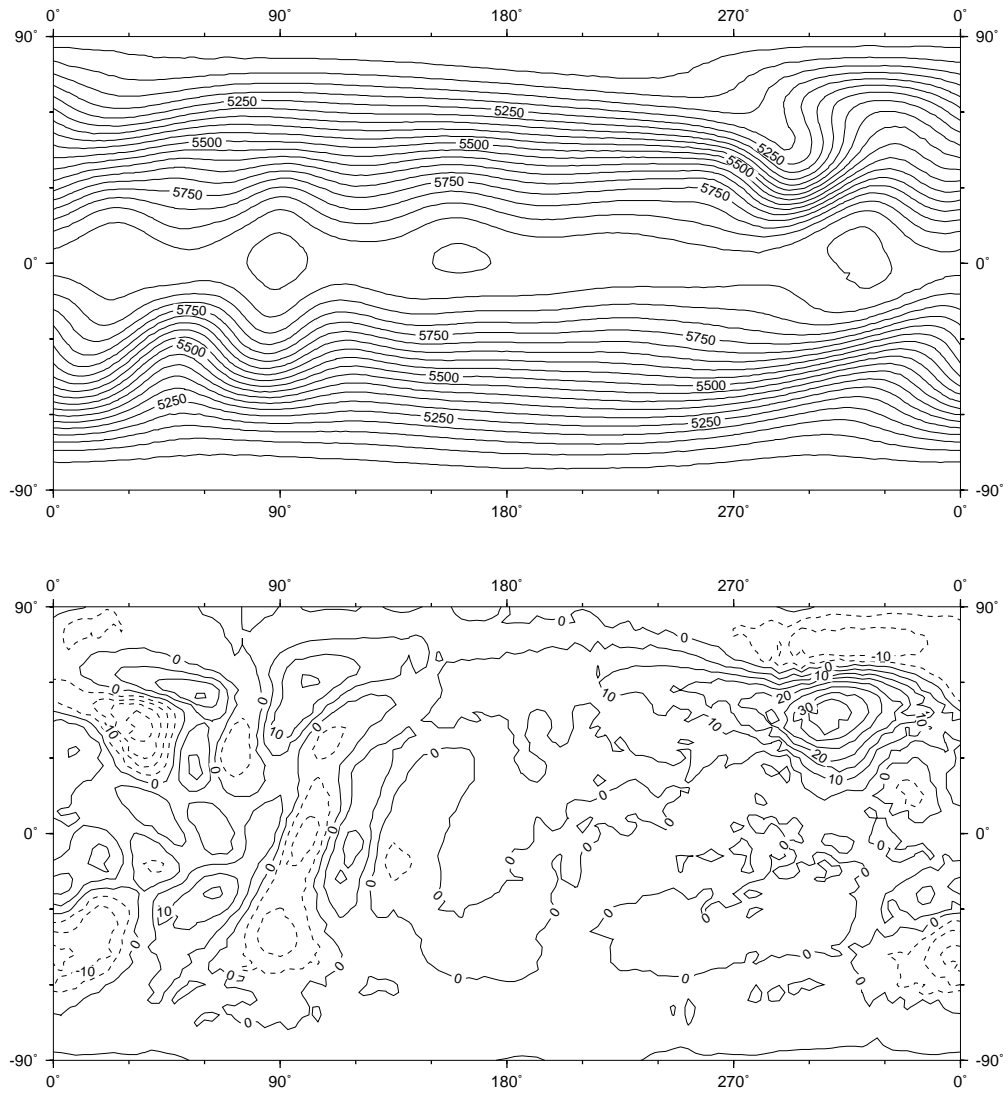
Figure 4.26: Zonal flow over an isolated mountain; height field $(h + h_s)$ after 120 hours (top, contour interval 50 m) and difference to reference solution (below, contour interval 2.5 m), $\Delta t = 225$ s
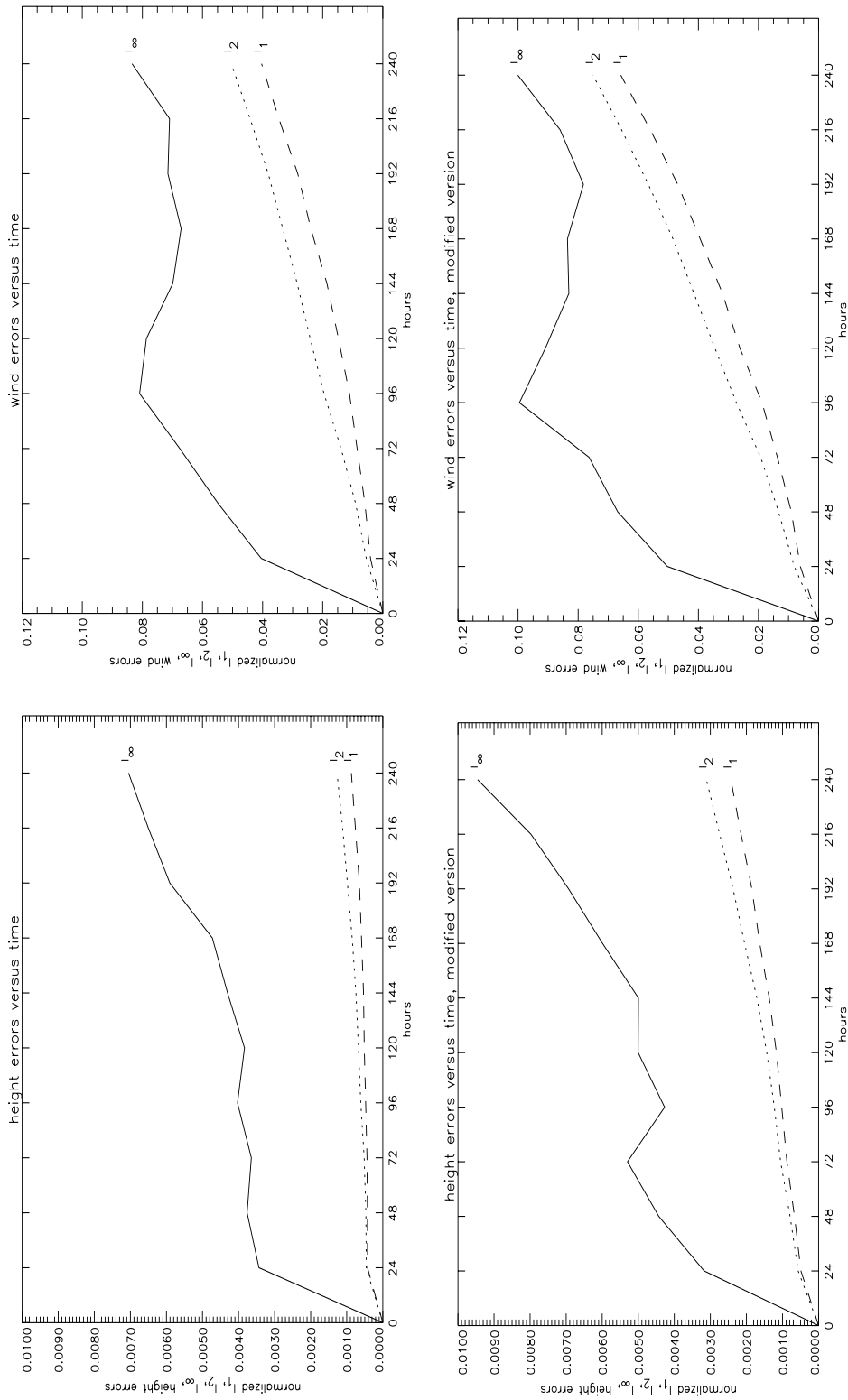
Figure 4.27: Zonal flow over an isolated mountain; height field $(h + h_s)$ after 240 hours (top, contour interval 50 m) and difference to reference solution (below, contour interval 5 m), $\Delta t = 225$ s

Figure 4.28: Zonal flow over an isolated mountain; height and wind error norms $\Delta t = 225$ s (original) and $\Delta t = 900$ s (modified)
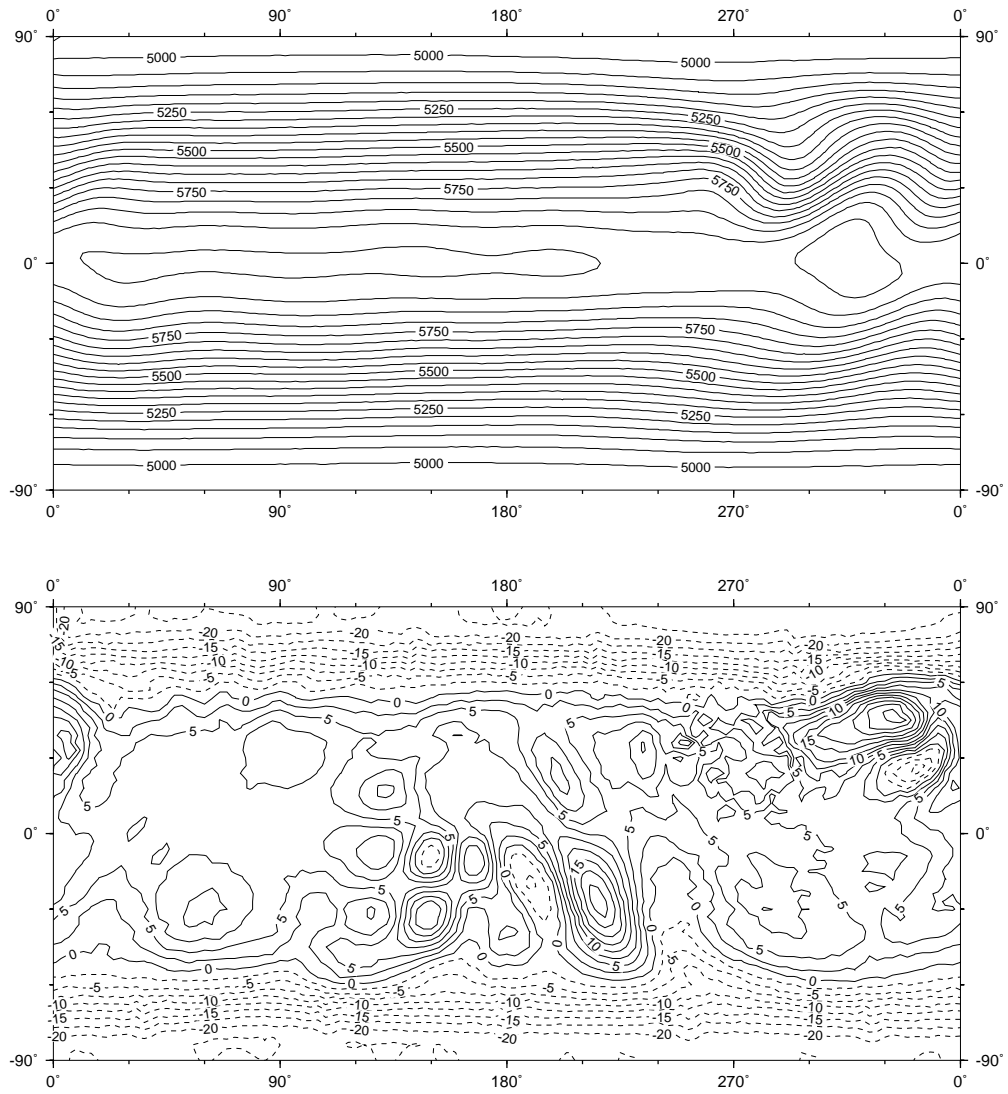
Figure 4.29: Zonal flow over an isolated mountain; height field $(h + h_s)$ after 120 hours (top, contour interval 50 m) and difference to reference solution (below, contour interval 2.5 m), $\Delta t = 900$ s, modified program
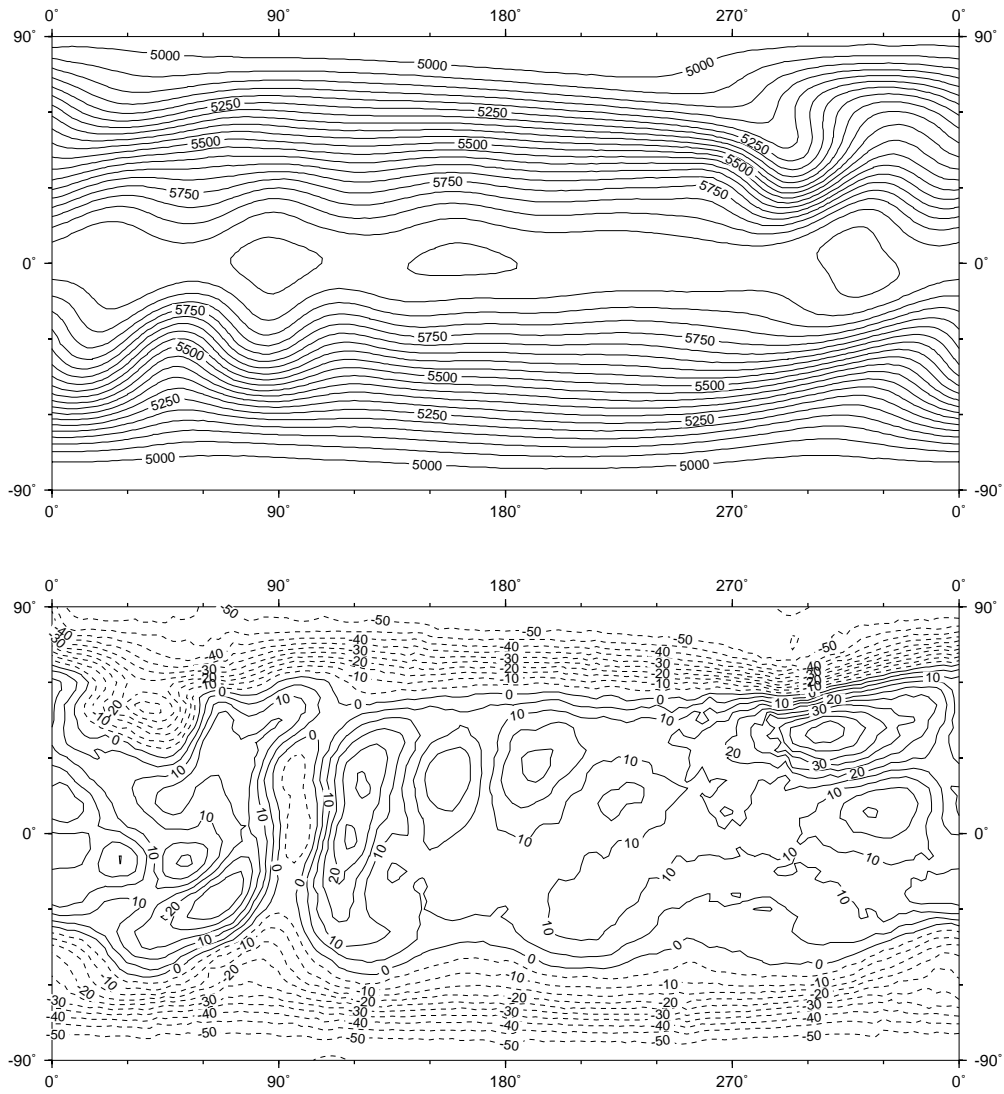
Figure 4.30: Zonal flow over an isolated mountain; height field $(h + h_s)$ after 240 hours (top, contour interval 50 m) and difference to reference solution (below, contour interval 5 m), $\Delta t = 900$ s, modified program

4.5 Rossby-Haurwitz Wave – Wavenumber 4

Rossby-Haurwitz waves can be considered as the de facto standard for meteorological tests. This test case consists of a regular pattern, which moves from west to east without change of shape by a given angular velocity. Only a wave number of $R = 4$ is included in the standard test set [6]. Unstable waves $R \geq 5$ are not considered.

For this test case, an analytical solution is not known. For evaluation we use the provided reference solution from a high resolution spectral transform model integration [2].

As reported in Table 4.8 the original version requires extremely small time steps to obtain stable results from the initial states (Figure 4.31). 60 s is the largest time step size for refinement step $m = 5$ using the original program. Also for spectral methods the time step size is smaller (600 s for T42 and 180 s for T106) than the default values (1200 s for T42 and 600 s for T106). The modified version of BARGLO allows $\Delta t = 225$ s. This time step size is larger than those reported for experiments with spectral methods.

The initializations of the height field and the wind field are shown in Figure 4.31. The reference solutions for day five and day ten are shown in Figure 4.32. The development of the height field as computed by the original program using $\Delta t = 60$ s and the deviations to the reference solutions at day five and ten are presented in Figures 4.33 and 4.34. The corresponding results for the modified program using $\Delta t = 225$ s are shown in Figures 4.35 and 4.36.

Figure 4.37 shows acceptable small height and wind errors, where again the modified program has slightly larger errors. Compared to similar resolutions with spectral models, the reference solutions are well approximated by both program versions of BARGLO.

m	Δt	after 2 days E	M	after 5 days E	M	after 10 days E	M
3	1800	0.796	0.999	0.737	0.997	divergent	
3	900	0.819	0.999	0.665	0.998	0.559	0.997
4	450	0.938	0.999	1.152	0.998	divergent	
4	225	0.951	1.000	0.885	0.999	0.796	0.998
5	60	0.989	1.000	0.971	1.000	0.943	0.999
modified program							
3	3600	0.786	0.999	0.675	0.998	0.665	0.997
4	1800	0.891	0.999	0.786	0.998	0.694	0.996
4	900	0.927	1.000	0.841	0.999	0.739	0.997
5	225	0.974	1.000	0.953	1.000	0.909	0.999

Table 4.8: Rossby-Haurwitz wave – wavenumber 4; relative conservation of energy and mass, original and modified program
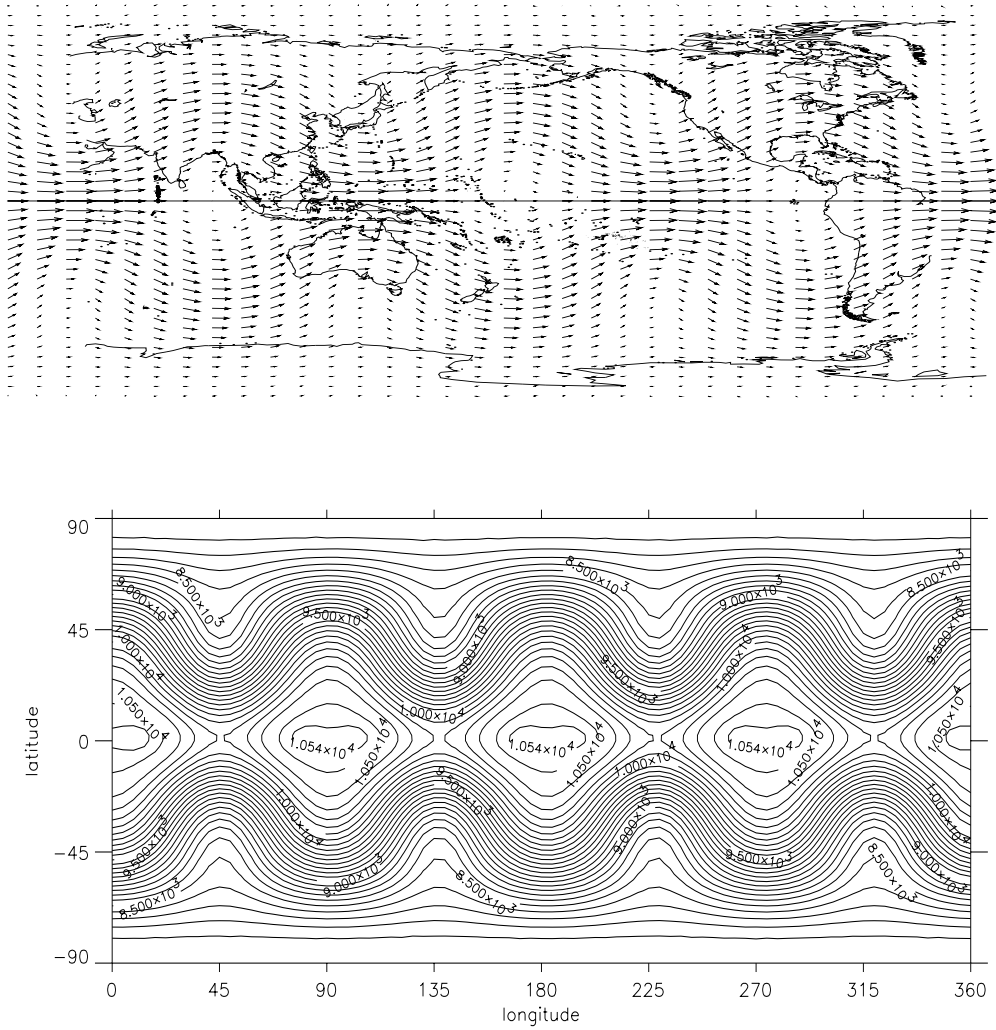
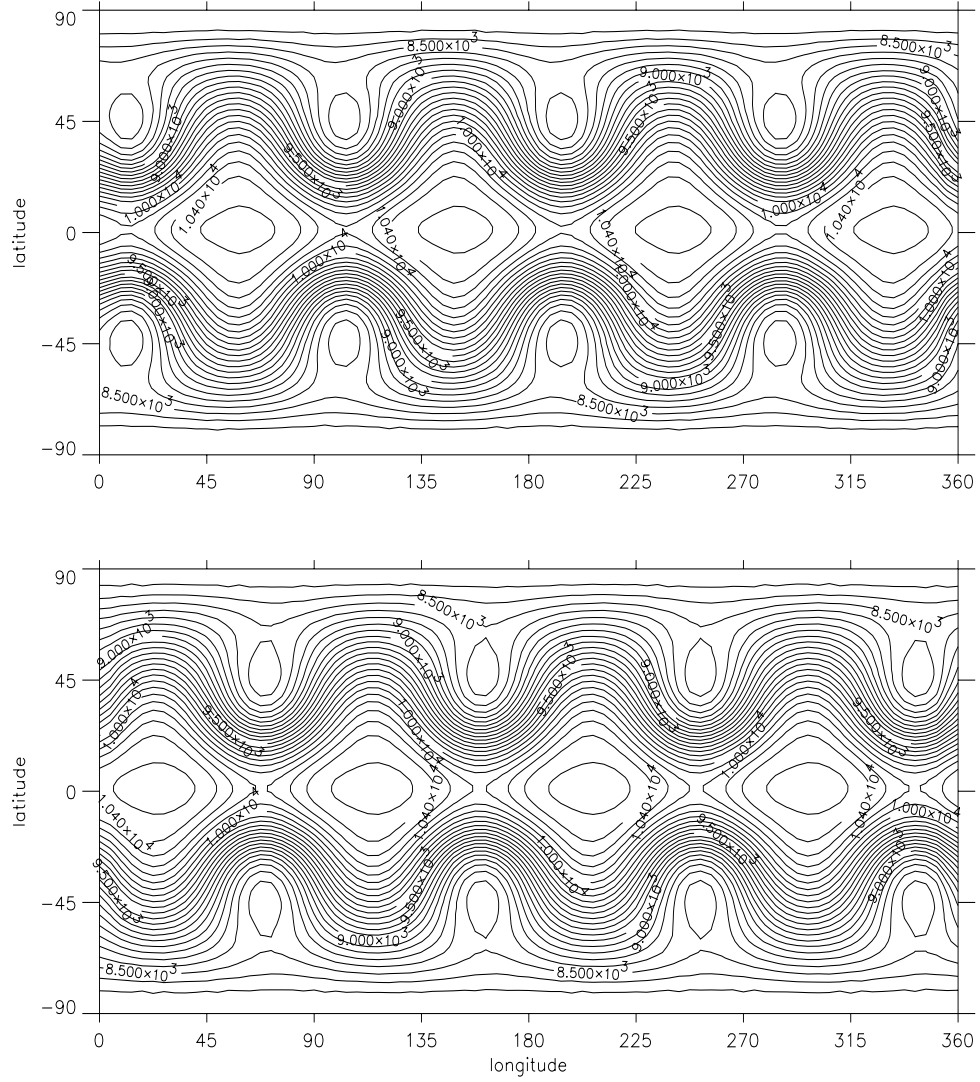Figure 4.31: Rossby-Haurwitz wave – wavenumber 4; initial wind and height field

Figure 4.32: Rossby-Haurwitz wave – wavenumber 4; reference height field for 120 (top) and 240 hours (below), (contour interval 100 m)
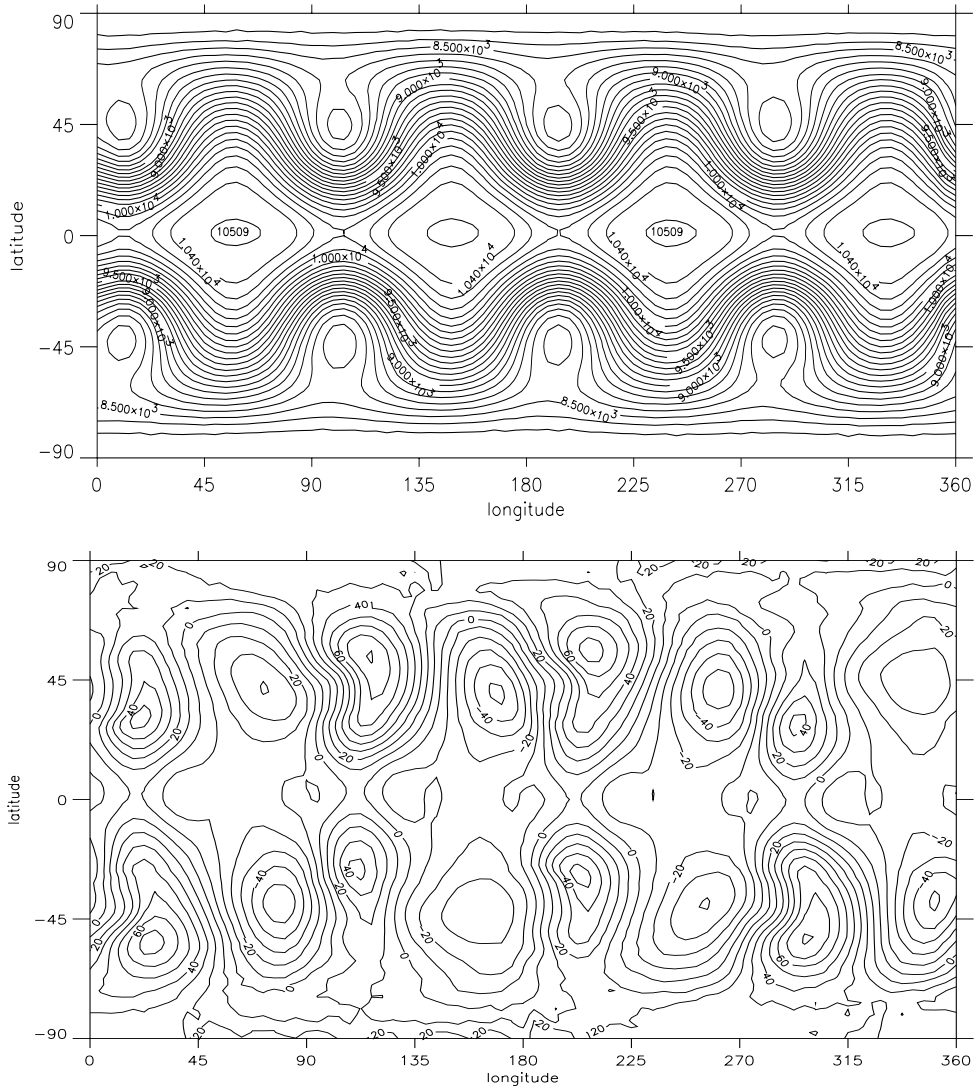
Figure 4.33: Rossby-Haurwitz wave – wavenumber 4; height field after 120 hours (top, contour interval 100 m) and difference to reference solution (below, contour interval 10 m), $\Delta t = 60$ s
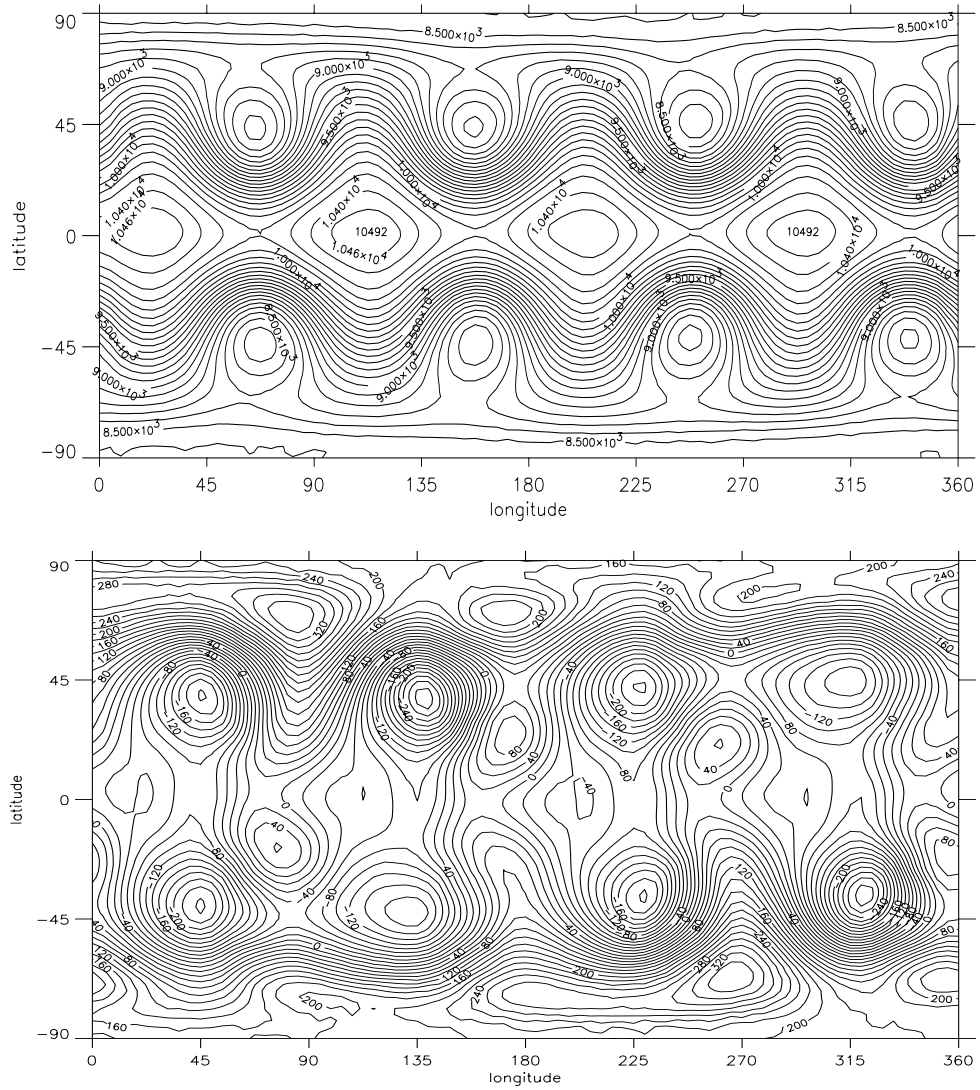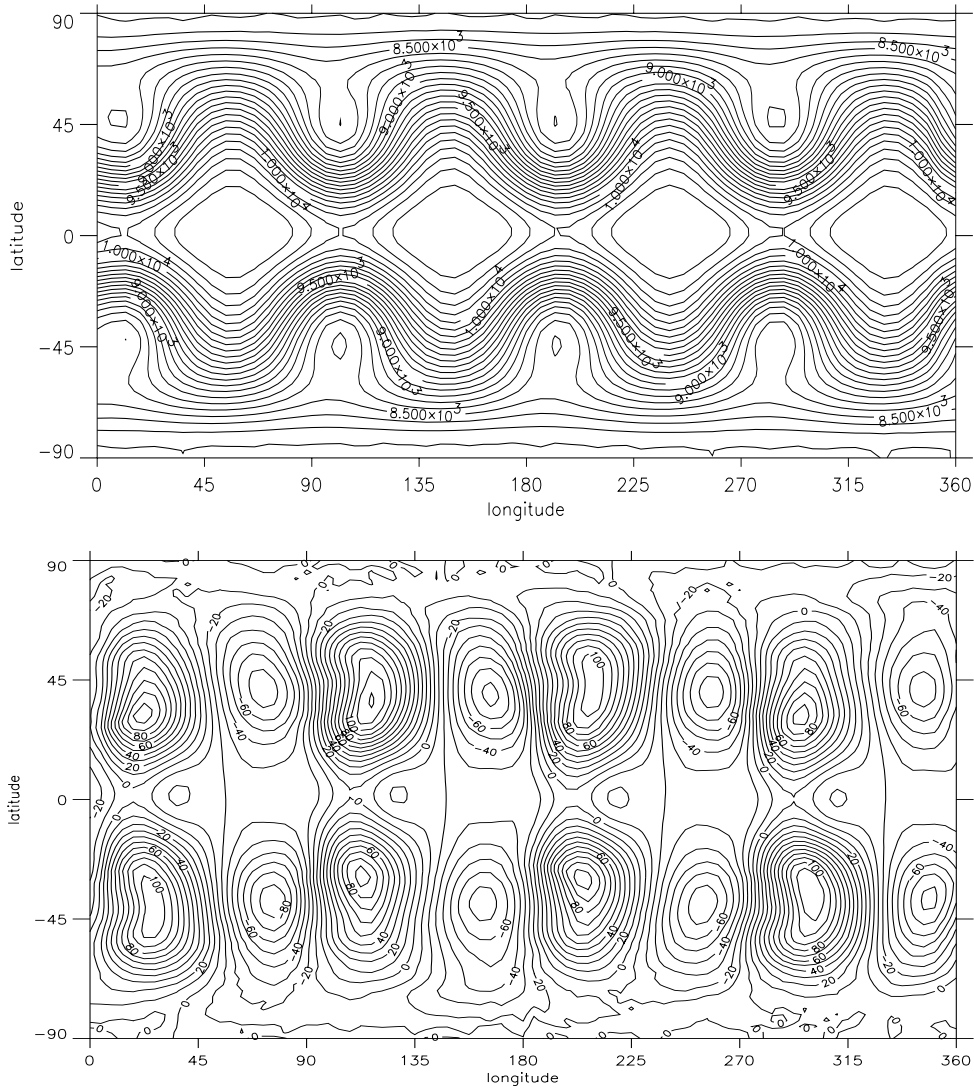
Figure 4.34: Rossby-Haurwitz wave – wavenumber 4; height field after 240 hours (top, contour interval 100 m) and difference to reference solution (below, contour interval 20 m), $\Delta t = 60$ s

Figure 4.35: Rossby-Haurwitz wave – wavenumber 4; height field after 120 hours (top, contour interval 100 m) and difference to reference solution (below, contour interval 10 m), $\Delta t = 225$ s, modified program
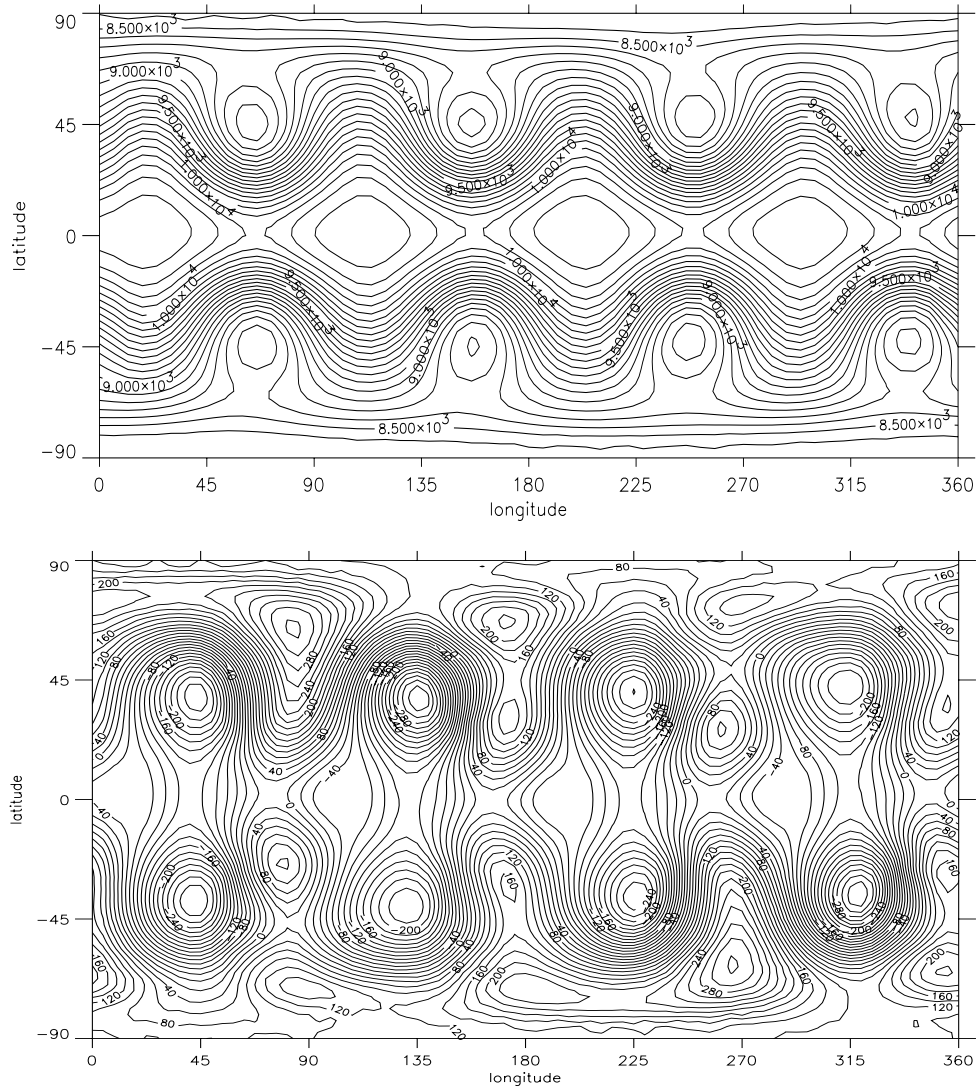
Figure 4.36: Rossby-Haurwitz wave – wavenumber 4; height field after 240 hours (top, contour interval 100 m) and difference to reference solution (below, contour interval 20 m), $\Delta t = 225$ s, modified program
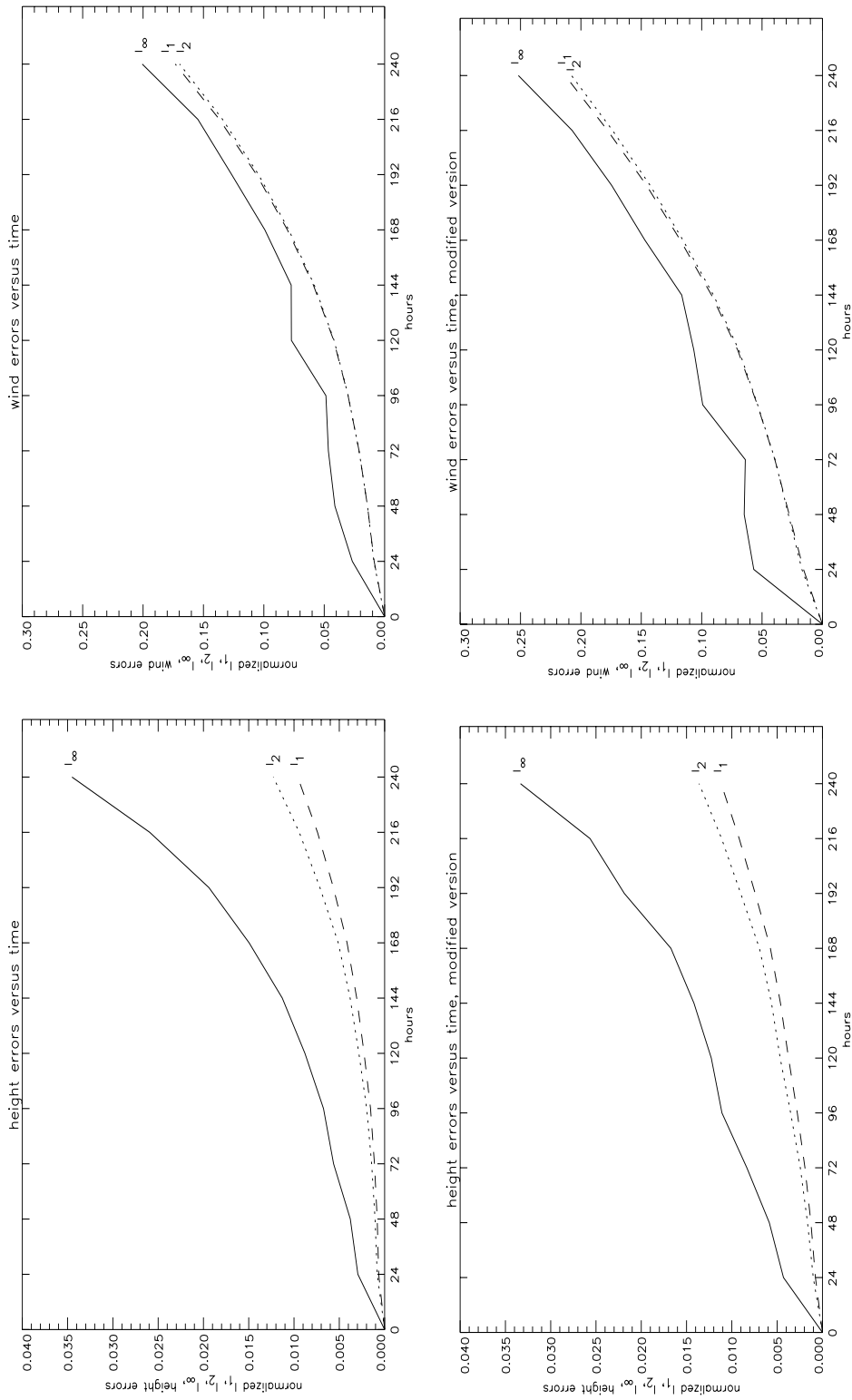
Figure 4.37: Rossby-Haurwitz wave – wavenumber 4; height and wind error norms $\Delta t = 60$ s (original) and $\Delta t = 225$ s (modified)

4.6 Analyzed 500 mb Height and Wind Field Initial Conditions

The following three test cases are based on observed data. They refer to initial conditions for 21 December, 1978, 9 January, 1979 and 16 January, 1979 (each 0000 GMT), respectively. The provided data sets are initialized via nonlinear normal mode initialization with a high resolution spectral transform model. Although this initialization scheme is not consistent with the scheme being tested, the initial data sets lead to reasonable results and it was not necessary to develop a special initialization program. Details about the initialization are provided in [2].

For all test cases the mean height is set to 10 km. The forecasts are calculated up to five days by the original and the modified model version. Table 4.9 shows the development of relative mass and energy for all three test cases. Also the error norms for the wind and height fields are graphed for the complete test set. Only the presentation of the resulting height patterns is limited to the case 21 December, 1978, which has a strong flow over the north pole and which is also discussed in [2].

Analyzing Table 4.9 we observe a significant loss of energy for all resolutions. We presume that this effect is due to a decrease of the wind velocities and the resulting loss of the kinetic energy. This requires further investigations.

In all test cases the time step sizes can be chosen larger in the modified version than in the original program. On refinement depth $m = 5$ the time step size is increased by a factor of 4 and we also recognize an improved conservation of the relative energy.

Figures 4.45, 4.46 and 4.47 show the height and wind error norms for the test cases. The error graphs of the original and modified versions look similar, but one should keep in mind, that the time step sizes in the modified version are larger than in the original program. Compared to the error norms in [2], which are calculated by a spectral model with $\Delta t = 600$ s, the error norms in Figures 4.45, 4.46 and 4.47 are about three times larger. [2].

North and south polar stereographic projections (figures 4.38 − 4.44 and 4.48 − 4.51) are presented for the 21 December 1978 case. The figures show the reference height fields computed by a spectral model, the height fields calculated by the two versions of BARGLO as well as the forecast errors compared to the reference solutions. They are provided for day 1 (24 hours) and day 5 (120 hours).

Additionally, figure 4.52 and 4.53 show graphs of the height field at every time step at the grid point closest to 40N and 105W, which is actually located at 40.65N and 104.89W for refinement depth $m = 5$. The graphs for the original version 4.52 obviously present , that the initial data set is not completely consistent with the scheme being used. Some gravity waves occur in the solutions, but they do not disturb the overall structure. In comparison to the modified version the contours shown in figure 4.53 are smoother and gravity wave effects only occur in the beginning of the forecast. Summing up the trace of the curves at 40N, 105W is similar in both figures. Additionally, the overall appearance

21 December 1978

m	Δt	after 2 days		after 5 days	
		E	M	E	M
3	1800	0.555	1.000	0.482	1.000
4	900	0.736	1.000	0.640	1.000
5	225	0.881	1.000	0.810	1.000
modified program					
3	1800	0.583	1.000	0.543	1.000
4	1800	0.778	1.000	0.740	1.000
5	900	0.901	1.000	0.867	1.000

9 January 1979

m	Δt	after 2 days		after 5 days	
		E	M	E	M
3	1800	0.583	1.000	0.494	1.000
4	900	0.761	1.000	0.676	1.000
5	225	0.890	1.000	0.832	1.000
modified program					
3	3600	0.671	1.000	0.667	1.000
4	1800	0.807	1.000	0.786	1.000
5	900	0.912	1.000	0.892	1.000

16 January 1979

m	Δt	after 2 days		after 5 days	
		E	M	E	M
3	1800	0.533	1.000	0.476	1.000
4	900	0.748	1.000	0.657	1.000
5	225	0.884	1.000	0.824	1.000
modified program					
3	1800	0.587	1.000	0.529	1.000
4	1800	0.785	1.000	0.744	1.000
5	900	0.900	1.000	0.873	1.000

Table 4.9: Analyzed 500 mb height and wind field; relative conservation of energy and mass, original and modified program
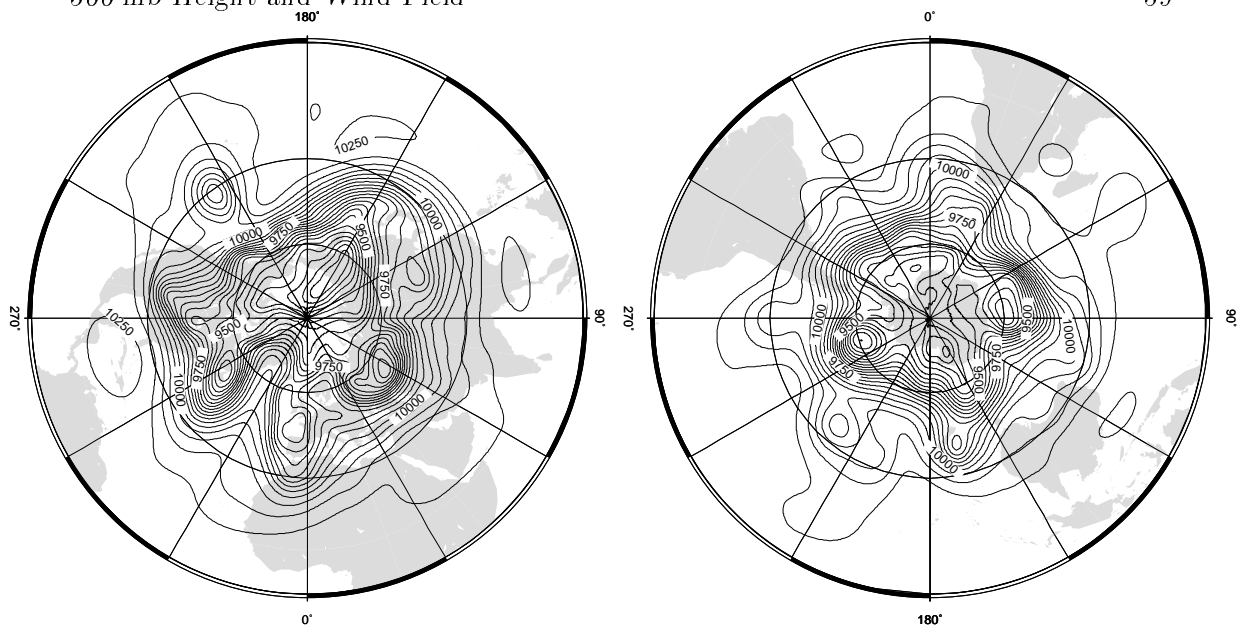
Figure 4.38: Initial height field for 21 December 1978 case, north (left) and south polar stereographic projection (right), contour interval 50 m

of the curves is well met in comparison to the corresponding graphs in [2], even though the grid point locations are naturally not identical. Only the courses of the curves are less clear-cut, especially concerning the extreme values.
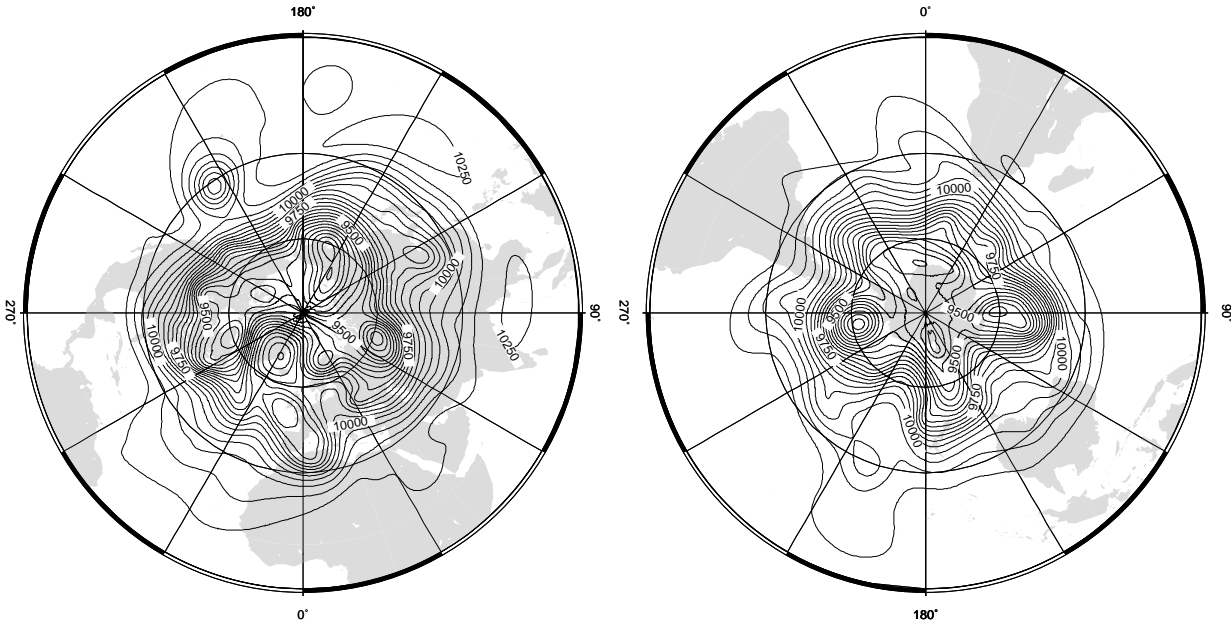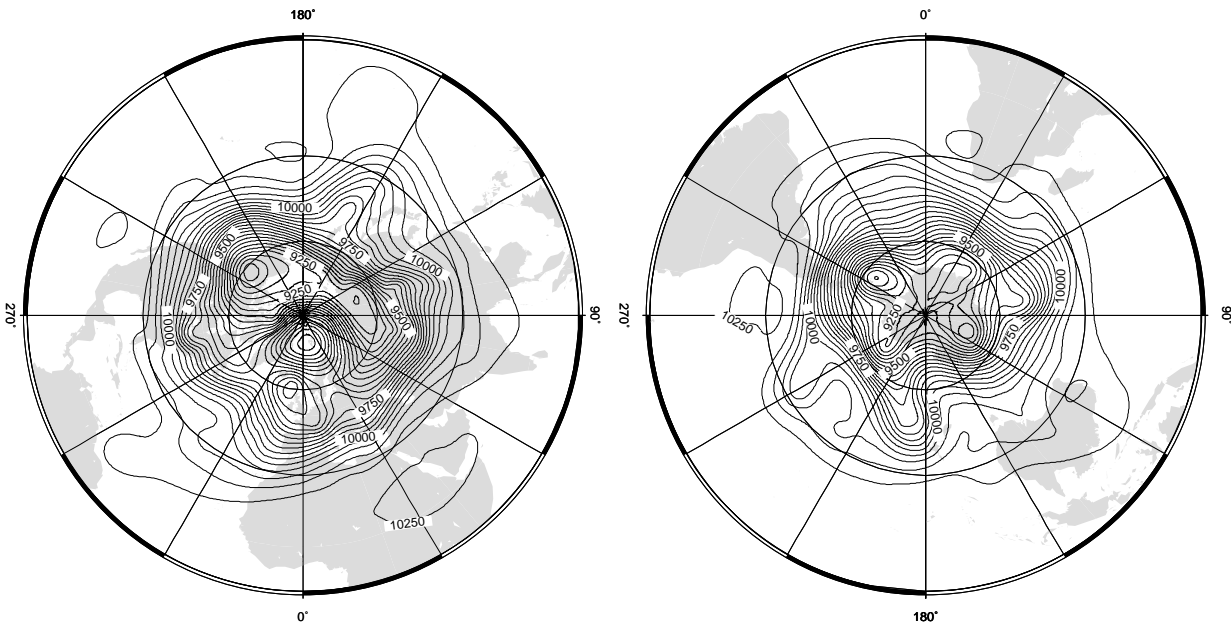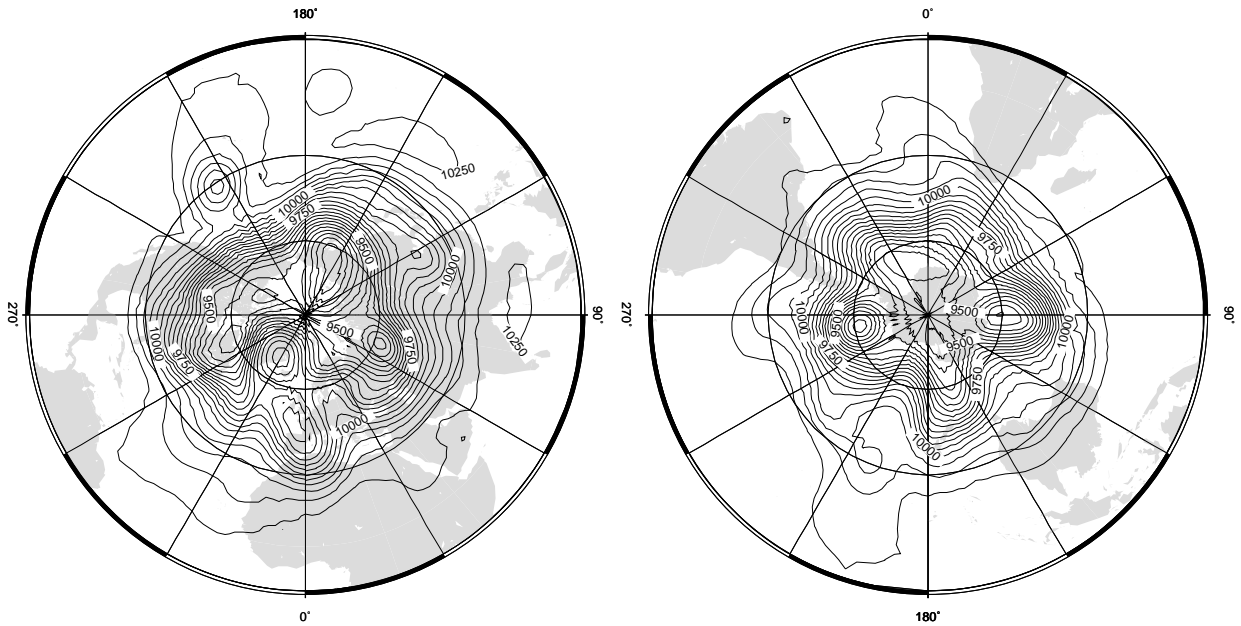
Figure 4.39: Reference solution for day 1 of 21 December 1978 case, north (left) and south polar stereographic projection (right), contour interval 50 m

Figure 4.40: Reference solution for day 5 of 21 December 1978 case, north (left) and south polar stereographic projection (right), contour interval 50 m

Figure 4.41: Height field for day 1 of 21 December 1978 case, north (left) and south polar stereographic projection (right), contour interval 50 m
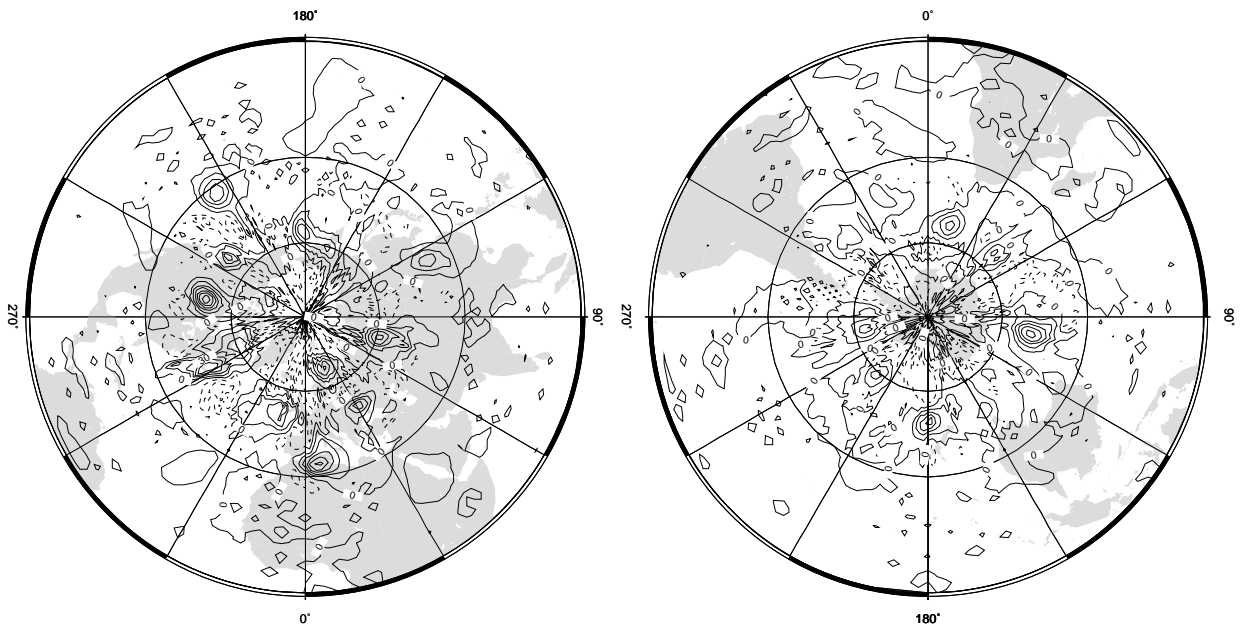

Figure 4.42: Difference with reference solution for height field for day 1 of 21 December 1978 case, north (left) and south polar stereographic projection (right), contour interval 15 m (dashed lines negative, solid lines positive)
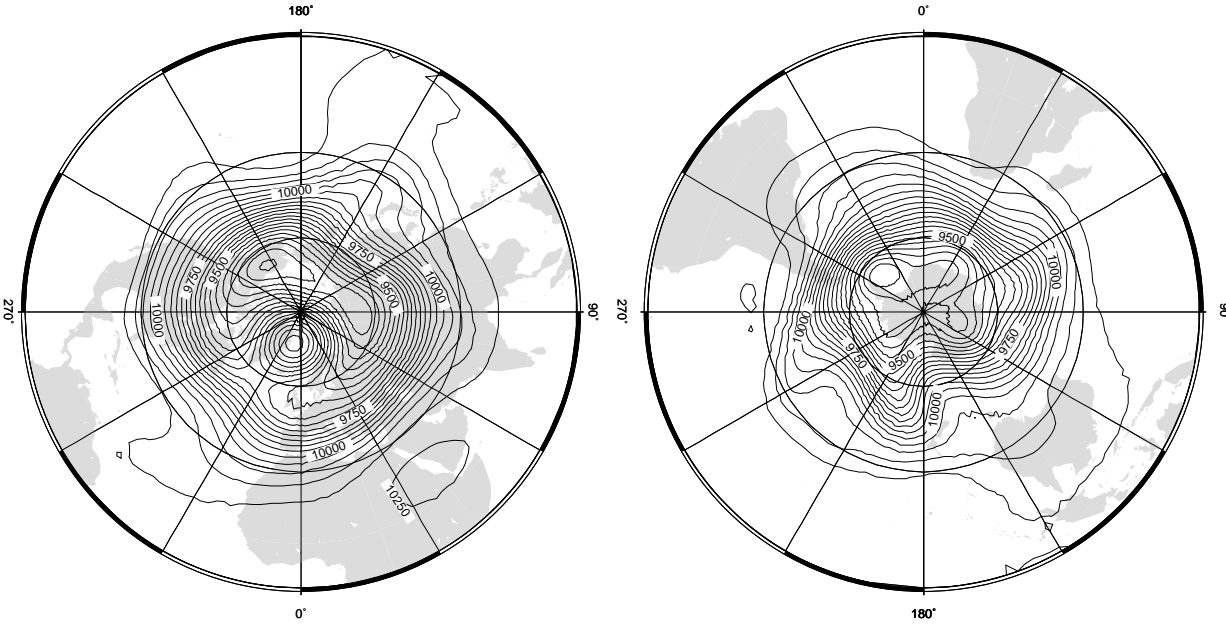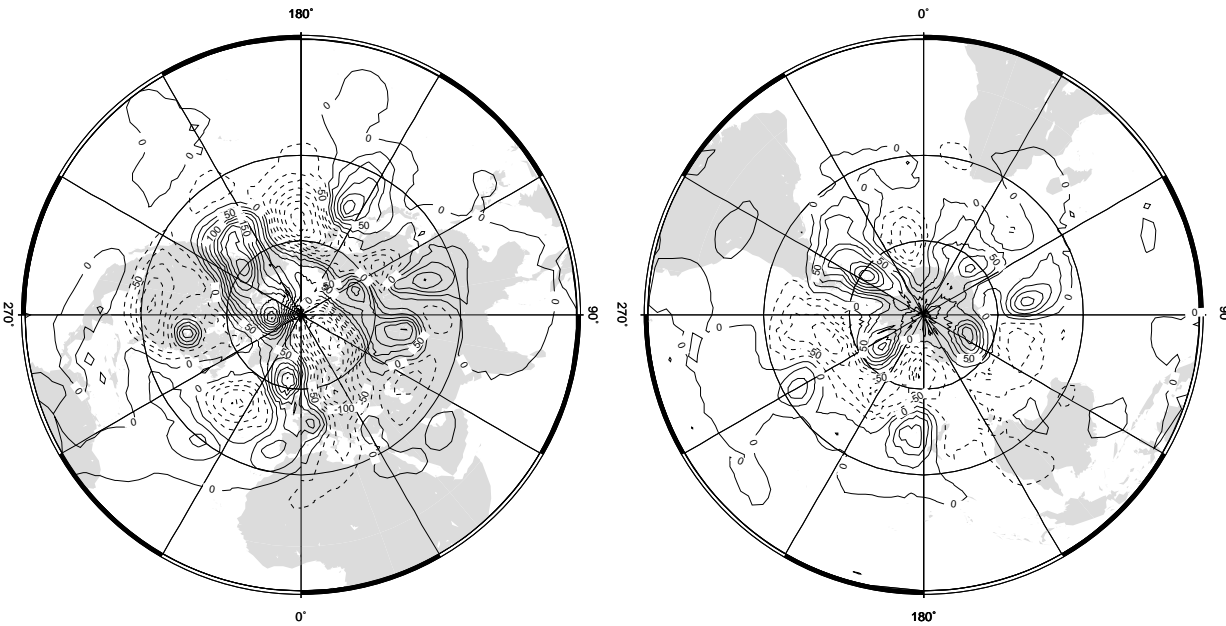
Figure 4.43: Height field for day 5 of 21 December 1978 case, north (left) and south polar stereographic projection (right), contour interval 50 m

Figure 4.44: Difference with reference solution for height field for day 5 of 21 December 1978 case, north (left) and south polar stereographic projection (right), contour interval 25 m (dashed lines negative, solid lines positive)
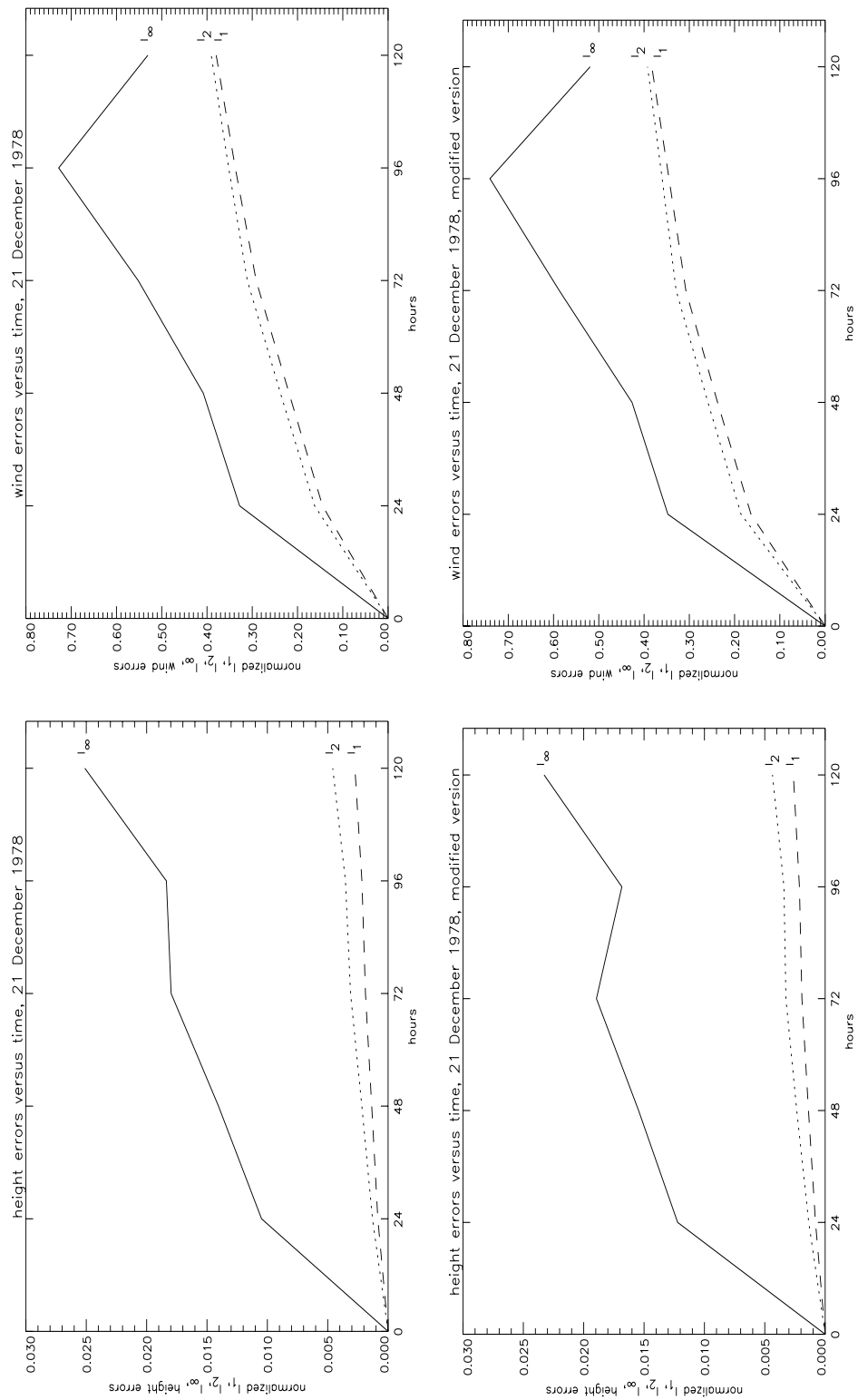
Figure 4.45: Height and wind error norms for case 21 December, 1978, $\Delta t = 225$ s (original) and $\Delta t = 900$ s (modified)
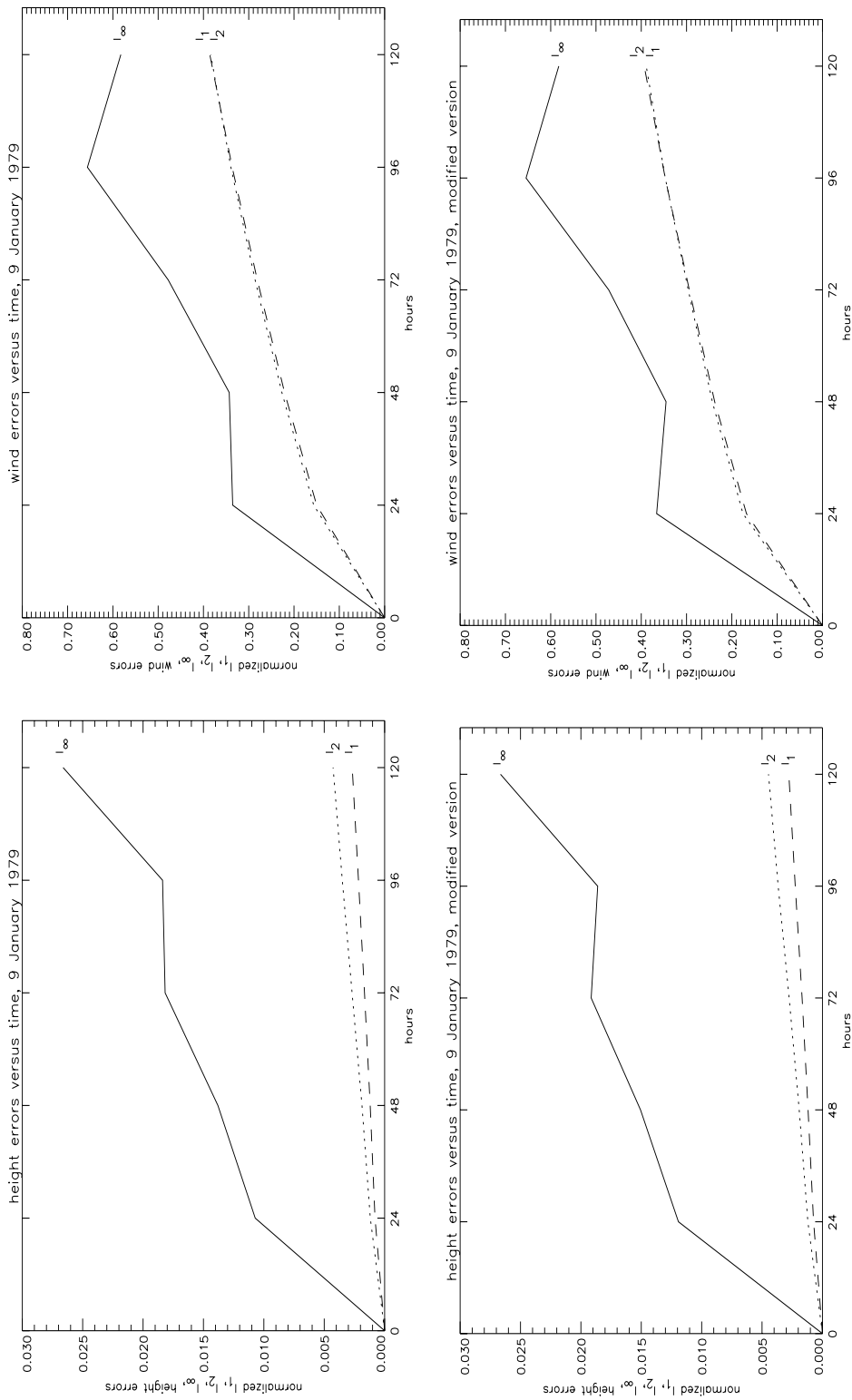
Figure 4.46: Height and wind error norms for case 9 January, 1979, $\Delta t = 225$ s (original) and $\Delta t = 900$ s (modified)
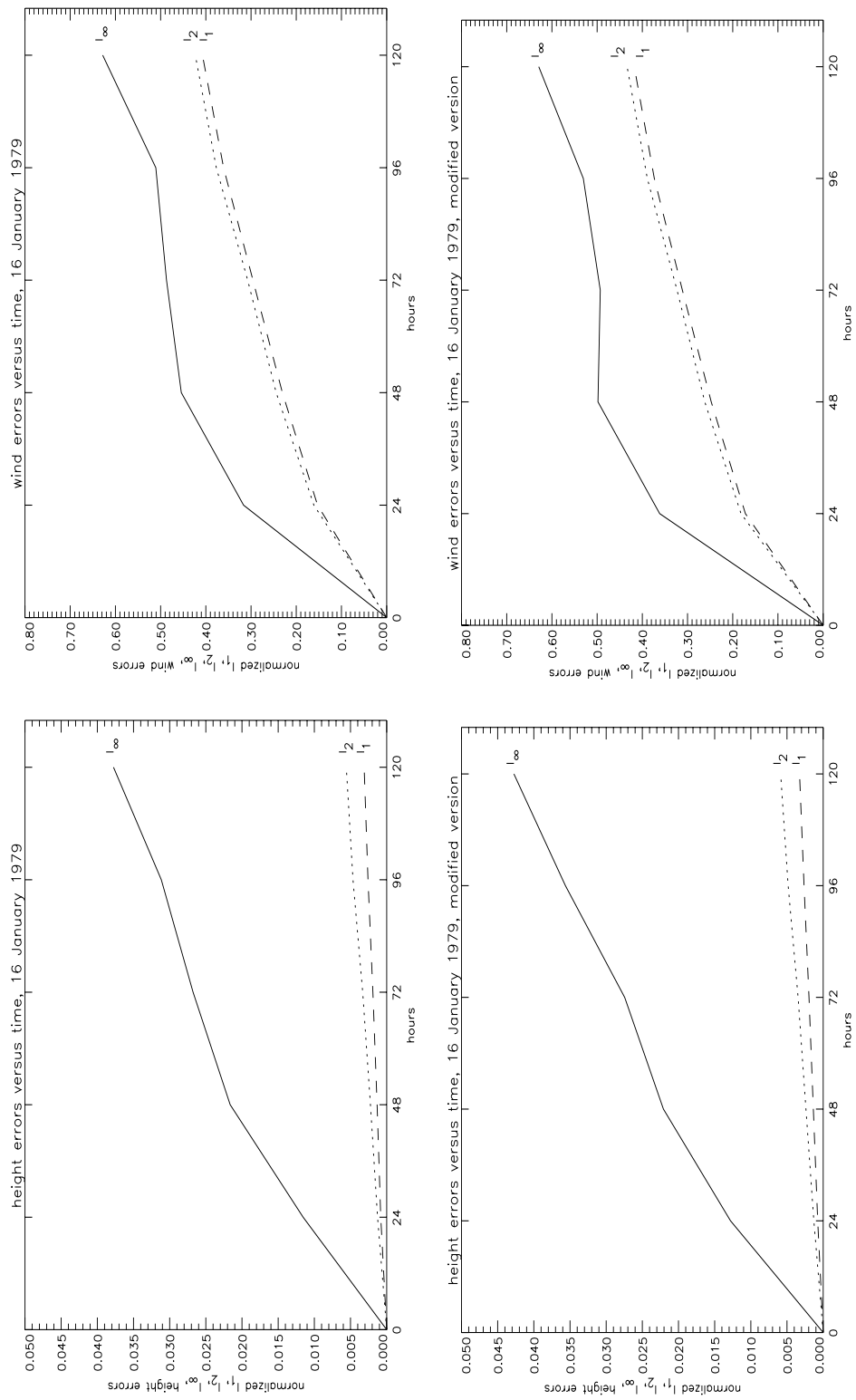
Figure 4.47: Height and wind error norms for case 16 January, 1979, $\Delta t = 225$ s (original) and $\Delta t = 900$ s (modified)
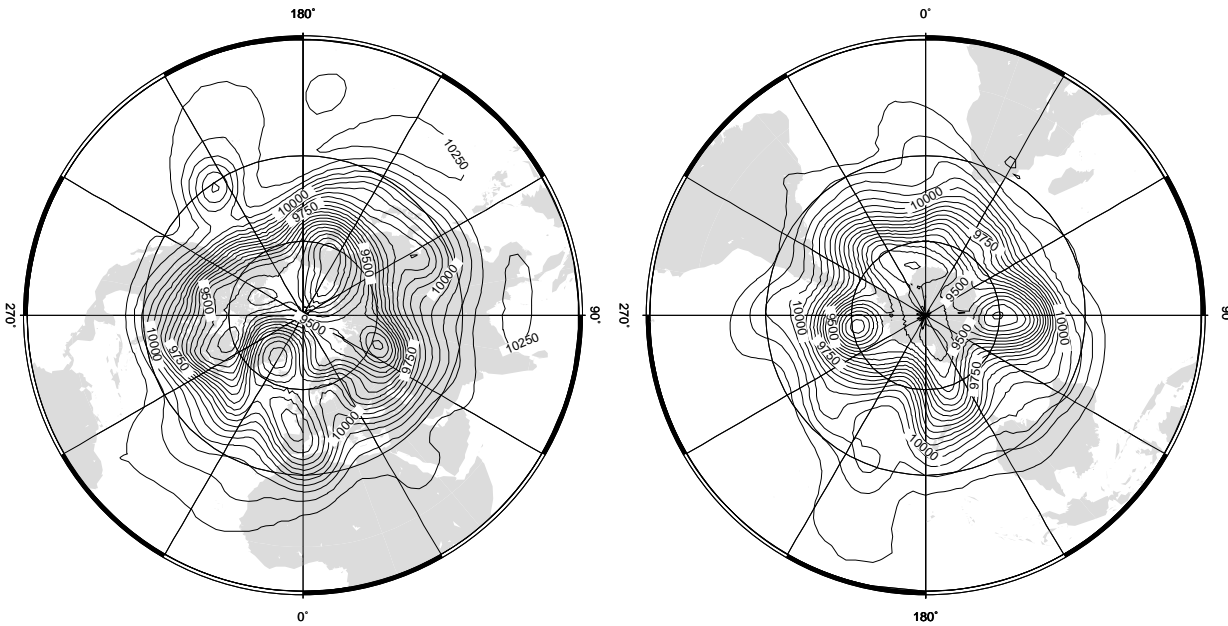
Figure 4.48: Height field for day 1 of 21 December 1978 case, modified program, north polar stereographic projection (left), south polar stereographic projection (right), contour interval 50 m
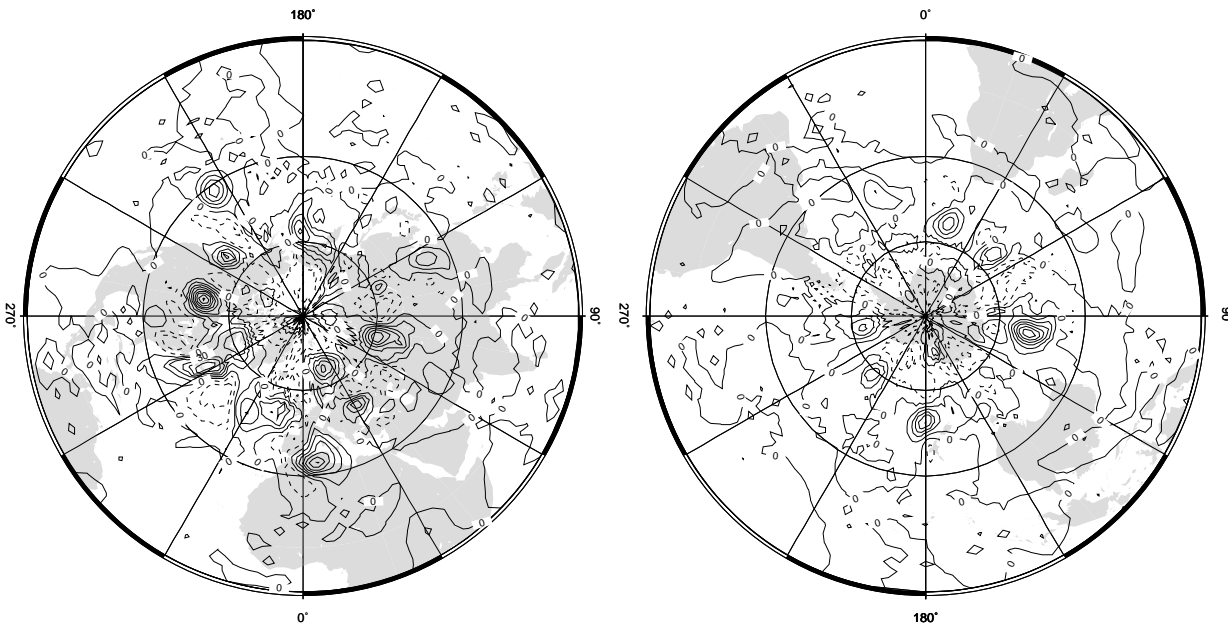
Figure 4.49: Difference with reference solution for height field for day 1 of 21 December 1978 case, modified program, north polar stereographic projection (left), south polar stereographic projection (right), contour interval 15 m (dashed lines negative, solid lines positive)
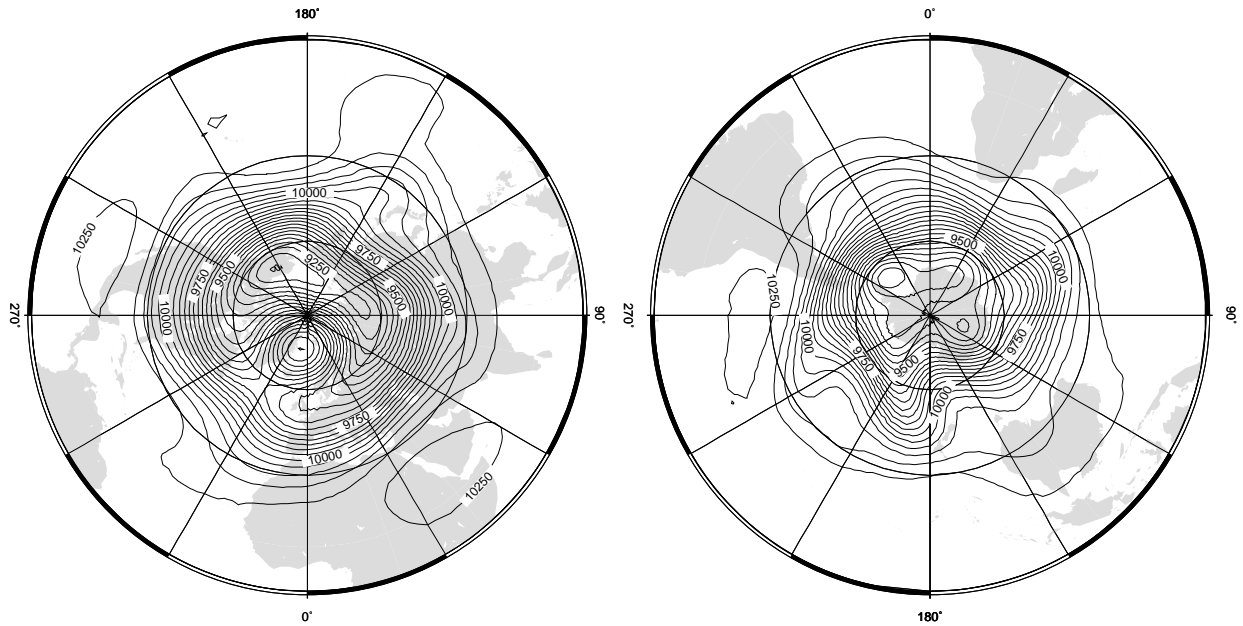
Figure 4.50: Height field for day 5 of 21 December 1978 case, modified program, north polar stereographic projection (left), south polar stereographic projection (right), contour interval 50 m
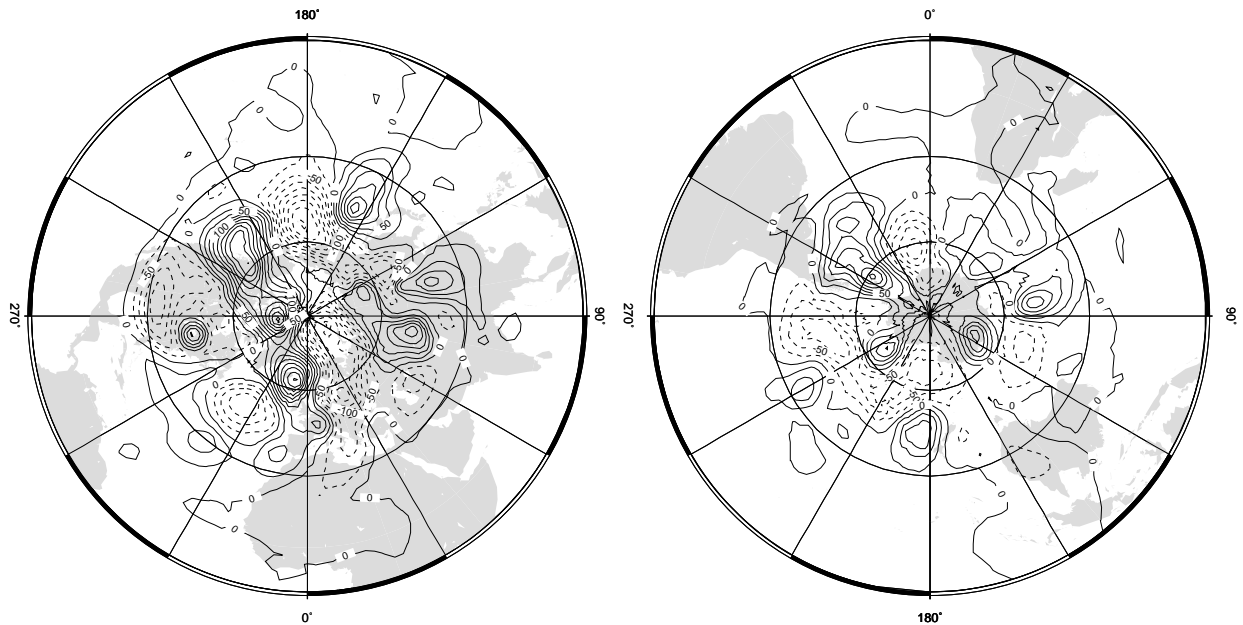

Figure 4.51: Difference with reference solution for height field for day 5 of 21 December 1978 case, modified program, north polar stereographic projection (left), south polar stereographic projection (right), contour interval 25 m (dashed lines negative, solid lines positive)
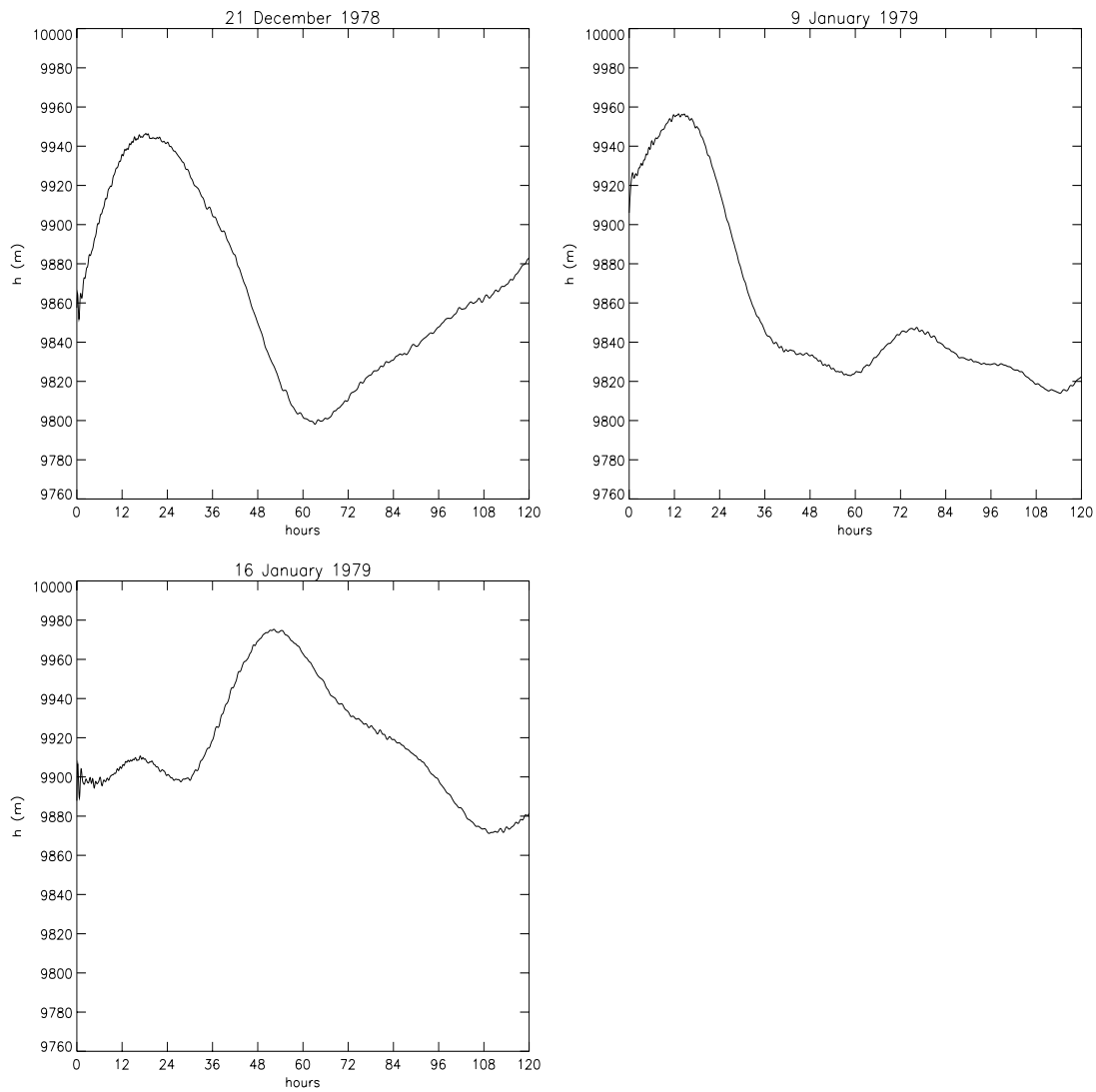
Figure 4.52: Height field at grid point closest to 40N, 105W for $m = 5$, original program
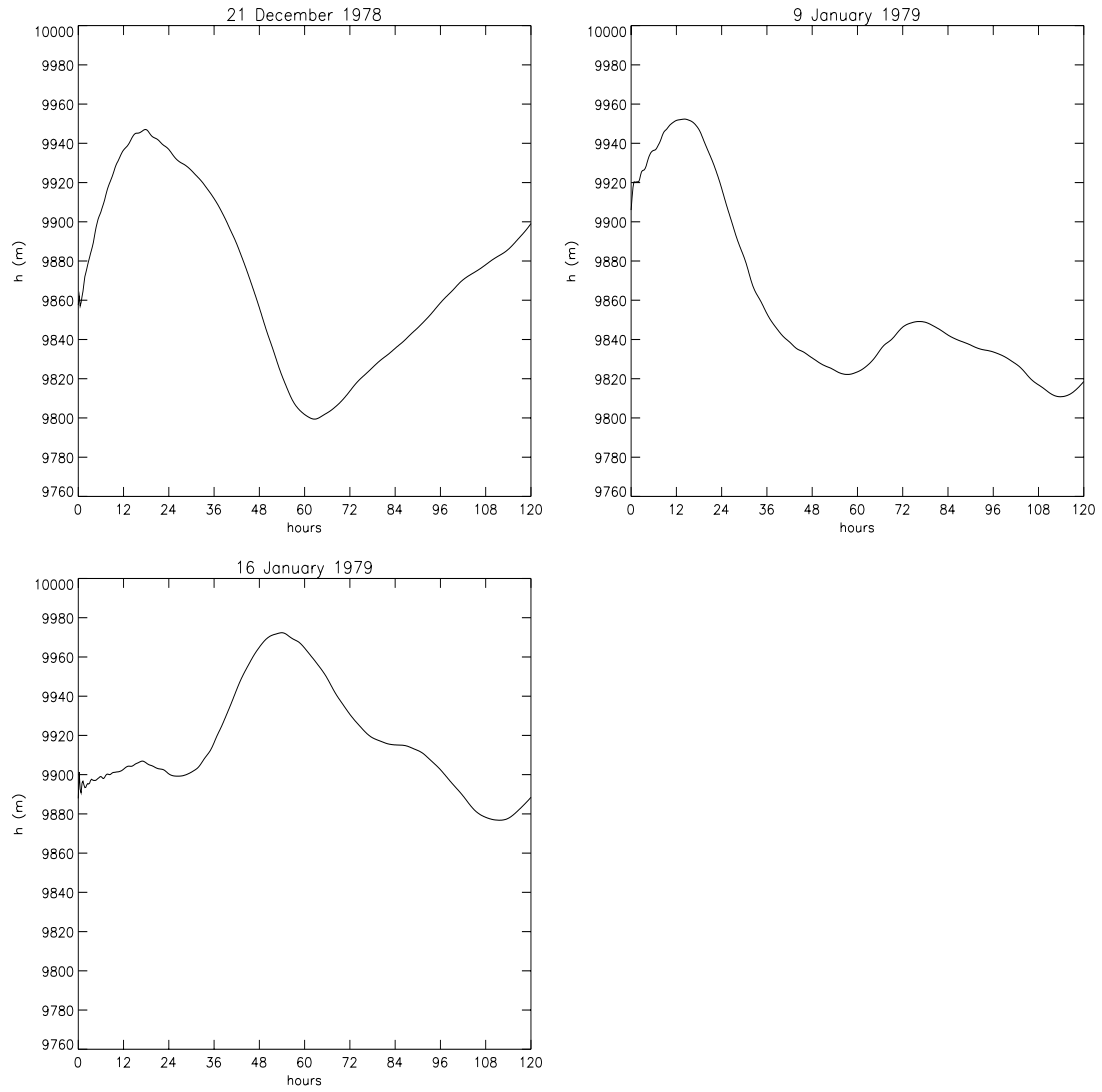
Figure 4.53: Height field at grid point closest to 40N, 105W for $m = 5$, modified program

4.7   Rossby-Haurwitz Wave – Wavenumber 1

This last reported test does not belong to the official test set. But it was used by the DWD as an initial test case. For this test, simulating an extremely smooth phenomenon the improvement of the program by the new time stepping is not severe.

m	Δt	after 2 days		after 5 days		after 10 days	
		E	M	E	M	E	M
3	3600	0.964	1.000	0.902	1.000	0.782	1.000
4	1800	0.990	1.000	0.975	1.000	0.943	1.000
5	900	0.997	1.000	0.993	1.000	0.986	1.000
modified program							
3	3600	1.058	1.000	1.125	1.001	1.165	1.002
4	3600	1.096	1.000	1.254	1.001	1.524	1.002
4	1800	1.038	1.000	1.092	1.001	1.154	1.001
5	1800	1.046	1.000	1.116	1.001	1.218	1.001
5	900	1.021	1.000	1.049	1.000	1.088	1.000

Table 4.10: Rossby-Haurwitz wave – wavenumber 1; relative conservation of energy and mass, original and modified program

5   A Concept for Parallelization

This concept aims towards the parallelization using a moderately parallel architecture not necessarily with distributed memory. Nevertheless, the concept is described on basis of a data partitioning and having message passing in mind. As the Figure 3.2 in Section 3.1 shows, the data structure is nicely regular. From the beginning there are at least five regular parts. Each of the parts itself consists of two large rhomboids, or four triangles, respectively. This structure origins from the initial mesh. Using more refinement steps does not disturb the regularity at all. Even the midpoints of the created triangles form nicely regular data fields. They are easily subdivided to supply each of the processor with the data for the calculations. All currently performed operations are local. Already in the sequential code at certain times in the algorithm some boundary update between adjacent parts of the initial structure is performed. This is at least the time when a parallel version should distribute new values. If the original subdomains are subdivided into even smaller ones, the communication should not only distribute values at the segment boundaries as it is done already now, but also communicate values at the newly created interior boundaries.

A recommended vehicle to do this, especially in three dimensions (where we assume a similar data structure) could be the GMD communications library [5] which can be
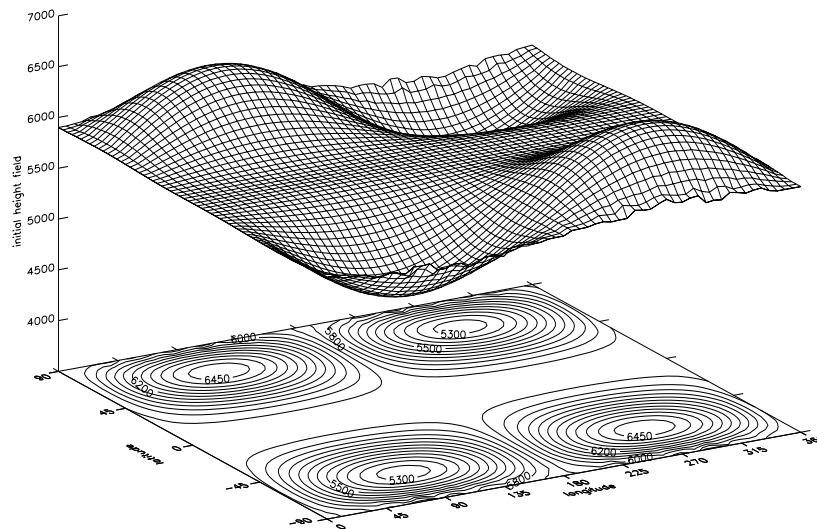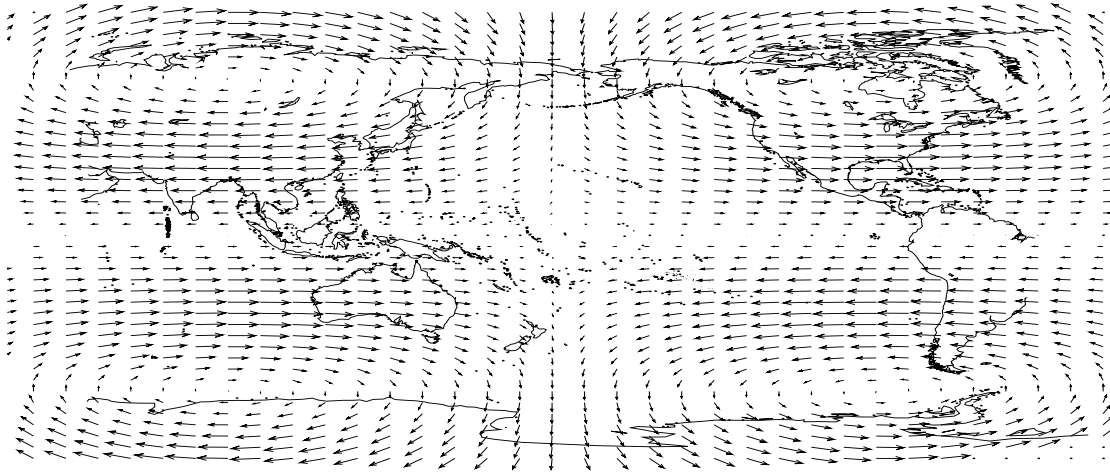
Figure 4.54: Rossby-Haurwitz wave – wavenumber 1, initial wind and height field
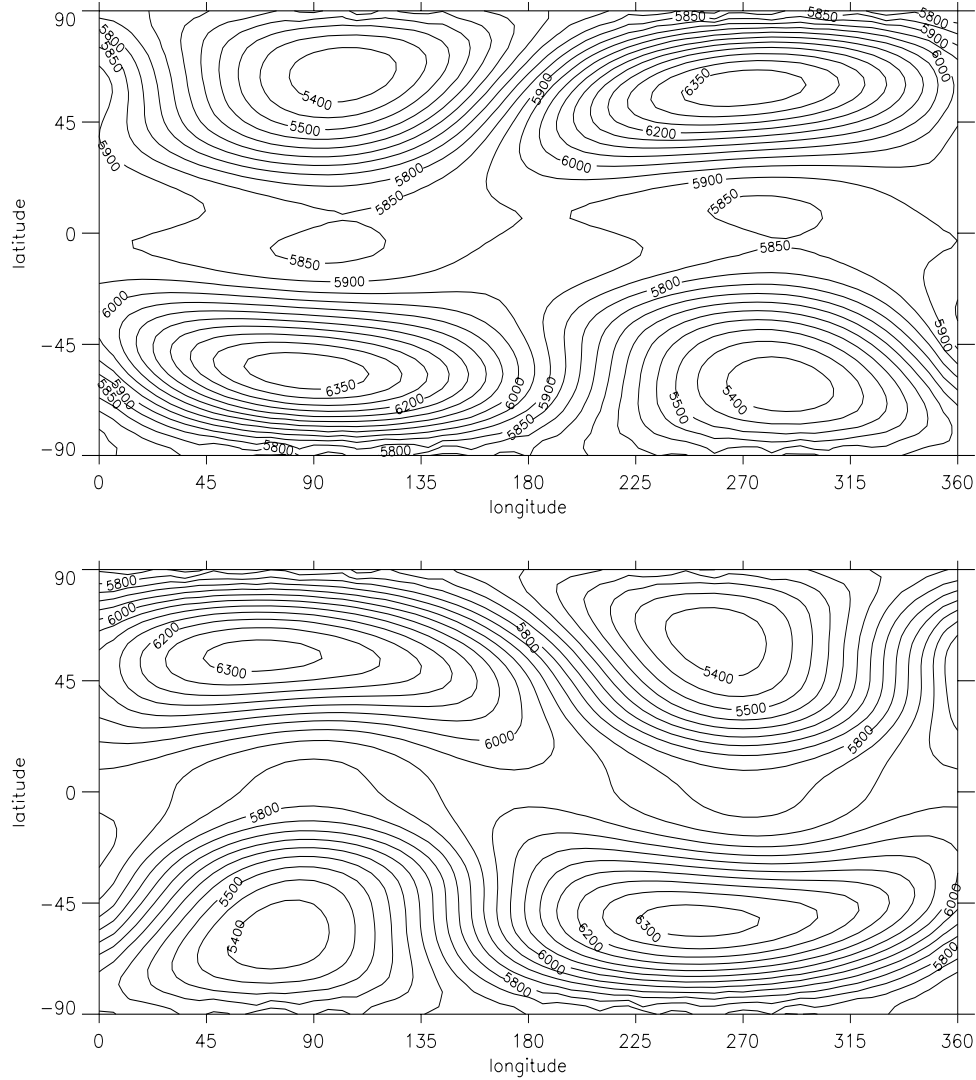
Figure 4.55: Rossby-Haurwitz wave – wavenumber 1, height field after 120 and 240 hours, $\Delta t = 900$ s, contours from 5.300 to 6.500 m
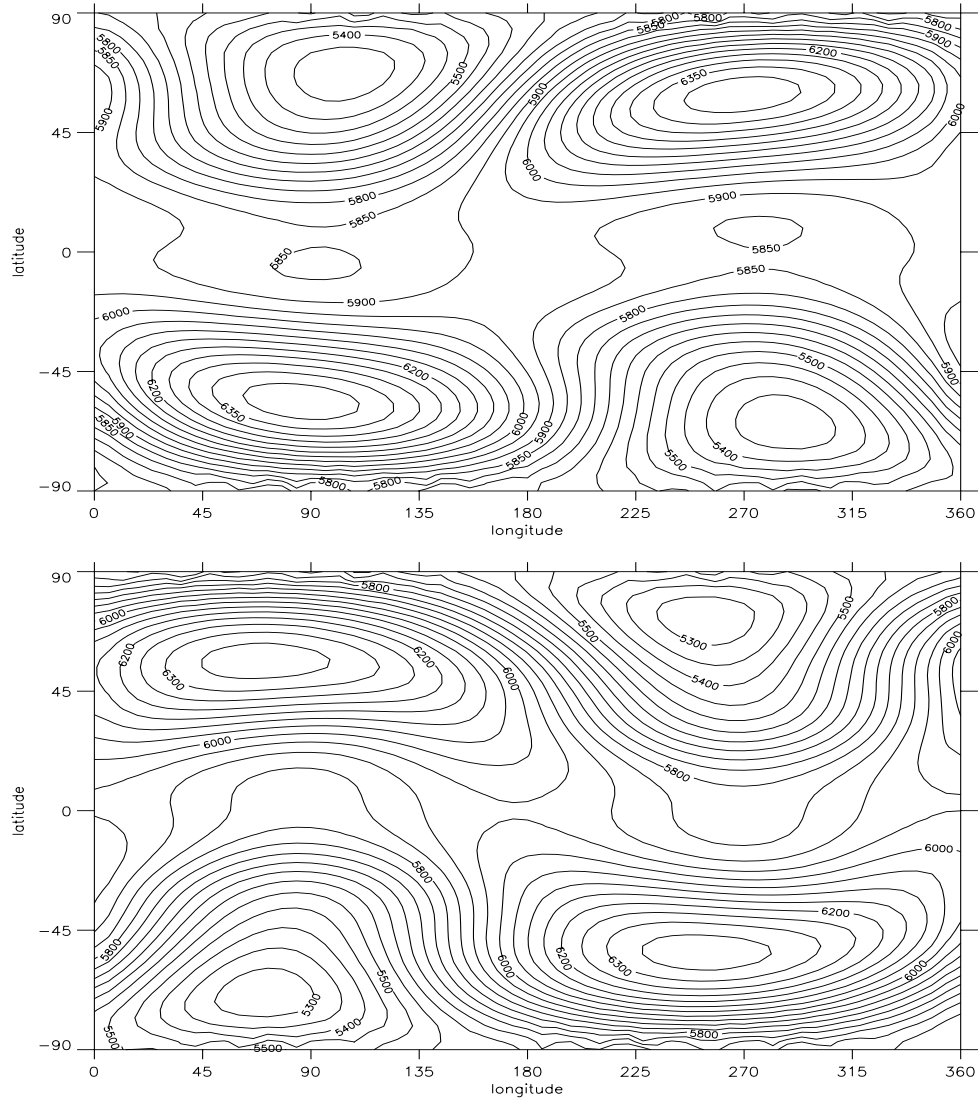
Figure 4.56: Rossby-Haurwitz wave – wavenumber 1, height field after 120 and 240 hours, $\Delta t = 1800$ s, contours from 5.300 to 6.500 m, modified program

placed on top of a message passing interface standard (MPI or PARMACS) and as a benefit the portability comes out in a natural way. This library assumes the concept of block-structured grids. The blocks can be created by subdividing the global data space only in x- and y-direction. This keeps the vertical data points together, as it is often desired due to the physical coupling in this direction. Nevertheless, the computation can be done on more or less rectangular data blocks.

6   Conclusion and Outlook

The grid point oriented approach based on an icosahedral grid is used to run the well-known shallow water benchmark suite. The approach offers some principle advantages

1. almost uniform triangular mesh

2. no special treatment at the poles

3. leading to a rectangular data structure

4. locality of the grid operators

In spite of these nice features, the original program showed a dramatic instability. By improving the time stepping algorithm a considerable improvement has been demonstrated.

test case	Δt original	Δt modified	Δt spectral
cosine bell	900 s	1800 s	600 s
geostrophic flow	120 s	675 s	600 s
flow with compact support	225 s	1800 s	600 s
isolated mountain	225 s	1800 s	600 s
Rossby–Haurwitz wave (4)	60 s	225 s	180 s
500 mb Height/wind field	225 s	900 s	600 s
Rossby–Haurwitz wave (1)	900 s	900 s	–

Table 6.1: Overview of time step sizes for the different test cases, refinement depth $m = 5$, T106

In all situations the time step size could be chosen larger than those reported for spectral methods. This indicates to possible advantages compared to spectral methods: The number of points in such grid point approaches may become similar or less to that of the reduced grids like in the IFS and the time step may become larger, optimal order methods are applicable and local refinements are more easily incorporated. Each of these features is important and justifies further work towards such a grid point oriented approach.

Further investigations should also compare the properties of approaches using either plane triangles or spherical triangles. Additionally, a systematic study of the influence of the diffusion constant K_4 should be performed. Another step to do is the parallelization of the program or of its next version. Depending on the data structure of the intended 3D-version, the parallelization can be started using the 2D program. Furthermore there is need to investigate the discretization more closely – both in time and in space. Sometimes the errors indicate to problems with the spatial discretization. Considerations of the order of discretization are important. What would higher order discretization techniques offer? Stability analysis has not yet been performed in a way to offer the best result. We only obtained a better result than the first approach.

References

[1] Baumgardner, J. R., and Frederickson, P. O., *Icosahedral Discretization of the Two-Sphere*, SIAM J. Numer. Anal., Vol. 22, No. 6, pp. 1107 – 11115, 1985

[2] Jakob, R., Hack, J. J., and Williamson, D. L., *Solutions to the Shallow Water Test Set Using the Spectral Transform Method*, NCAR Technical Note, NCAR/TN-388+STR, 1993

[3] Machenhauer, B.: *The spectral method.* Numerical Methods Used in Atmospheric Models, GARP publication series No. 17, pp. 121–275, 1979

[4] Prohl, P., *Barotropes Globalmodell in einem Dreiecksgitter – Programmdokumentation*, Deutscher Wetterdienst – Abteilung Forschung, Offenbach, 1995

[5] Ritzdorf, H., – *CLIC – The Communications Library for Industrial Codes*, Preliminary Version of the User's Reference Manual, Version 4.0

[6] Williamson, D. L., Drake, J. B., Hack, J. J., Jakob, R., and Swartztrauber, P. N., *A Standard Test Set for Numerical Approximations to the Shallow Water Equations in Spherical Geometry*, J. Comp. Phys., Vol. 102, pp. 211 – 224, 1992

[7] Hirsch C., *Numerical Computation of Internal and External Flows*, Vol. I, *Fundamentals of Numerical Discretization*, Wiley, 1988

[8] Wendt, J. F., *Computational Fluid Dynamics*, Springer, 1992